

ENERGY SCALE STUDY FOR PROSPECT'S MEASUREMENT OF THE  
ANTINEUTRINO SPECTRUM OF  $^{235}\text{U}$

BY  
XIANYI ZHANG

Submitted in partial fulfillment of the  
requirements for the degree of  
Doctor of Philosophy in Department of Physics  
in the Graduate College of the  
Illinois Institute of Technology

Approved  \_\_\_\_\_  
Advisor

Chicago, Illinois  
December 2019



## ACKNOWLEDGMENT

The accomplishment of this thesis research is with the help of many. Firstly, I give my special thanks to professor Bryce Littlejohn, my thesis advisor. Being both a mentor and a friend, he shared precious physics knowledge with me and set a great example for a young scientist. I am also grateful for professor Christ White, for accepting me to the IIT neutrino physics group and funding my thesis research. I would also like to thank Pranava Teja Surukuchi, who has been a great friend of mine. Pranava's enthusiasm has been a spur through my student life at IIT.

Other young scientists in PROSPECT collaboration, Karin Gilje, Tom Lanford, and Michael Mendenhall, have inspired me with their professionalism. They also offered great help in my research with their skill and knowledge. Danielle Berish, Ben Foust, Jeremy Gaison, Adam Hansell, Olga Kzylova, Jeremy Lu and Danielle Norcini are fantastic companions, who shared work of all aspects with me. I am thankful to Nathaniel Bowden, David Jaffe, Pieter Mumm, Minfang Yeh, and Chao Zhang for their valuable advice in my research.

I owe my great thanks to my parents, Huiqian Zhu and Caodaobaiyin, for selflessly supporting me. At last, I cannot thank Danyang Wang enough for her love and courage.

# TABLE OF CONTENTS

	Page
<b>ACKNOWLEDGEMENT</b> . . . . .	iii
<b>LIST OF TABLES</b> . . . . .	vii
<b>LIST OF FIGURES</b> . . . . .	xii
<b>LIST OF ABBREVIATIONS</b> . . . . .	xiii
<b>ABSTRACT</b> . . . . .	xv
<b>CHAPTER</b>	
<b>1. AN INTRODUCTION TO NEUTRINOS</b> . . . . .	1
<b>1.1. Beta-decay</b> . . . . .	1
<b>1.2. The Discovery of Neutrinos</b> . . . . .	3
<b>1.3. Observation of Neutrino Oscillations</b> . . . . .	4
<b>1.4. Massive Neutrinos</b> . . . . .	6
<b>1.5. Theory of Neutrino Oscillation</b> . . . . .	9
<b>1.6. Measurements of Neutrino Oscillation</b> . . . . .	12
<b>1.7. Future Tasks of Neutrino Experiments</b> . . . . .	12
<b>2. REACTOR ANTINEUTRINOS</b> . . . . .	14
<b>2.1. The Flux and Spectrum of Reactor Neutrinos</b> . . . . .	14
<b>2.2. Historical Context of Reactor Neutrino Experiments</b> . . . . .	18
<b>2.3. Reactor Antineutrino Anomaly</b> . . . . .	21
<b>2.4. Resolution of the RAA</b> . . . . .	24
<b>3. PROSPECT EXPERIMENT</b> . . . . .	26
<b>3.1. HFIR Reactor</b> . . . . .	26
<b>3.2. Detector Design</b> . . . . .	28
<b>3.3. Antineutrino Detection</b> . . . . .	32
<b>4. DETECTOR RESEARCH, DEVELOPMENT, CONSTRUCTION, AND COMMISSIONING</b> . . . . .	37
<b>4.1. Prototype Research</b> . . . . .	39
<b>4.2. <sup>6</sup>Li Loaded Liquid Scintillator</b> . . . . .	41
<b>4.3. Optical Grid</b> . . . . .	42
<b>4.4. PMT Modules</b> . . . . .	57
<b>4.5. Calibration System</b> . . . . .	59
<b>4.6. Detector Construction and Commissioning</b> . . . . .	61

4.7. Data Acquisition System . . . . .	66
5. PHYSICS OF LIQUID SCINTILLATOR DETECTORS . . . . .	69
5.1. Organic Scintillator Light Yield . . . . .	69
5.2. Birks' Quenching . . . . .	73
5.3. Cherenkov Radiation . . . . .	74
6. MONTE-CARLO SIMULATIONS FOR PROSPECT . . . . .	77
6.1. Geometrical Simulation . . . . .	77
6.2. Particle Generation and Interaction Simulations . . . . .	78
6.3. Truth-level Simulation . . . . .	80
6.4. DAQ Pulse Simulation . . . . .	82
7. DATA PROCESSING AND LOW-LEVEL CALIBRATION . . . . .	86
7.1. Data Processing . . . . .	86
7.2. Timing Calibration . . . . .	87
7.3. Position Calibration . . . . .	89
7.4. ADC to Energy conversion . . . . .	90
7.5. PSD Calibration . . . . .	94
8. ABSOLUTE ENERGY SCALE CALIBRATION . . . . .	96
8.1. Energy Scale Calibrations Activities . . . . .	97
8.2. Calibration Event Reconstruction . . . . .	101
8.3. Monte-Carlo Simulation of Calibrations . . . . .	105
8.4. Data vs. Monte-Carlo Comparison . . . . .	112
8.5. Position Dependence of Energy Response . . . . .	120
8.6. Energy Scale Stability . . . . .	122
8.7. Energy Resolution Stability . . . . .	126
8.8. Position Resolution Characterization . . . . .	126
8.9. Reconstruction Differences Among Segments . . . . .	128
8.10. Finalized Detector Response Model and Uncertainties for the IBD Spectrum Analysis . . . . .	129
9. IBD PROMPT ENERGY SPECTRUM OF ANTINEUTRINOS FROM <sup>235</sup> U . . . . .	137
9.1. IBD Event Selection . . . . .	137
9.2. Observation of Reactor Neutrinos on Earth's Surface . . . . .	141
9.3. Background Subtraction . . . . .	143
9.4. IBD Prompt Energy Spectrum . . . . .	145

9.5. Comparison with Spectrum Models . . . . .	146
10. CONCLUSION . . . . .	152
10.1. Personal Contribution . . . . .	153
10.2. Possible Improvement of This Work . . . . .	154
BIBLIOGRAPHY . . . . .	154

## LIST OF TABLES

Table	Page
1.1 Key parameters of neutrino oscillation . . . . .	13
2.1 An overview of historical reactor oscillation experiments . . . . .	19
2.2 $\theta_{13}$ reactor experiments . . . . .	21
3.1 The properties of HFIR . . . . .	27
3.2 Key parameters of the PROSPECT AD . . . . .	29
4.1 PROSPECT R&D and construction phases . . . . .	38
4.2 Designed and measured dimensional parameters of separators. . . . .	46
4.3 The count of fabricated separators passing each level of QC . . . . .	49
4.4 Mass of the optical grid components . . . . .	53
4.5 Detector assembly time line . . . . .	61
8.1 Calibration source utilized . . . . .	98
9.1 IBD event selection (page 1 of 2) . . . . .	138
9.2 IBD event selection (page 2 of 2) . . . . .	139
9.3 List of systematic uncertainties . . . . .	150

## LIST OF FIGURES

Figure	Page
1.1 The continuous $\beta$ spectrum of $^{210}\text{Bi}$ . . . . .	2
1.2 Atmospheric neutrino oscillation . . . . .	6
1.3 Solar neutrino oscillation . . . . .	7
2.1 Predicted reactor neutrino spectrum . . . . .	15
2.2 Expectation of detected reactor neutrino spectrum . . . . .	17
2.3 Confirmation of Reactor Neutrino Oscillation by KamLAND . . . . .	20
2.4 Historical Absolute Reactor Neutrino Flux . . . . .	22
2.5 The allowed region for the parameters of sterile oscillation . . . . .	23
2.6 Daya Bay IBD positron energy spectrum . . . . .	24
3.1 The dimensions and power distribution of HFIR . . . . .	27
3.2 Local background distribution at the HFIR facility . . . . .	28
3.3 The layout of the PROSPECT experiment . . . . .	30
3.4 The design of the PROSPECT AD . . . . .	30
3.5 The inner volume of the PROSPECT AD . . . . .	31
3.6 IBD detection schematic . . . . .	33
3.7 Pulse shape difference . . . . .	34
3.8 Event selection based on PSD . . . . .	35
3.9 An illustration of an event cluster . . . . .	36
3.10 An illustration of a single segment light collection . . . . .	36
4.1 A schematic of the 2-liter prototype with shielding . . . . .	39
4.2 The schematic of the 23-liter prototype . . . . .	40
4.3 A schematic of the 50-liter prototype . . . . .	41
4.4 The QA measurements of the $^6\text{LiLS}$ . . . . .	43
4.5 Detailed PROSPECT optical grid schematic . . . . .	44

4.6	Illustration of a separators sandwich structure	45
4.7	Reflectance measurement of DF2000MA	46
4.8	Separator lamination	48
4.9	Optical measurement on the PLA rods	50
4.10	Schematics of PLA rods	51
4.11	Assembled location of PLA rods	51
4.12	Stringing of the PLA rods	52
4.13	Thickness of separators	54
4.14	Separator reflectance measurement	55
4.15	Results of the goniometer measurements	55
4.16	Optical grid compatibility	56
4.17	A schematic of PLA rod lever test	57
4.18	Design of the PMT modules	58
4.19	The setup of the PROSPECT calibration system	60
4.20	Optical grid assembly illustration	63
4.21	The photograph of the PROSPECT AD assembly	64
4.22	The acrylic and aluminum tanks as containment vessel of the detector	64
4.23	The installed PROSPECT AD	66
4.24	DAQ system connection	67
4.25	DAQ triggering signal	68
5.1	Electron energy loss in ${}^6\text{LiLS}$	71
5.2	Quenched scintillator light response	75
5.3	Cherenkov radiation thresholds	76
6.1	The simulated IBD products angular distribution	79
6.2	Illustration of PG4 event tracking	81
6.3	The data structure of MC simulation and PROSPECT data	83
6.4	Schematic of PG4 output conversion	85

7.1	Data process procedures	86
7.2	Pulse timing reconstruction	88
7.3	Time offset in all detector segments	89
7.4	The “Hobbes effect” corner clipping muons	90
7.5	The fitted $z(dt)$ function	91
7.6	The light transport efficiency curve of all segments	92
7.7	$\ln(S_1/S_0)$ vs $dt$ of a segment	93
7.8	The geometric mean of $n$ -Li events	94
7.9	The single PE calibration for photostatistics	94
8.1	Positions of the PLA rods used for energy scale calibration runs	99
8.2	The PE per MeV evolution over time	100
8.3	Calibration gamma spectra reconstructed with the full PROSPECT AD	102
8.4	The segment hit multiplicity of calibration gamma clusters	103
8.5	The observed of $^{12}\text{B}$ spectrum in PROSPECT	104
8.6	AmBe gamma reconstruction	106
8.7	Quenched energy affected by different $k_{B1}$ values	107
8.8	Quenched energy affected by different $k_{B2}$ values	108
8.9	The effect of Cherenkov radiation in PG4	109
8.10	The affect of different detector parameters	110
8.11	The affect of separator thickness to energy scale	111
8.12	The affect of PLA rod dimensions to energy scale	111
8.13	Full detector data to MC gamma energy comparisons	115
8.14	Full detector data vs MC gamma multiplicity comparisons	116
8.15	$\chi^2$ distributions with respect to the values of nonlinearity parameters.	117
8.16	Single segment data to MC gamma energy comparisons	118
8.17	Indication of accidentally left calibration sources	119

8.18 AmBe data to MC comparison . . . . .	120
8.19 Discrepancies among calibration campaigns . . . . .	121
8.20 $E_{rec}/E_{mc}$ ratio vs. particle multiplicities . . . . .	122
8.21 Example of different volume sizes within three layers of segments. . . . .	123
8.22 Reconstructed gamma energy of $^{22}\text{Na}$ at different positions . . . . .	124
8.23 The decay chain involving the decays from $^{227}\text{Ac}$ to the RnPo events . . . . .	125
8.24 Detector stability characterization . . . . .	127
8.25 Distributions of $z$ and $dz$ of Po decayed $\alpha$ . . . . .	128
8.26 RnPo rate per segment . . . . .	129
8.27 Energy scale variation among segments . . . . .	129
8.28 Best fit MC compared to data of the $^{12}\text{B}$ spectrum . . . . .	130
8.29 The data to best fit MC comparison of the $^{22}\text{Na}$ gamma events . . . . .	131
8.30 Energy resolution function fitting to the standard deviations of gamma calibration spectra . . . . .	132
8.31 Reduced covariance matrices . . . . .	133
8.32 Calibration data to best fit MC comparison with energy scale un- certainties. . . . .	134
8.33 Detector response matrix . . . . .	136
9.1 Illustration of IBD PSD selection . . . . .	140
9.2 Illustration of the detector fiducial volume . . . . .	141
9.3 Different levels of IBD selection . . . . .	142
9.4 Reactor neutrino from HFIR . . . . .	142
9.5 Correlations between atmospheric pressure and neutron/IBD event rate. . . . .	144
9.6 IBD event rate stability . . . . .	145
9.7 Reactor-off data energy stability . . . . .	146
9.8 First PROSPECT IBD prompt energy spectrum from HFIR . . . . .	147
9.9 Prompt spectrum model with Huber prediction . . . . .	148

9.10 Full covariance matrix for the PROSPECT spectrum analysis . . .	149
9.11 PROSPECT measured spectrum compared to adjusted Huber spectral model . . . . .	151

## LIST OF ABBREVIATIONS

Abbreviation/Symbol	Definition
ADC	Analog-Digital Converter
BNL	Brookhaven National Laboratory
BiPo	Bismuth-Polonium decay
CC interaction	Charged Current interaction
DAQ	Data AcQuisition
ENSDF	Evaluated Nuclear Structure Data File
FEP	Fluorinated Ethylene Propylene
HEU reactor	High Enrichment $^{235}\text{U}$
HFIR	High Flux Isotope Reactor
HV	High Voltage
IBD	Inverse Beta Decay
ILL	Institut Laue-Langevin
JENDL	Japanese Evaluated Nuclear Data Library
LEU reactor	Low Enrichment $^{235}\text{U}$
LLNL	Lawrence Livermore National Laboratory
LS	Liquid Scintillator
$^6\text{LiLS}$	$^6\text{Li}$ loaded Liquid Scintillator
MC	Monte-Carlo simulation
NC interaction	Neutral Current interaction
OCS	Optical Calibration System
ORNL	Oak Ridge National Laboratory

PE	Photoelectron
PG4	PROSPECT-Geant4 simulation package
PID	Particle type Identification
PMNS matrix	Pontecorvo-Maki-Nakagawa-Sakata matrix
PMT	Photomultiplier Tube
PTFE	PolyTetraFluoroEthylene
PSD	Pulse Shape Discrimination
QC	Quality Control
QA	Quality Assurance
R&D	Research and Development
RAA	Reactor Antineutrino Anomaly
RnPo	Radon-Polonium decay
S:B	Signal to Background ratio
UV	Ultraviolet
ZLE	Zero Length Encoding

## ABSTRACT

Neutrinos from nuclear fission reactors have been widely studied in particle and nuclear physics. In the last ten years, the antineutrino flux and spectrum were measured independently by short baseline reactor experiments. Both flux and spectrum measurements showed discrepancies compared to theoretical models based on historical measurements and nuclear databases. These discrepancies hint at sterile neutrino oscillation at the eV mass scale, as well as an incomplete theoretical model. PROSPECT, the Precision Reactor Oscillation and Spectrum experiment, was built to probe for sterile neutrino oscillations and precisely measure the reactor antineutrino spectrum from a highly  $^{235}\text{U}$  enriched reactor. The PROSPECT antineutrino detector is an optically segmented liquid scintillator detector deployed at seven meter to nine meter from the High Flux Isotope Reactor at Oak Ridge National Laboratory. This dissertation details the analysis to calibrate the energy scale of the PROSPECT antineutrino detector, an essential step for both the oscillation and spectrum measurements. To characterize the nonlinear detector energy response, a unique calibration and analysis strategy was developed to overcome challenges brought on by particle multi-segment scattering within the PROSPECT detector. With the calibrated scale for energy reconstruction, PROSPECT measured of the antineutrino spectrum from a  $^{235}\text{U}$ -burning reactor.

## CHAPTER 1

### AN INTRODUCTION TO NEUTRINOS

Neutrinos are leptons carrying neutral electrical charge. Its neutral lepton nature makes it a fermion that only interacts with other particles through weak interactions. From decades of experimental study, it is known that neutrinos come in three flavors, and have antiparticle analogs. The neutrino was long assumed to be a massless particle until the discovery of neutrino oscillations, which proved that that at least two of the neutrinos have mass. Measurements of neutrino oscillation also showed that neutrino mass eigenstates are not orthogonal with neutrino flavor states, and are significantly mixed with neutrino flavors, in contrast to quark mixing.

Although many theoretical and experimental efforts involved with neutrinos have been completed, the discovery and measurements of neutrinos have brought even more experimental questions into focus: the absolute mass measurement of neutrinos, the observation of lepton CP-violation through neutrino oscillation, probing neutrino-less double beta decay, and the new beyond standard model neutrino states.

Thanks to its rare reaction with other particles, neutrino detection has been applied to aid the research of nuclear and astrophysics. Reactor antineutrino detectors are able to remotely monitor a fission reactor's nuclear structure [1,2]. The neutrino observatory has become an essential component in the multi-messenger astrophysics observations [3].

#### 1.1 Beta-decay

The study of neutrino physics began with studies of  $\beta$ -decay. During early

research on radioactive decay, the process of  $\beta$ -decay was assumed to be



With energy and momentum conservation, one can easily conclude that reaction should produce a  $\beta$  with single kinetic energy. In 1914, Chadwick found the energy spectrum of the  $\beta$  particle produced from radioactive decay was continuous [4], different from the  $\alpha$  and  $\gamma$  products that have a sharp distribution. Particularly, Ellis and Wooster established the proof of continuous  $\beta$  spectrum measurement of  $^{210}\text{Bi}$  [5] shown in Figure 1.1. To preserve conservation of energy, in 1932, Pauli postulated the existence of a new particle in his *Open Letter to The Group of Radioactive People at the Gauverein Meeting in Tübingen*, by calling it a “neutron”, as an additional neutral spin- $\frac{1}{2}$  particle produced in  $\beta$ -decay.

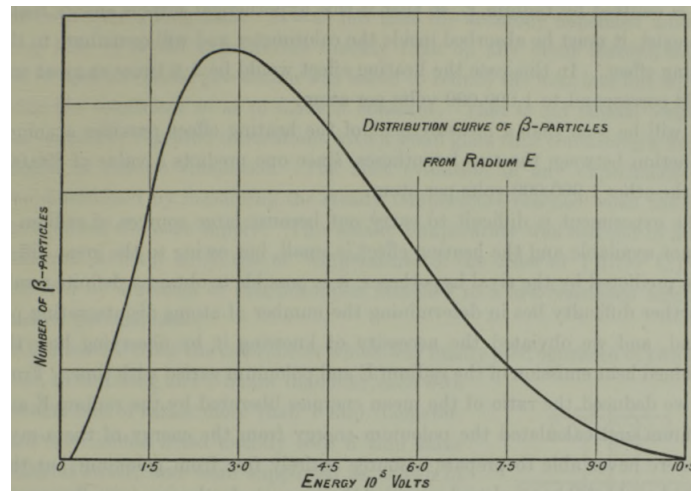


Figure 1.1. The continuous  $\beta$  energy spectrum measured from  $^{210}\text{Bi}$   $\beta$ -decay [5].

Soon after the discovery of the neutron (the neutral nucleon), Fermi developed his theory of beta decay in 1934 [6], where the weak interaction was theorized. In Fermi’s theory of beta decay, neutrinos were incorporated as a massless daughter particle that carries away a part of the energy of a neutron beta decay:



where  $\nu$  was named as ‘neutrino’ for the first time. The neutrino generated in this process was later found to be  $\bar{\nu}_e$  (electron antineutrino) to conserve lepton number in this process.

## 1.2 The Discovery of Neutrinos

When he proposed the neutrino’s existence, Pauli stated they were particles that “cannot be detected.” The introduction of the weak interaction meant that neutrinos can interact with other particles by exchanging W or Z bosons. Among many types of neutrino-nucleon and -lepton interactions, neutrinos can interact similarly as in  $\beta$ -decay:

$$\bar{\nu}_e + p \rightarrow n + e^+, \quad (1.3)$$

which is named as inverse beta decay (IBD), a quasielastic charged-current (CCQE) reaction between  $\bar{\nu}_e$  and proton mediated by the exchange of a W boson. The cross-section of the IBD reaction is

$$\sigma_{IBD} \simeq \frac{G_F^2 |V_{ud}|^2}{\pi} (1 + 3g_A^2) E_\nu^2, \quad (1.4)$$

where  $G_F$  is the Fermi constant,  $V_{ud}$  is the up-down quark mixing magnitude, and the Goldberger–Treiman relation  $g_A \simeq 1.27$ . Equation [1.4](#) estimates the IBD cross-section at the scale of  $\sim 10^{-43} \frac{p_e E_e}{\text{MeV}^2}$  ( $\text{cm}^2$ ) [\[7\]](#), where  $p_e$  and  $E_e$  are momentum and energy of the IBD produced positron. Such a rare interaction rate brought a significant challenge in neutrino detection that requires both high neutrino production from the source and a vast amount of protons in the detector.

In 1956, Cowan and Reines discovered neutrinos through the detection of IBD [\[8\]](#). The neutrinos detected were  $\bar{\nu}_e$  produced from the  $\beta$ -decay of daughter isotopes of the nuclear fission reactor at the Savannah River nuclear power plant. To detect the IBD signals, two target tanks filled with  $^{108}\text{Cd}$  loaded water were deployed in two gaps made by three vertically aligned liquid scintillator (LS) detectors. The

signature of the IBD process was the time coincidence between the positron and neutron produced in the reaction. When a proton in the water tank was hit by  $\bar{\nu}_e$ , the produced positron annihilated with an electron into a pair of 0.511 MeV  $\gamma$ , and the neutrons were mostly captured by  $^{108}\text{Cd}$  within 5  $\mu\text{s}$ , emitting capture  $\gamma$  rays with total energy from 3 MeV to 10 MeV. As they interacted in the LS, the  $\gamma$  rays in the LS generate scintillation photons that are eventually collected by the 110 photomultiplier tubes (PMTs) in each LS detector. By detecting  $\gamma$  rays from the target tanks with time coincidence, the Cowan and Reines experiment observed 1013  $\bar{\nu}_e$  events in 900 hours reactor-on data acquisition.

The conservation of lepton flavor requires that  $\beta$ -decay only produce  $\bar{\nu}_e$ . This conservation also forbids interactions like  $\bar{\nu}_\mu + p \rightarrow n + e^+$ , meaning a  $\nu_\mu$ 's (muon neutrino's) interaction with a nucleon cannot produce an electron [9, 10]. In 1962, Schwartz, Lederman, and Steinberger induced high energy  $\nu_\mu/\bar{\nu}_\mu$  produced from the decay of the boosted  $\pi^\pm$  [11]. With a 10 ton spark chamber consisting of 90 aluminum plates, the experiment at Brookhaven National Laboratory was able to distinguish electrons and muons produced from  $\nu_\mu/\bar{\nu}_\mu$ 's interactions with nucleons. This experiment discovered  $\nu_\mu$  by finding that only  $\mu^\pm$  were detected in the chamber.

In 2000, the DONUT collaboration at Fermilab discovered  $\nu_\tau$  (tau neutrino) from the decay of boosted  $D_s^- \rightarrow \tau^- + \bar{\nu}_\tau$ . Since the discovery of  $\nu_\tau$ , the family of neutrinos in Standard Model has six members:  $\nu_e$ ,  $\nu_\mu$ ,  $\nu_\tau$ , and their antiparticles.

### 1.3 Observation of Neutrino Oscillations

Fermi also stated the neutrino should be either massless or extremely light in his study of  $\beta$ -decay [6]. Following Yang and Lee's discussion of the parity conservation question [12], Wu discovered that weak interaction violates parity symmetry by observing  $\beta$  momentum direction preference in the  $\beta$ -decay of polarized  $^{60}\text{Co}$  [13].

The parity violation of  $\beta$ -decay restricts the neutrino helicity to be only left-handed (and antineutrino helicity to be only right-handed). Therefore, massless neutrinos and antineutrinos were seemingly preferred in nature to obey the proper representation of the Lorentz group. The Standard Model was built with the assumption of massless neutrinos. However, the experimental observation of neutrino oscillations proved neutrinos have nonzero masses.

The research of the oscillating neutrino began from the discovery of the solar neutrino problem. In 1968, Davis *et al.* organized a solar neutrino experiment aiming to detect  $\nu_e$  from fusion reactions in the sun [14]. This experiment used a target containing 390000 liters of  $C_2Cl_4$  in the Homestake mine to detect the appearance of  $^{37}Ar$  in the  $^{37}Cl(\nu_e, e^-)^{37}Ar$  reaction. The solar neutrino problem arose when the measured flux of  $\nu_e$  was found to be one third of that predicted by the Standard Solar Model. In the following decades, more solar neutrino flux measurements, including GALLEX [15], GNO [16], SAGE [17], and Kamiokande [18], observed less solar  $\nu_e$  flux than expected. Also, atmospheric neutrino measurements from the IMB [19] and Kamiokande [20] experiments reported fewer atmospheric neutrinos than predicted, which is referred to as the *Atmospheric Neutrino Anomaly*. These deficits with respect to theoretical models provided experimental hints of the neutrino oscillation.

Neutrino oscillation was authoritatively first observed by the Super-K experiment [21] in 1998. Using a water Cherenkov detector with 50000 tons of pure water and 13000 PMTs, the experiment observed the atmosphere  $\nu_\mu$  flux difference among a large range of zenith angles, as shown in Figure 1.2. The difference of atmospheric neutrino flux was the result of  $\nu_\mu$ 's oscillating into other flavors while traveling through the earth prior being collected in the detector.

In 2001, the SNO experiment [22] deployed a heavy-water Cherenkov detector that was able to detect charged-current (CC), neutral-current (NC) and elastic scat-

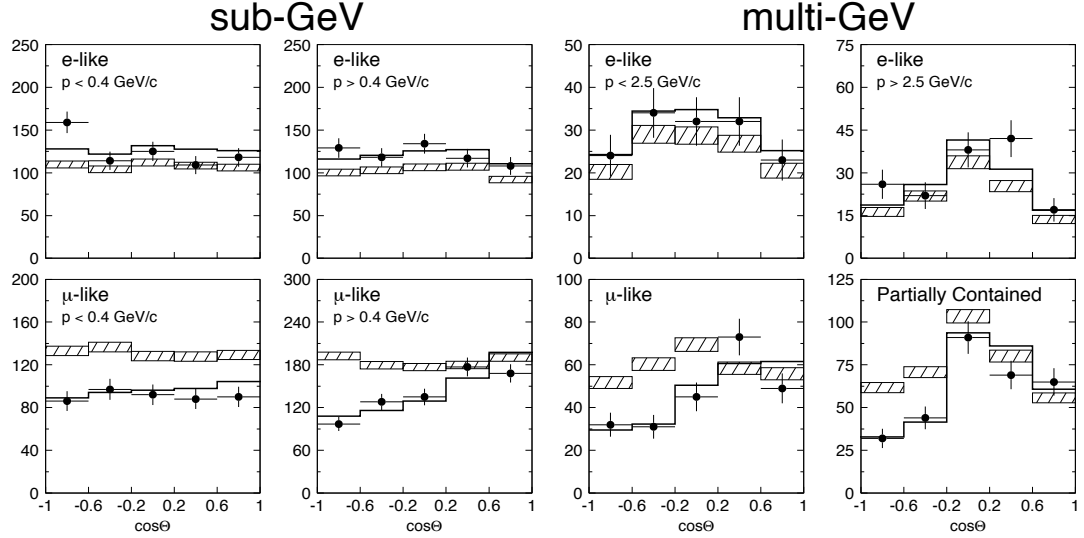


Figure 1.2. The flux of  $e$ -like and  $\mu$ -like events measured by the Super-K experiment [21]. The flux of  $\mu$ -like events, correlated to the number of  $\nu_\mu$  collected, varies significantly to zenith angle. The solid line (shaded region) represents the Monte-Carlo (MC) simulation with (without) the model of neutrino oscillation.

tering (ES) to detect solar neutrinos of all flavors in comparison with the  $\nu_e$  flux. If neutrino oscillates among flavors, the solar  $\nu_e$  will oscillates into other flavors while conserving their total flux. As shown in Figure 1.3, the experiment confirmed solar neutrino oscillation by comparing neutrino flux as measured with different scattering modes. Super-K and SNO experiments provided substantial experimental evidence of neutrino oscillation and resolved the solar neutrino problem and atmospheric neutrino anomaly.

#### 1.4 Massive Neutrinos

The discovery of neutrino oscillation implies that neutrinos have mass. Although the natural origin of neutrino mass is undetermined, neutrinos can obtain mass through the Higgs mechanism similar to other leptons. Under the assumption of the neutrino being Dirac fermion (particle distinct from antiparticle), a Higgs-

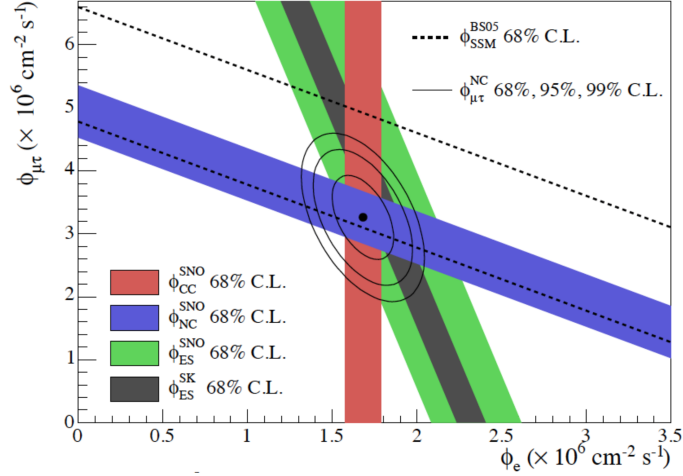


Figure 1.3. The flux of different scattering modes of solar neutrinos measured by SNO [22]. The all-flavor flux (NC and ES) agreed. The day-night flux indicates  $\nu_e$ 's oscillation into other flavors.

lepton Yukawa Lagrangian term can be expressed as

$$\mathcal{L}_H = - \left( \frac{v + H}{\sqrt{2}} \right) \left[ \bar{l}'_L Y'^l l'_R + \bar{\nu}'_L Y'^\nu \nu'_R \right], \quad (1.5)$$

where  $v$  is the Higgs vacuum expectation value (VEV),  $H$  is the Higgs field, and  $Y$  is the Yukawa coupling matrix. The matrix can be diagonalized with the unitary matrices  $V_L$  and  $V_R$ .

$$V_L^\dagger Y' V_R = Y, \quad \text{with } Y_{kj} = y_k \delta_{kj} \quad (k, j = 1, 2, 3), \quad (1.6)$$

where  $y_k$  is the eigenvalue of Yukawa coupling matrix. The three-generation neutrino mass mixing is defined as:

$$\nu'_L \rightarrow V_L^{\nu\dagger} \nu'_L = \begin{pmatrix} \nu_{1L} \\ \nu_{2L} \\ \nu_{3L} \end{pmatrix} \quad \text{and} \quad \nu'_R \rightarrow V_R^{\nu\dagger} \nu'_R = \begin{pmatrix} \nu_{1R} \\ \nu_{2R} \\ \nu_{3R} \end{pmatrix}. \quad (1.7)$$

Considering  $l_\alpha = l_{\alpha L} + l_{\alpha R}$  and  $\nu_k = \nu_{kL} + \nu_{kR}$ , the Lagrangian can be rewritten as

$$\begin{aligned} \mathcal{L}_H &= - \left( \frac{v+H}{\sqrt{2}} \right) \left[ \sum_{\alpha=e,\mu,\tau} y_\alpha^l \bar{l}_{\alpha L} l_{\alpha R} + \sum_{k=1,2,3} y_k^\nu \bar{\nu}_{kL} \nu_{kR} \right] \\ &= - \sum_{\alpha=e,\mu,\tau} \frac{y_\alpha^l v}{\sqrt{2}} \bar{l}_\alpha l_\alpha - \sum_{k=1,2,3} \frac{y_k^\nu v}{\sqrt{2}} \bar{\nu}_k \nu_k - \sum_{\alpha=e,\mu,\tau} \frac{y_\alpha^l}{\sqrt{2}} \bar{l}_\alpha l_\alpha H - \sum_{k=1,2,3} \frac{y_k^\nu}{\sqrt{2}} \bar{\nu}_k \nu_k H. \end{aligned} \quad (1.8)$$

Since  $\nu_k = \nu_{kL} + \nu_{kR}$ , the Dirac mass term of neutrino is simplified as

$$\begin{aligned} \mathcal{L}_{mass}^D &= - \sum_{k=1,2,3} m_k^D \bar{\nu}_k \nu_k + \text{H.c.} \\ &= - \sum_{k=1,2,3} m_k^D (\bar{\nu}_{kL} \nu_{kR} + \bar{\nu}_{kR} \nu_{kL}) + \text{H.c.}, \end{aligned} \quad (1.9)$$

where the Dirac mass of the neutrino  $m_k^D = \frac{y_k^\nu v}{\sqrt{2}}$  and  $\bar{\nu}_{kL} \nu_{kL} = \bar{\nu}_{kR} \nu_{kR} = 0$ . This mechanism for neutrinos to obtain mass involves a right-handed neutrino  $\nu_R$ , also referred to as the *sterile neutrino* for its incapability of interacting under the parity-violating weak force.

Because of its neutral nature, neutrinos are also candidates to be Majorana fermions (the particles being the antiparticles of themselves). Under this condition, the neutrino field is

$$\nu = \nu_L + \mathcal{C} \bar{\nu}_L^T, \quad (1.10)$$

where neutrino  $\mathcal{C}$  is a charge conjugate matrix. The Majorana mass term of the lepton Lagrangian can be written as

$$\mathcal{L}_{mass}^M = \frac{1}{2} m_L \nu_L^T \mathcal{C}^\dagger \nu_L + \text{H.c.}, \quad (1.11)$$

in which  $m^L$  is the left-handed Majorana mass. The Majorana mass term of neutrino avoids the assumption of a right handed neutrino.

However, it is theoretically allowed that both right handed neutrinos and Majorana neutrinos exist. In this case, a more general neutrino mass term for single

neutrino scenario is defined as

$$\begin{aligned}\mathcal{L}_{mass}^{D+M} &= -m_D(\bar{\nu}_L\nu_R + \bar{\nu}_R\nu_L) + \frac{1}{2}m_L\nu_L^T\mathcal{C}^\dagger\nu_L + \frac{1}{2}m_R\nu_R^T\mathcal{C}^\dagger\nu_R + \text{H.c.} \\ &= \frac{1}{2}(\bar{\nu}_L^C \quad \bar{\nu}_R) \begin{pmatrix} m_L & m_D \\ m_D & m_R \end{pmatrix} \begin{pmatrix} \nu_L \\ \nu_R^C \end{pmatrix} + \text{H.c.}\end{aligned}\quad (1.12)$$

In a special case, when  $m^D \ll m_R$  and  $m_L = 0$ , Equation [1.12](#) can be diagonalized as

$$\mathcal{L}_{mass}^{D+M} = \frac{1}{2}(\bar{\nu}_1 \quad \bar{\nu}_2) \begin{pmatrix} \frac{m_D^2}{m_R} & \\ & m_R \end{pmatrix} \begin{pmatrix} \nu_1 \\ \nu_2 \end{pmatrix} + \text{H.c.}\quad (1.13)$$

This is called the Type-I seesaw mechanism, a possible explanation of the tiny mass of the left-handed neutrino [\[23,24\]](#).

## 1.5 Theory of Neutrino Oscillation

The theoretical study of neutrino oscillations started in the 1950s. Pontecorvo [\[25,26\]](#) proposed neutrino oscillation inspired by observation of  $K^0 \leftrightarrow \bar{K}^0$  oscillations. In 1967, Maki, Nakagawa, and Sakata discussed the theory of two-neutrino flavor mixing [\[27\]](#). Later in 1969, Gribov and Pontecorvo explicitly developed the theory of neutrino oscillation with mass state mixing [\[28\]](#). For massive neutrinos, the neutrino portion of the Lagrangian can be expressed analogously to other massive particles:

$$\mathcal{L}_\nu = - [m_\alpha^\nu \bar{\nu}_\alpha \nu_\alpha + m_\beta^\nu \bar{\nu}_\beta \nu_\beta + m_\alpha^\nu m_\beta^\nu (\bar{\nu}_\alpha \nu_\beta + \bar{\nu}_\beta \nu_\alpha)] \quad (\alpha, \beta = e, \mu, \tau). \quad (1.14)$$

This equation can be rewritten as

$$\mathcal{L}_\nu = \bar{\nu}_\alpha \mathcal{M}^\nu \nu_\beta. \quad (1.15)$$

where the  $\mathcal{M}^\nu$  can be diagonalized. The conversion between the two matrix expressions above transforms the flavor states of neutrinos to mass states by a unitary

matrix  $U$ :

$$\begin{pmatrix} \nu_\alpha \\ \nu_\beta \end{pmatrix} = \begin{pmatrix} \cos \theta & \sin \theta \\ -\sin \theta & \cos \theta \end{pmatrix} \begin{pmatrix} \nu_k \\ \nu_l \end{pmatrix}. \quad (1.16)$$

When  $\theta \neq 0$ , this transformation is a two generation mixing of neutrino mass eigenstates and neutrino flavors, meaning a neutrino's flavor is not orthogonal to its mass eigenstates. This matrix can be expanded to three neutrino mixing with the unitary matrix  $U_{PMNS}$ , the Pontecorvo-Maki-Nakagawa-Sakata (PMNS) matrix, a neutrino equivalent to the CKM mixing matrix of the quark sector. In addition to the 3x3 angular transformation, this matrix also includes a CP-violation phase factor  $\delta_{CP}$  and a diagonal mixing matrix of Majorana neutrino terms  $D_{Majorana}$ , where  $\xi_1$  and  $\xi_2$  are Majorana phase terms. The three generation neutrino mixing matrix is

$$\begin{aligned} U &= U_{PMNS} \cdot D_{Majorana} \\ &= \begin{pmatrix} U_{e1} & U_{e2} & U_{e3} \\ U_{\mu1} & U_{\mu2} & U_{\mu3} \\ U_{\tau1} & U_{\tau2} & U_{\tau3} \end{pmatrix} \\ &= \begin{pmatrix} 1 & & \\ & c_{23} & s_{23} \\ & -s_{23} & c_{23} \end{pmatrix} \begin{pmatrix} c_{13} & & s_{13}e^{-i\delta_{CP}} \\ & 1 & \\ -s_{13}e^{i\delta_{CP}} & & c_{13} \end{pmatrix} \begin{pmatrix} c_{12} & s_{12} \\ -s_{12} & c_{12} \\ & & 1 \end{pmatrix} \\ &\cdot \begin{pmatrix} e^{i\xi_1/2} & & \\ & e^{i\xi_2/2} & \\ & & 1 \end{pmatrix}, \end{aligned} \quad (1.17)$$

where  $s_{ij} = \sin \theta_{ij}$  and  $c_{ij} = \cos \theta_{ij}$ .

Hence, the flavor eigenstates of the neutrino can be described as a sum of the

mass states with a matrix element form  $U_{PMNS}$ :

$$|\nu_\alpha\rangle = \sum_{k=1,2,3} U_{\alpha k}^* |\nu_k\rangle. \quad (1.18)$$

Using the time-dependent Schrödinger equation, the time evolution of neutrino flavor is expressed as

$$|\nu_\alpha(t)\rangle = \sum_{k=1,2,3} U_{\alpha k}^* e^{-i(E_k)t} |\nu_k\rangle. \quad (1.19)$$

Therefore, the probability of a neutrino oscillating from one flavor to the other is

$$\begin{aligned} P_{\nu_\alpha \rightarrow \nu_\beta} &= |\langle \nu_\beta | \nu_\alpha(t) \rangle|^2 \\ &= \sum_{k,j} U_{\alpha k}^* U_{\beta k} U_{\alpha j} U_{\beta j}^* e^{-i(E_k - E_j)t} \\ &= \sum_{k,j} U_{\alpha k}^* U_{\beta k} U_{\alpha j} U_{\beta j}^* \exp\left(-i \frac{\Delta m_{kj}^2 L}{2E}\right), \end{aligned} \quad (1.20)$$

where  $\Delta m_{kj}^2 = m_k^2 - m_j^2$ ,  $L$  is the neutrino travelling distance, and  $E$  is the kinetic energy of the neutrino. This equation proves that a nonzero neutrino oscillation probability requires the mixing of massive neutrinos. It also shows that the phase of the neutrino oscillation depends on the factor  $\frac{\Delta m_{kj}^2 L}{2E}$ , resolving both the solar neutrino problem and the atmospheric neutrino anomaly.

The probability shown in Equation [1.20](#) can be generalized to any neutrino flavor transition in oscillation as

$$\begin{aligned} P_{\nu_\alpha \rightarrow \nu_\beta} &= \delta_{\alpha\beta} - 4 \sum_{k>j} \text{Re} [U_{\alpha k}^* U_{\beta k} U_{\alpha j} U_{\beta j}^*] \sin^2 \left( \frac{\Delta m_{kj}^2 L}{4E} \right) \\ &\quad \pm 2 \sum_{k>j} \text{Im} [U_{\alpha k}^* U_{\beta k} U_{\alpha j} U_{\beta j}^*] \sin \left( -i \frac{\Delta m_{kj}^2 L}{2E} \right). \end{aligned} \quad (1.21)$$

The imaginary component is positive for neutrinos and negative for antineutrinos. In two neutrino mixing, Equation [1.20](#) can be simplified as

$$P_{\nu_\alpha \rightarrow \nu_\beta} = \sin^2 2\theta \sin^2 \left( 1.27 \frac{\Delta m^2 L}{E} \right) \quad (1.22)$$

to calculate the appearance probability of one flavor during neutrino oscillation in vacuum. Similarly, the survival probability of the original neutrino flavor can be written as

$$P_{\nu_\alpha \rightarrow \nu_\alpha} = 1 - \sin^2 2\theta \sin^2 \left( 1.27 \frac{\Delta m^2 L}{E} \right). \quad (1.23)$$

The probability Equations [1.22](#) and [1.23](#) are frequently used as a theoretical tool in neutrino oscillation experiments to calculate expected levels of oscillation.

## 1.6 Measurements of Neutrino Oscillation

Experimental efforts have been made in the past two decades to determine the key neutrino oscillation parameters. By measuring the flux of disappeared or appeared neutrinos at various baselines, experiments have been able to measure the oscillation parameters, including  $\theta_{23}$ ,  $\theta_{13}$ ,  $\theta_{12}$ ,  $\Delta m_{21}^2$ , and  $|\Delta m_{31}^2|$ .  $\theta_{12}$  and  $\Delta m_{21}^2$  were determined by the phenomenological analyses of solar neutrino flux measurements [29](#) and KamLAND reactor  $\bar{\nu}_e$  oscillation measurement [30](#). By measuring the disappearance of  $\nu_\mu$  and  $\bar{\nu}_\mu$  in atmospheric neutrino experiments [31,32](#), long baseline accelerator neutrino experiments [33-36](#), and neutrino telescope observation [37,38](#),  $\theta_{23}$  and  $|\Delta m_{31(32)}^2|$  have been measured.  $\theta_{13}$  has been thoroughly measured in  $\sim 1$  km scale baseline reactor  $\bar{\nu}_e$  flux measurements [39-41](#). The current preferred neutrino mass mixing parameters are listed in Table [1.1](#), where “normal” and “inverted” represents the two untested assumptions of the neutrino mass hierarchy. *Normal hierarchy* suggests  $\nu_1 < \nu_2 < \nu_3$  in mass. *Inverted hierarchy* suggests  $\nu_3 < \nu_1 < \nu_2$  in mass.

## 1.7 Future Tasks of Neutrino Experiments

The properties of massive neutrinos are of primary interest for future experimental research, as they are the first solid experimental evidence of physics beyond the Standard Model. Studies of the Dirac or Majorana nature of neutrinos are conducted worldwide. If neutrinoless double  $\beta$ -decay ( $0\nu\beta\beta$ ) is observed, neutrinos can

Table 1.1. Measured parameters of neutrino oscillation [42].

Parameters	Value	3- $\sigma$
$\sin^2(\theta_{12})$	0.297	0.250 – 0.354
$\sin^2(\theta_{23})$	0.425 (normal)	0.381 – 0.615
	0.589 (inverted)	0.384 – 0.636
$\sin^2(\theta_{13})$	0.0215 (normal)	0.0190 – 0.0240
	0.0216 (inverted)	0.0190 – 0.0242
$\Delta m_{21}^2 (10^{-5} \text{eV}^2)$	7.57	6.93 – 7.96
$ \Delta m_{31}^2  (10^{-3} \text{eV}^2)$	2.56 (normal)	2.45 – 2.69
	2.54 (inverted)	2.42 – 2.66

be determined as the first Majorana fermion ever detected. Several experiments are directly measuring the neutrino mass by searching the upper limit of  $\beta$  spectra from specific isotopes with very high energy resolution.

To resolve the neutrino mass hierarchy, observe leptonic CP violation, and search the light sterile neutrino, more precise measurements of neutrino oscillations from different sources at various baselines are needed. These studies involve precise measurement of different transition ratios in oscillation, high-resolution energy spectrum measurement, neutrino-antineutrino oscillation difference, and very short baseline oscillation measurements.

## CHAPTER 2

### REACTOR ANTINEUTRINOS

Neutrinos can be categorized by the sources they are generated from, including natural sources and artificial sources. The solar neutrino, relic neutrino, supernova neutrino, geo-neutrino, and atmospheric neutrino are neutrinos generated by natural cosmological or radioactive sources. Reactor antineutrinos (henceforth mentioned as *reactor neutrinos*) and accelerator neutrinos are human-made.

Reactor neutrino experiments have the advantages of

- Relatively high statistics;
- Easy-to-control experimental baselines;
- A relatively narrow range of neutrino energy.

Thus, reactor neutrino experiments have played an irreplaceable role in the history of neutrino detection and oscillation measurements.

#### 2.1 The Flux and Spectrum of Reactor Neutrinos

Reactor neutrinos are  $\bar{\nu}_e$  generated through  $\beta$ -decay of the daughter nuclei of the nuclear fission process. Since the discoveries of lepton number conservation and neutrino flavors, Equation [1.2](#) is rewritten as the decay of a neutron producing  $\bar{\nu}_e$ ,

$$n \rightarrow p + e^- + \bar{\nu}_e, \quad (2.1)$$

where the proton is contained in a daughter nucleus. The chain reaction of a nuclear reactor produces a great variety of fission produced isotopes that release their energy

through beta decay. One fission reaction naturally results in the emission of multiple neutrinos, most with kinetic energy ranging from 0 MeV to 10 MeV.

Fission reactions of most reactor cores are dominated by  $^{235}\text{U}$ , with other fission isotopes including  $^{238}\text{U}$ ,  $^{239}\text{Pu}$  and  $^{241}\text{Pu}$ . The spectrum of reactor neutrinos is expressed as

$$S(E_\nu) = \frac{W_{reactor}}{\sum_i \frac{f_i}{F} e_i} \sum_i \frac{f_i}{F} \left( \frac{dN_i}{dE_\nu} \right), \quad (2.2)$$

where  $W_{reactor}$  is the thermal power of the reactor,  $i$  is each of the four fission isotopes above,  $f_i/F$  is the relative fraction of each isotope,  $e_i$  is energy per fission, and

$$\frac{dN_i}{dE_\nu} = \sum_n Y_n(t) \left( \sum_j b_{n,j} \cdot P(E_\nu, E_0^{n,j}) \right), \quad (2.3)$$

which is the summed energy spectrum of each fission isotope. In Equation [2.3](#),  $Y_n(t)$  is cumulative fission yield,  $b_{n,j}$  are the  $\beta$ -branches, and  $P(E_\nu, E_0^{n,j})$  is the spectrum of each branch. A typical reactor has thousands of  $\beta$ -decay branches. By adding the neutrino spectra of these branches, one can predict the spectrum of neutrinos generated from a reactor, an illustration is shown in [Figure 2.1](#).

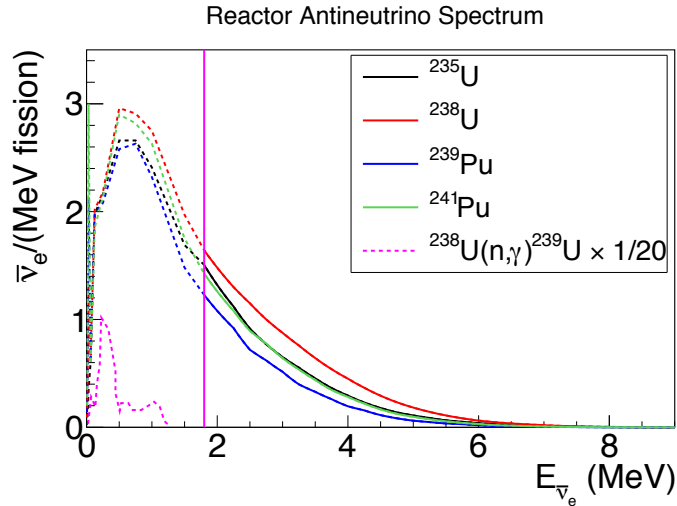


Figure 2.1. An illustration of a commercial reactor neutrino spectrum prediction [\[43\]](#).

Reactor neutrino experiments rely on the detection of the IBD process ex-

pressed in Equation [1.2](#). Because of the mass difference between the neutron and proton, the neutrino energy  $E_\nu$  must be above a threshold to trigger the IBD process, as

$$E_\nu \geq m_n + m_e - m_p \simeq 1.806\text{MeV}. \quad (2.4)$$

The kinetic energy of the IBD produced neutron  $T_n$  is on the keV scale. Thus, the total energy of an IBD positron can be expressed as

$$E_e = E_\nu - (m_n + T_n - m_p) \simeq E_\nu - 1.293\text{MeV}. \quad (2.5)$$

In an IBD detector, the  $e^+$  quickly annihilates with an atomic electron and emits two 0.511 MeV  $\gamma$  rays. The visible energy of an IBD positron in an ideal detector is

$$E_{vis} \simeq E_\nu - 0.782\text{MeV}, \quad (2.6)$$

which is a useful direct experimental conversion for the reconstruction of the  $\bar{\nu}_e$  energy. The cross-section of the IBD interaction is dependent on the neutrino energy and can be expressed as a function of positron energy

$$\sigma_{IBD} \simeq \frac{2\pi^2}{\tau_n m_e^5 f} E_e P_e = 10^{-43} \cdot \frac{E_e P_e}{\text{MeV}} \cdot \left(\frac{\tau_n}{886\text{s}}\right)^{-1} \text{cm}^2, \quad (2.7)$$

where  $\tau_n$  is the neutron lifetime and  $f$  is a phase space integral factor. Based on the theoretical neutrino spectrum (Equation [2.2](#)) and IBD cross-section (Equation [2.7](#)), a reactor neutrino experiment can expect a measured spectrum and flux as shown in Figure [2.2](#).

Reactor neutrino research has an interest in testing the success of nuclear and particle physics theories by comparing experimental measurements of reactor neutrino flux and spectra to predictions based on these theories. There are two methods to predict the absolute neutrino spectrum of a nuclear reactor:

- **The *ab initio* method:** The neutrino spectrum is calculated by Equation [2.2](#) and [2.3](#), where the ratio and the endpoint energy of each branch are extracted

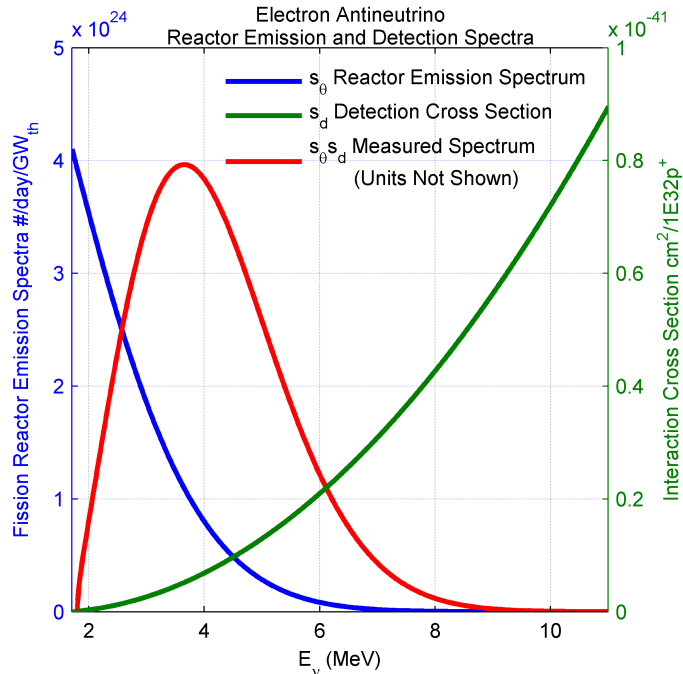


Figure 2.2. An illustration [44] of the detected neutrino energy spectrum in a reactor experiment. The detected spectrum is the multiplication of the emitted neutrino spectrum and IBD cross-section.

from data in nuclear databases, such as Evaluated Nuclear Structure Data File (ENSDF) [45], ENDF [46], and Japanese Evaluated Nuclear Data Library (JENDL) [47]. The predicted neutrino spectrum is the sum of the calculated  $\beta$ -spectra including a variety of theoretical corrections. The most-widely used neutrino spectrum of  $^{238}\text{U}$  is predicted in this way [48].

- **$\beta$ -conversion method:** Because the kinetic energy of the  $\beta$ -decay proton is negligibly small, the total  $\beta$ -decay end point energy  $E_0 \simeq E_\nu + E_e$ . The neutrino spectrum can thus be deduced from the experimental measurement of  $\beta$  energy from a fission reactor. In the 1980s, the  $^{235}\text{U}$ ,  $^{239}\text{Pu}$ , and  $^{241}\text{Pu}$  neutrino spectra were converted from the spectrum measurements of  $\beta$ s from the Institut Laue-Langevin (ILL) reactor [49–51]. The conversion was made by fitting the measured  $\beta$  spectrum with the sum of tens of hypothetical  $\beta$ -decay branches, then converting the spectrum of each  $\beta$  branch to a neutrino spectrum.

The detailed theoretical approaches are described in Section 2.3.

Successful neutrino flux and spectrum prediction and measurement made it possible for reactor neutrino experiments to test the nuclear model of fission reactors.

## 2.2 Historical Context of Reactor Neutrino Experiments

After the discovery of neutrinos via the detection by the Savannah reactor neutrino experiment [8], a hint of  $\bar{\nu}_e$  oscillation was discovered by Reines *et al* in 1980 [52]. Their experiment found in unexpected ratio between CC and NC interactions at the  $2\sigma - 3\sigma$  level of statistical significance, which suggests antineutrino oscillation. More reactor experiments were built to test  $\bar{\nu}_e$  oscillation over a wide variety of baseline by comparing neutrino flux to theoretical predictions or to measurements at different baselines, included in Table 2.1. These experiments attempted to observe neutrino oscillation via  $\bar{\nu}_e$  disappearance. The commonly used methods are to compare the observed neutrino flux to the expected flux, or to compare the relative flux/spectrum difference at different baselines.

The experiments listed in Table 2.1 cover different regions in the  $(\Delta m^2, \sin^2 \theta)$  parameter space of neutrino oscillations. The CHOOZ and Palo Verde experiments narrowed the allowed range of the parameter space to  $\sin^2 2\theta_{13} \leq 0.18$  for  $|\Delta m_{13}^2| \geq 2 \times 10^{-3} \text{ eV}^2$ , these results indicated that  $\nu_\mu \rightarrow \nu_e$  oscillation provided only a small contribution to the atmospheric neutrino anomaly.

In 2002, the KamLAND experiment [30, 65] confirmed reactor neutrino oscillation via a spectrum measurement of  $\bar{\nu}_e$  from 53 reactors around Japan (also 5% in South Korea and 1% from other reactors), with 180 km average baseline. The KamLAND experiment utilized a spherical detector with filled about 3000 ton of LS deployed in the Kamioka mine in Japan. The IBD positron and neutron signals were collected by 1879 inward-facing photomultiplier tubes (PMTs) on the surface of the

Table 2.1. An overview of historical reactor experiments searching for  $\bar{\nu}_e$  oscillation in baseline from  $\sim 10$  m to  $\sim 100$  km. The absolute flux ratios were calculated by comparing experimental measurements to the expected fluxes. The relative flux indicates the ratio of neutrino flux measured by detectors at different baselines.

Experiment	Baseline	Absolute flux	Relative flux	Reference
ILL	8.76 m	$0.955 \pm 0.115$		[53]
	37.9 m	$1.018 \pm 0.06$		
Gösgen	45.9 m	$1.045 \pm 0.06$		[54]
	64.7 m	$0.975 \pm 0.06$		
Rovno	18.3 m to 25.3 m	$0.964 \pm 0.068$		[55]
Krasnoyarsk	57 m to 231 m	$0.99 \pm 0.05$	$0.86 \pm 0.15$	[56]
	14 m	$0.988 \pm 0.05$		
Bugey	40 m	$0.994 \pm 0.05$		[57]
	95 m	$0.913 \pm 0.13$		
Savannah River	18 m	$0.987 \pm 0.038$		[58]
	4 m	$1.055 \pm 0.038$		
CHOOZ	1 km	$1.01 \pm 0.04$		[59–61]
Palo Verde	750 m to 890 m	$1.04 \pm 0.09$		[62–64]
KamLAND	80 km to 800 km	$0.658 \pm 0.06$		[30, 65]

detector. Similar to the Cowan-Reines experiment [8], KamLAND used positron-neutron time coincidence to tag the IBD interaction candidates, with the prompt positron signal followed by a delayed  $\gamma$  signal from  $n$ -H capture in the detector. With 162 ton-yr exposure, the KamLAND experiment observed neutrino oscillation at very long baselines by comparing the detected neutrino flux to the neutrino flux predicted by the ILL+Vogel model [48–51] shown in Figure 2.3(a). KamLAND also observed oscillation behavior dependent on the experimental  $L/E$  ratio, as shown in Figure 2.3(b).

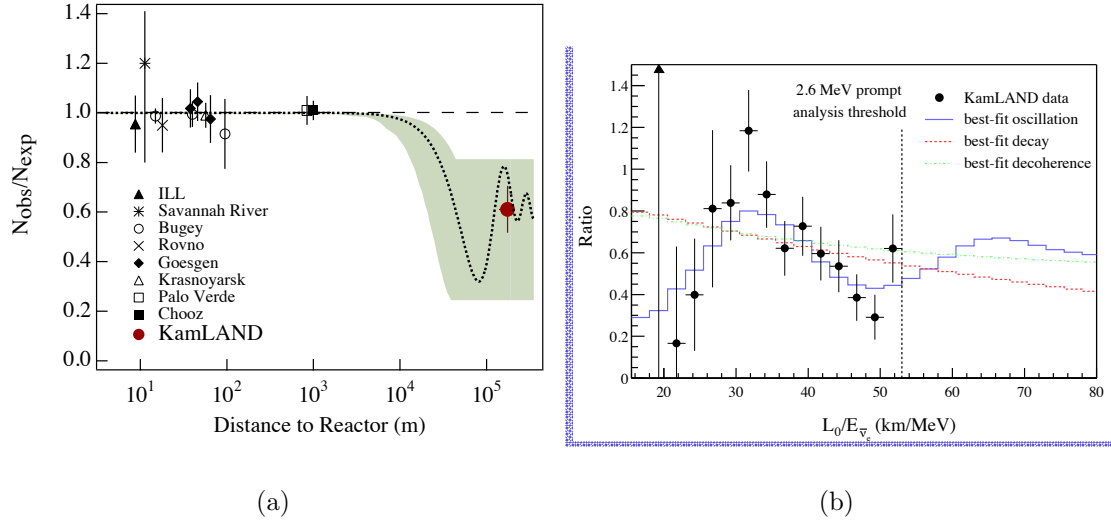


Figure 2.3. Observation of reactor neutrino oscillation by KamLAND [65]. (a) The ratio of the KamLAND observed neutrino flux to ILL+Vogel prediction. (b) The ratio of KamLAND measured  $L_0/E$  spectrum to the no oscillation prediction with average baseline  $L_0 = 180$  km, indicating oscillation behavior with respect to  $L_0/E$  of  $\bar{\nu}_e$ . This result also disfavored neutron decay and neutrino decoherence models made based on atmosphere neutrino experiments.

Another milestone in reactor neutrino experiments is the precise measurement of the  $\theta_{13}$  mixing angle. The medium baseline experiments, CHOOZ [61], Parlo Verde [64], RENO [40], Daya Bay [39] and Double CHOOZ [41] attempted to measure  $\theta_{13}$  via observation of  $\bar{\nu}_e \rightarrow \bar{\nu}$  disappearance in baselines varying from several hundred meters to 1 km from commercial reactors. Following CHOOZ and Parlo Verde’s measurement of the  $\sin^2 2\theta_{13}$  upper bound, RENO, Daya Bay and Double CHOOZ

independently reported the measurement of a nonzero  $\theta_{13}$  mixing angle. The three  $\theta_{13}$  experiments all utilized Gd loaded LS detectors deployed at different baselines from groups of reactors. By comparing the  $\bar{\nu}_e$  flux between near and far detectors, these experiments measured the  $\bar{\nu}_e \rightarrow \bar{\nu}$  disappearance probability independently from the nuclear model of the reactor  $\bar{\nu}_e$  production. The result of the measurements are listed in Table [1.1](#). The commercial reactors utilized in these experiments contain low-enriched Uranium (LEU) fuel, whose fission isotope fractions and  $\bar{\nu}_e$  productions evolve with time.

Table 2.2. Overview of results from medium baseline reactor neutrino experiments that measured the  $\theta_{13}$  mixing angle [39-41](#).

Experiment	Baseline	Average Fission Fraction
Daya Bay	560 m to 1640 m	57.1% $^{235}\text{U}$ , 29.9% $^{239}\text{Pu}$ , 7.6% $^{238}\text{U}$ , 5.4% $^{241}\text{Pu}$
RENO	294 m to 1383 m	57.3% $^{235}\text{U}$ , 29.9% $^{239}\text{Pu}$ , 7.3% $^{238}\text{U}$ , 5.5% $^{241}\text{Pu}$
Double CHOOZ	1050 m	48.8% $^{235}\text{U}$ , 35.9% $^{239}\text{Pu}$ , 8.7% $^{238}\text{U}$ , 6.7% $^{241}\text{Pu}$

### 2.3 Reactor Antineutrino Anomaly

In addition to oscillation measurements, the  $\theta_{13}$  experiments also measured the absolute neutrino flux and spectrum of the commercial reactors. To provide precise models for these measurements, predictions of reactor neutrino flux and spectrum were revisited with both the *ab initio* method and the  $\beta$  conversion method.

The ‘Mueller’ hybrid model [66](#) first used to the *ab initio* method by reading the ENSDF and JENDL nuclear databases to sum the  $\bar{\nu}_e$  spectrum from well

measured  $\beta$  branches. This method then subtracted this summed  $\beta$  spectrum from the ILL measured spectrum. The remaining spectra were fitted with five effective branches similar to the  $\beta$  conversion method. This resulted in a calculated  $\bar{\nu}_e$  spectra for  $^{235}\text{U}$ ,  $^{238}\text{U}$ ,  $^{239}\text{Pu}$ , and  $^{241}\text{Pu}$ , with limited effects from hypothetical branches. The ‘Huber’ model [67] purely utilized the  $\beta$  spectra of  $^{235}\text{U}$ ,  $^{239}\text{Pu}$ , and  $^{241}\text{Pu}$  measured from the ILL reactor and applied the conversion method with higher-order theoretical corrections to the  $\beta$  spectra of the virtual decay branches. The theoretical corrections include the effect of electron-nucleus interactions, radiation effects, and weak magnetism corrections. With different approaches predicting the  $\bar{\nu}_e$  spectrum, the Mueller model of expected neutrino flux found 2.5% more than the ILL+Vogel model, and Huber model found a 3% increase in the neutrino flux prediction. However, the absolute flux measurements of the historical reactor experiments within 1 km baseline showed inconsistent measured neutrino flux with respect to either of the two predictions, as shown in Figure 2.4.

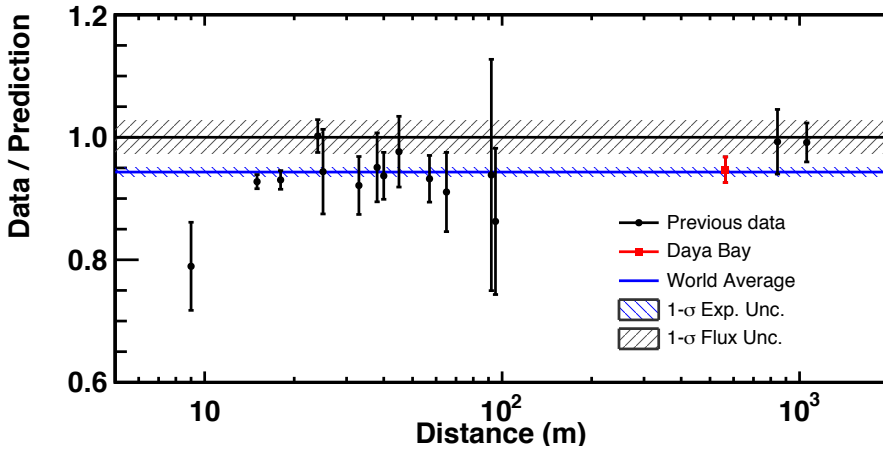


Figure 2.4. Historical reactor neutrino flux measurements [68]. The global average is a 5% to 6% deficit from Huber+Mueller predicted flux.

This measured neutrino flux deviation is referred to as the Reactor Antineutrino Anomaly (RAA) [69]. This anomaly suggests a systematic bias present in the theoretical aggregation method and/or the virtual branching approach in the con-

version from the ILL measured  $\beta$  spectrum. This disagreement of neutrino flux in the medium baselines can also be explained by a possible oscillation between  $\bar{\nu}_e$  and a light sterile neutrino. A 3+1 model of left-handed neutrino mixing with a sterile neutrino with  $\Delta m^2 \sim 1 \text{ eV}^2$  [69,70] scale was developed based on the disappearance rate shown in the flux deficit. The RAA best fit 3+1 neutrino oscillation parameters are shown in Figure 2.5.

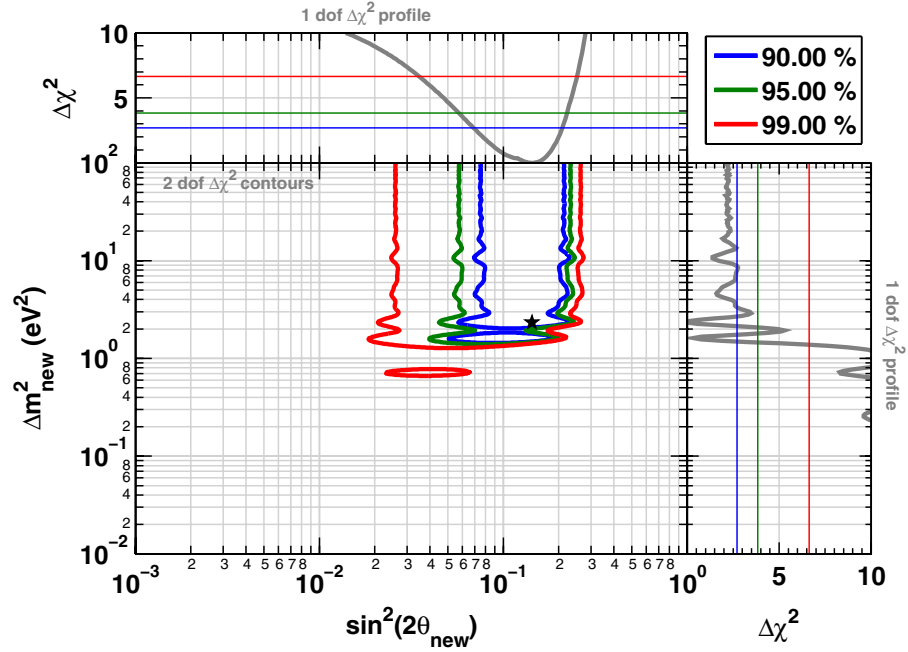


Figure 2.5. The allowed region for the parameters of sterile neutrino oscillation as a result of the flux deficit observed in RAA [69]. The best fit point suggests a  $\sin_{14}^2 2\theta = 0.14 \pm 0.08$  and  $|\Delta m^2| > 1.5 \text{ eV}^2$  (95% C.L.) of a 3+1 left hand neutrino and sterile neutrino mixing.

Independent of the flux deviation, the medium baseline experiments Daya Bay [1], Double CHOOZ [41], and RENO [40], also measured reactor neutrino spectra that disagree with the Huber and Mueller models, as shown in Figure 2.6. An 8% to 10% excess is observed in the 4 MeV to 6 MeV region of IBD positron energy, equivalent to 5 MeV to 7 MeV reactor neutrino energy. With high statistical significance, the spectral deficit observed hints at errors in the nuclear database used

to calculate the expected spectral shape. Additionally, the isotopic contribution to the flux and spectrum anomalies is unclear due to the mixture and evolution of the fission isotopes in the LEU reactors utilized by these experiments.

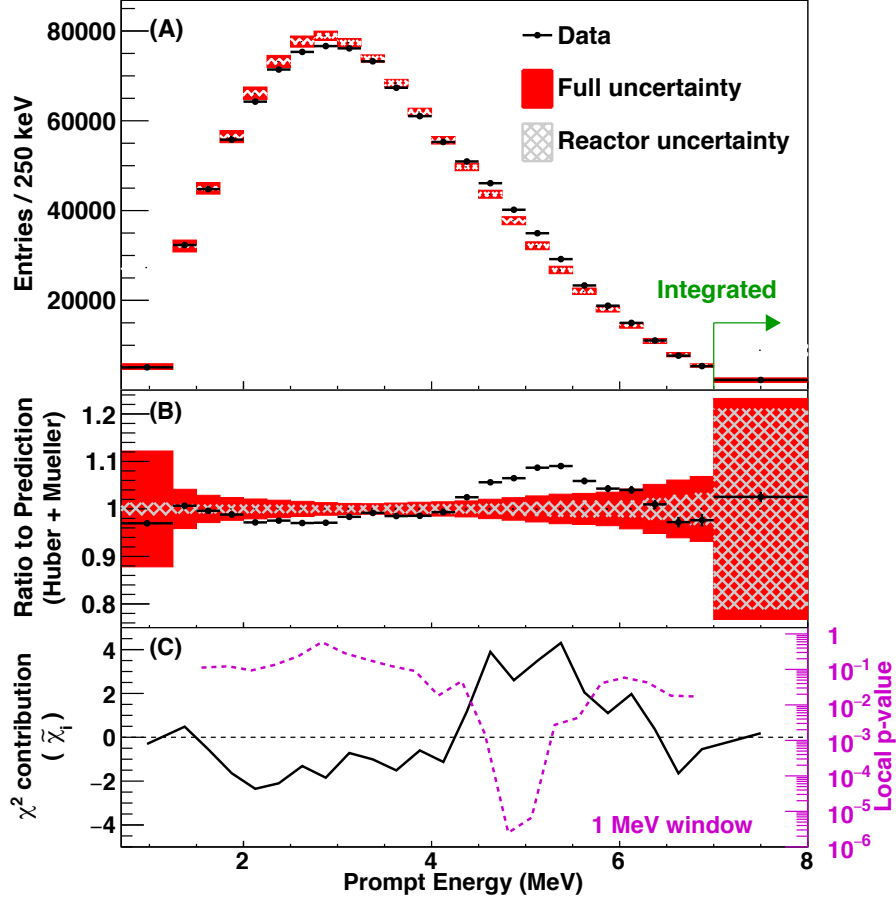


Figure 2.6. The IBD positron energy spectrum measured by Daya Bay experiment. The spectrum is the sum of IBD positron spectrum from four fission isotopes, which indicate an excess at 4 MeV to 6 MeV compared to the Huber+Mueller model with  $2.9 \sigma$  discrepancy.

## 2.4 Resolution of the RAA

Further studies include introducing forbidden transitions in  $\beta$ -decay branch spectra [71], and *ab initio* spectrum prediction with different nuclear databases [72]. These studies suggest larger systematic uncertainties than claimed in the Huber and Mueller model because of the lack of forbidden branch knowledge and errors in nuclear

databases. Phenomenological studies [73] based on historical reactor experiments were also made to resolve the RAA by comparing the neutrino flux of reactors with various fission fractions. The global fit of isotopic contributions to the flux deficit hint at  $^{235}\text{U}$  being the main contributor to the flux anomaly.

Multiple reactor neutrino measurements have been made to resolve the isotopic contribution of the flux and spectrum anomalies. Daya Bay and RENO experiments measured the reactor neutrino flux and spectrum evolution with fission fraction in their reactors [2, 74]. These measurements indirectly tested  $^{235}\text{U}$  and  $^{239}\text{Pu}$ 's contribution to the reactor neutrino flux and spectrum deficit. In these fuel evolution measurements, the reactor neutrino flux and spectrum's dependence on fission isotope is observed. The evolution of the spectrum weakly hints at a correlation between the  $^{235}\text{U}$ - $^{239}\text{Pu}$  transition and the local excess of the IBD spectrum.

The lack of definitive resolution to the RAA necessitates a direct measurement of the reactor neutrino flux and spectrum from a single fission isotope, particularly  $^{235}\text{U}$ . A very short baseline,  $^{235}\text{U}$ -only reactor neutrino experiment is preferred to measure the flux and spectrum of  $\bar{\nu}_e$  from the single fission isotope, as well as to simultaneously and independently probe possible eV-scale sterile neutrino oscillations.

## CHAPTER 3

### PROSPECT EXPERIMENT

The RAA described in Chapter 2 leads to the need for experiments capable of probing short baseline sterile neutrino oscillation, as well as directly measuring the flux and spectrum of a reactor with a high concentration of a single fission isotope. The experiment has to meet the requirements of :

- Sub-10 m baseline from a reactor with a compact reactor size.
- Fission reactor whose neutrino production is from a single isotope.
- Good IBD position reconstruction resolution for oscillation measurement.
- High energy resolution to precisely measure neutrino spectrum.

PROSPECT [75,76], the Precision Reactor Oscillation and SPECTrum experiment, was designed and built to directly measure the neutrino flux and spectrum from the HFIR located at ORNL [77]. PROSPECT's antineutrino detector (AD) covers baselines from 7 m to 9 m with a segmented LS volume. The goals of PROSPECT are to probe eV-scale sterile neutrino oscillation by the observation of  $\bar{\nu}_e$  disappearance, and to precisely measure the reactor neutrino spectrum from  $^{235}\text{U}$ .

### 3.1 HFIR Reactor

HFIR is a high enrichment  $^{235}\text{U}$  (HEU) research fission reactor whose  $^{235}\text{U}$  enrichment is 93% on average. The key parameters of the HFIR core relevant to PROSPECT neutrino measurements are listed in Table 3.1.

HFIR is a cylindrical fission reactor. Its compact size, as shown in Table 3.1 and Figure 3.1, is ideal for constraining the uncertainty in neutrino baselines. To

Table 3.1. The properties of HFIR.

Parameter	Value
Power	85 MW
Dimensions	435 mm (diameter) $\times$ 508 mm (height)
$^{235}\text{U}$ enrichment	93%
Neutrino source	$\sim 99\%$ from $^{235}\text{U}$
Reactor cycle	$\sim 25$ day on, $\sim 30$ day off

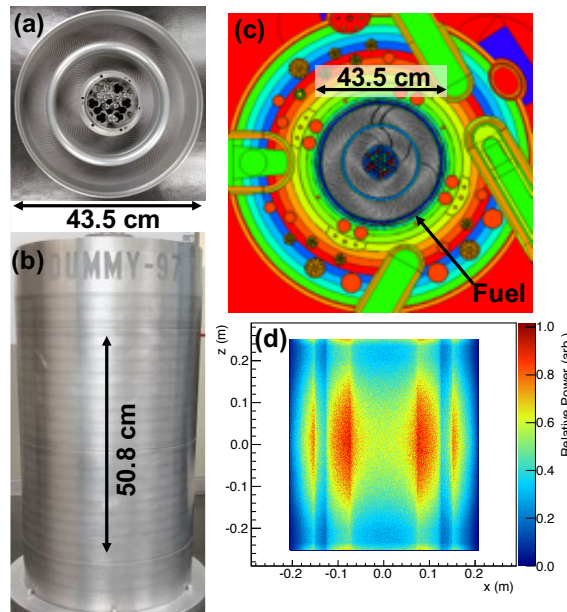


Figure 3.1. A model of the reactor [76] parameters. (a) and (b) are the diameter and height of the HFIR core. The location of the HFIR core in a detailed reactor system simulation is indicated in (c). (d) is a projection of the fission power density of HFIR at the x-z plane.

maintain its high  $^{235}\text{U}$  enrichment, the HFIR reactor is operated in relatively short reactor cycles. In this case, the fuel evolution of fissile isotopes is negligible.

The HFIR facility also brings unique background challenges for neutrino mea-

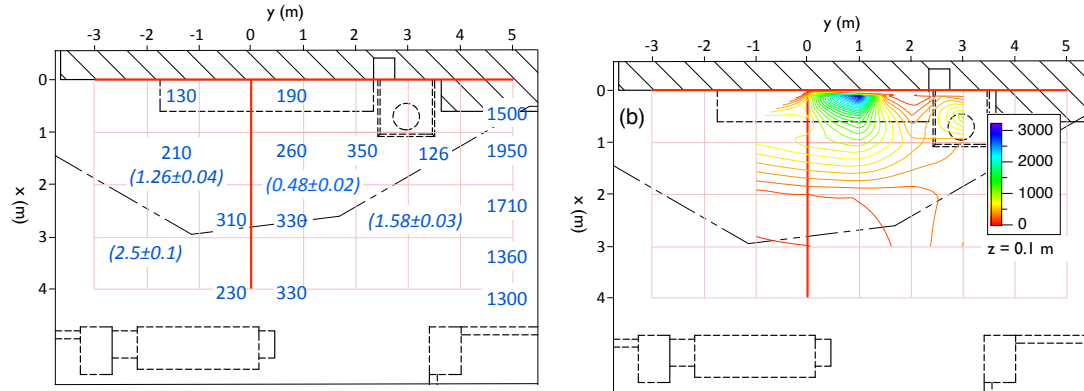


Figure 3.2. (Left) The reactor correlated neutron background rate (nSv/h) shown in a map of the HFIR site where PROSPECT is deployed. (Right) The local  $\gamma$  ray background rate (Hz) shown in the same map.

measurements. Due to availability of an experiment site at very short baseline, the PROSPECT AD is exposed to cosmic ray backgrounds with minimal overburden. The detector also faces reactor correlated background, e.g., the background neutrons generated from the reactor, and the gamma-ray background from neutron capture on materials in the piping of the facility. A comprehensive background characterization was therefore organized in the research and development (R&D) phase of PROSPECT [78]. Figure 3.2 shows the amplitude of the gamma and neutron background. The detector and additional background shielding were designed based on this background survey.

### 3.2 Detector Design

The PROSPECT AD is a  $\sim 4$  ton  ${}^6\text{Li}$ -doped LS ( ${}^6\text{LiLS}$ ) detector deployed at 7-9 m baselines from the HFIR core. The critical parameters of the PROSPECT AD are shown in Table 3.2. The schematic of detector deployment at the HFIR facility is shown in Figure 3.3.

The anatomy of the PROSPECT AD is shown in Figure 3.4. The inner volume of the detector is contained in a liquid-tight acrylic tank filled with the  ${}^6\text{LiLS}$ ,

Table 3.2. The key parameters of the PROSPECT AD [76].

Parameter	Value
Target volume & mass	3760 liters, 3.68 tons
Target dimension	1.176 m wide $\times$ 2.045 m long $\times$ 1.607 m tall
Baseline	7.9 m
Liquid scintillator	EJ-309 based LS with $<0.1\%$ $^6\text{Li}$
LS energy resolution	4.5%
Segments	14 horizontal <i>times</i> 11 vertical
Segment dimension	1.176 m wide $\times$ 14.5 cm long $\times$ 14.5 cm tall
Light collection	diameter = 12.7 cm (5 inch) PMTs
Position resolution	$\sigma_X = 14.5$ cm, $\sigma_Y = 14.5$ cm, $\sigma_Z \approx 5$ cm

which is made from EJ-309 base, an organic LS [79]. The acrylic tank is shielded by layers of water, polyethylene, lead, and borated polyethylene, respectively from the outside to inside to suppress neutron and gamma backgrounds. The designed energy resolution is 4.5% to optimize PROSPECT's IBD spectrum measurement. An advantage of utilizing EJ-309 is its pulse shape discrimination (PSD) capability which makes the PROSPECT AD sensitive to particle identity, which is described in detail in Section 3.3. The purified  $^6\text{Li}$  is loaded as a main neutron capture isotope through dissolved LiCl in the scintillator. A small amount of  $^{227}\text{Ac}$  was also uniformly spiked in the LS for active calibration of segment volume differences.

The inner volume of the PROSPECT AD is optically segmented by a lightweight optical grid subsystem [80]. The optical grid consists of highly reflective

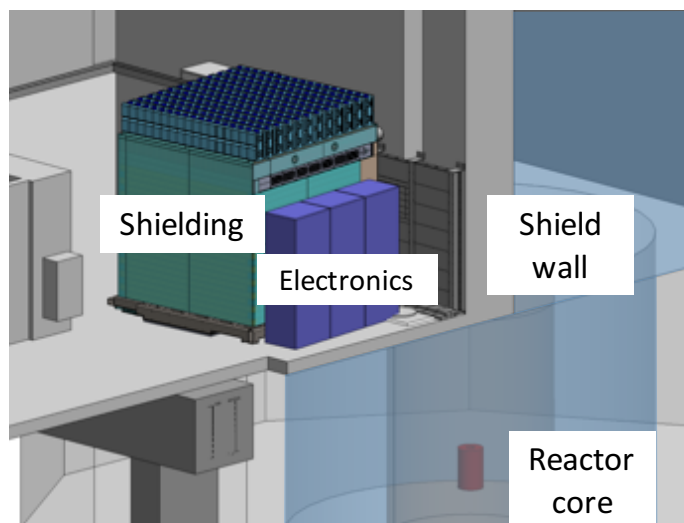


Figure 3.3. The layout of the PROSPECT experiment. The PROSPECT AD is deployed 7.9 m from the reactor center to the detector center. An additional on-site lead shield was installed between the reactor pool and the AD to eliminate local gamma-ray backgrounds.

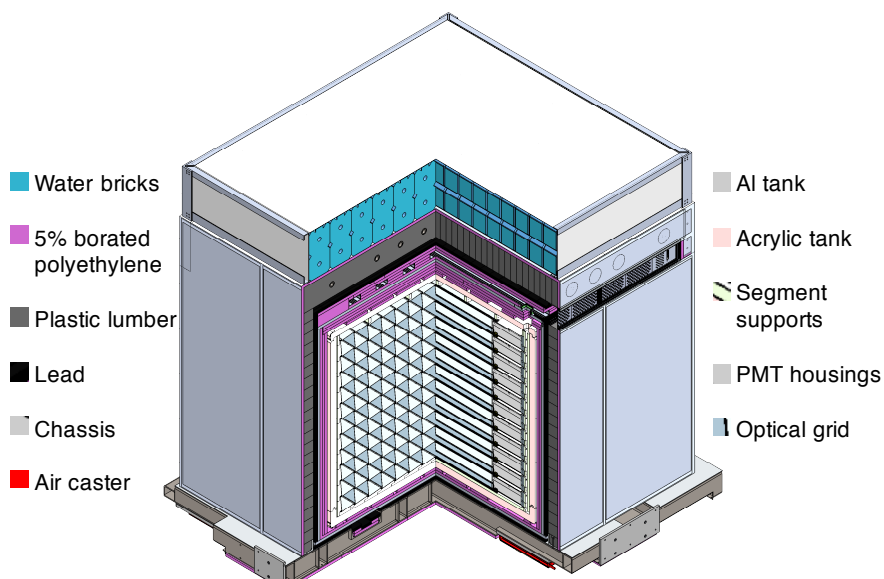


Figure 3.4. The design of the PROSPECT AD, consisting an inner volume and surrounding layers of shielding. The inner detector includes  ${}^6\text{LiLS}$ , the optical grid, PMTs, and the calibration system.

carbon fiber backed separators dividing the LS volume into  $14 \times 11$  identical longitudinal segments. Each segment is enclosed by two 12.7 cm diameter PMTs at its two ends. Schematics of the PROSPECT AD inner volume are shown in Figure 3.5. The segment with the largest LS light signal is identified as the interaction point (x- and y-direction) of an incident particle. The readout of PMTs, which are housed in mineral-oil filled acrylic modules (PMT optical modules) on both sides of each segment, allows for timing- and charge-based position reconstruction along the axis (z-direction) of each segment [81, 82]. Hence, the optical grid makes the PROSPECT AD able to reconstruct incident particles' 3D positions, which is an essential function for cosmic ray rejection and oscillation measurements.

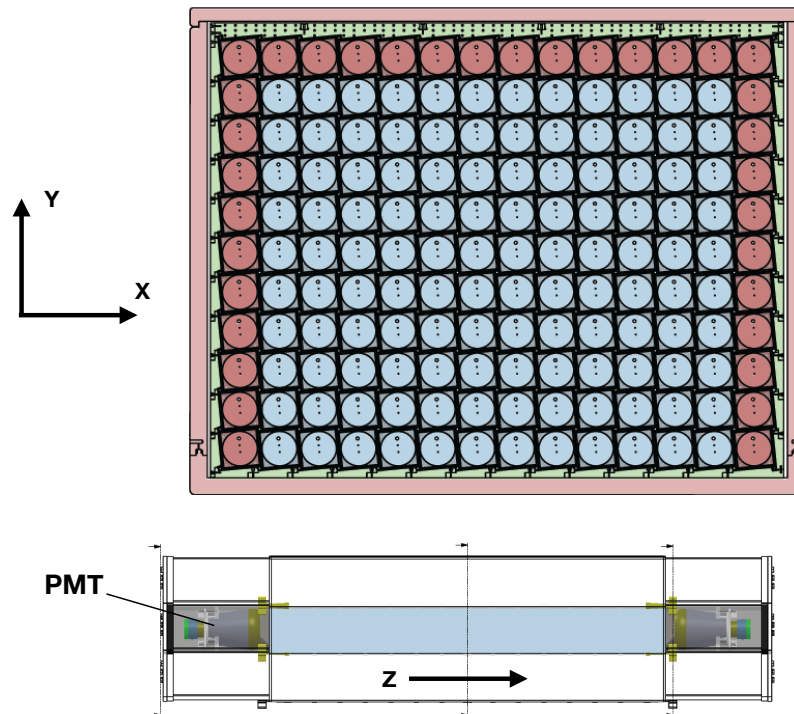


Figure 3.5. Schematic of the inner volume of the PROSPECT AD. (Top) A side view to the X,Y plane of the AD, the red grids represent segments assembled with Electron Tubes PMTs and the light blue grids represent segments with Hamamatsu PMTs. (Bottom) A schematic of a single segment.

### 3.3 Antineutrino Detection

**3.3.1 IBD signature.** Similar to other reactor neutrino experiments, the PROSPECT AD detects  $\bar{\nu}_e$  through the detection of the positron and neutron produced in the IBD process:

$$\bar{\nu}_e + p \rightarrow n + e^+. \quad (3.1)$$

The positron deposits its kinetic energy immediately in the LS by transferring the kinetic energy to molecular energy that generates scintillation light, a process described in detail in Chapter 5. Having lost most of its kinetic energy, positron-electron annihilation produces two 511 keV gammas moving in opposite directions. The IBD neutron produced, with keV-scale kinetic energy, is decelerated within 50  $\mu\text{s}$  and then captured by a nucleus in the LS. The main neutron capturing isotope in the PROSPECT AD is  ${}^6\text{Li}$ , with approximately 80% of the total neutron capture fraction. The  $n$ -Li capture process,

$$n + {}^6\text{Li} \rightarrow \alpha + {}^3\text{H}, \quad (3.2)$$

brings an advantage for PROSPECT that the event signature includes only the recoil of  $\alpha$  and  ${}^3\text{H}$  nuclei without energy loss. The traveling distance of  $\alpha$  and  ${}^3\text{H}$  produced are in the mm-scale. Thus, the  $n$ -Li capture event is restricted to a single segment. On the contrary, most of the historical reactor neutrino experiments utilizing Gd as the neutron capture solvent have to tag the neutron signal as a cascade of  $\gamma$  rays with a total energy of approximately 8 MeV and a spreading light signal at the meter-scale. The scintillation signal of the IBD produced positron, and its annihilation gammas are detected at the 10 ns scale after the IBD process, followed by the  $\sim 50$   $\mu\text{s}$  delayed neutron capture signal. Hence, the positron and neutron signals are referred to as prompt and delayed signals, respectively. A schematic of the IBD signals in PROSPECT is shown in Figure 3.6.

**3.3.2 Prompt and Delayed Signal Discrimination.** PROSPECT discriminates

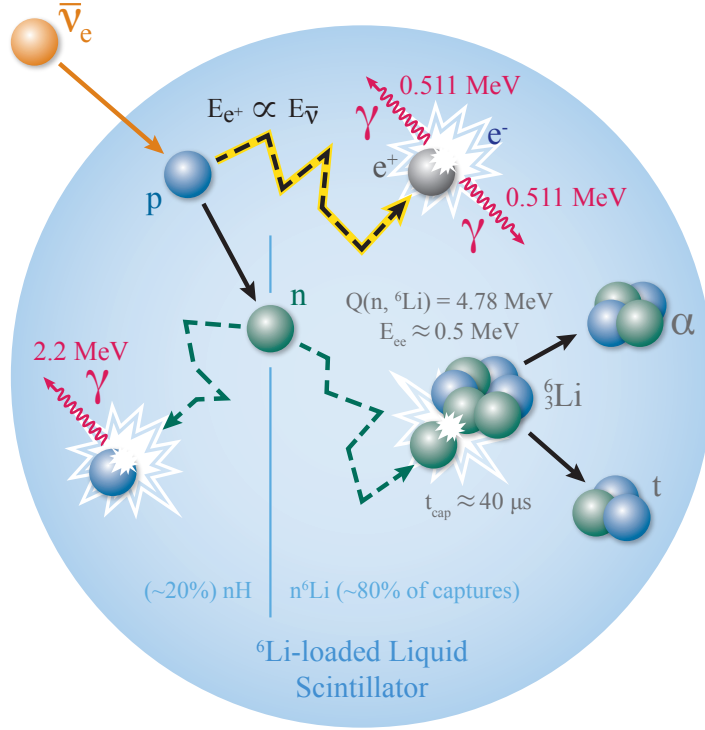


Figure 3.6. A schematic of IBD detection in PROSPECT AD. An IBD event is tagged with time coincidence between the positron and the neutron events. The positron deposits its energy and annihilates in  $\sim 10$  ns after IBD process. Within  $\sim 50$   $\mu$ s after the IBD process, the neutron is mainly captured by  ${}^6\text{Li}$ , generating  $\alpha$  and tritium with a total kinetic energy of 4.78 MeV (0.55 MeV electron equivalent).

the prompt and delayed signal with PSD. The pulse shape of scintillation light in EJ-309 contains short-lived and long-lived fluorescence components whose fractions in the light pulse are dependent on the  $dE/dx$  of an ionizing particle. Since the  $dE/dx$  of charged nuclei is greater than the positrons and electrons, a significant difference of pulse shapes between the prompt and the delayed signals is shown as Figure 3.7. For the ease of signal discrimination, a PSD parameter is defined as the tail fraction of the pulse integral,

$$\text{PSD} = \frac{Q_{\text{tail}}}{Q_{\text{full}}}. \quad (3.3)$$

The time window of the tail integral, illustrated in Figure 3.7, is user defined to maximize the gamma-neutron discrimination [82]. With event selection based on the

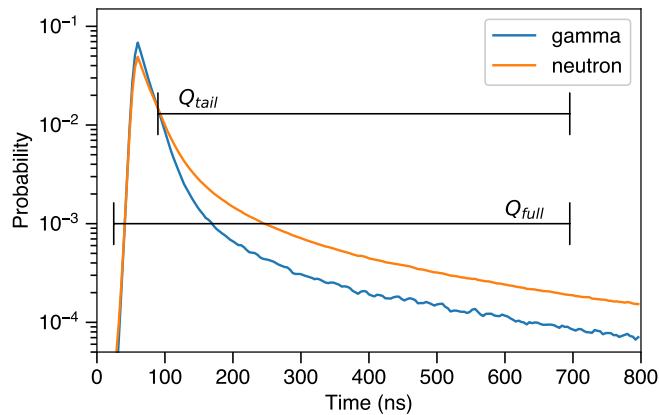


Figure 3.7. An example of the different pulse shape between a  $\gamma$  ray-like signal and a neutron-like signal [81].

reconstructed energy, timing and PSD value of a pulse, clear signal types can be distinguished as shown in Figure 3.8.

**3.3.3 Energy and Position Reconstruction.** The segmented nature of the PROSPECT AD allows particles with enough energy to travel through multiple segments. The energy of particles deposited in each segment is reconstructed by counting scintillation light collected by the PMTs on its ends. When both PMTs of a segment are triggered coincidentally, this light signal is referred to as a *hit*. An event *cluster* is defined as a group of hits in a 20 ns time interval. The reconstructed energy of a particle is the sum of energy deposited in all segments of a cluster, as illustrated in Figure 3.9. The reconstructed event vertex  $(x, y)$  position is defined as the location of the segment with the largest energy deposition in a cluster.

An event vertex's  $z$  position is reconstructed based on the charge and timing difference between the pair of PMTs' light signals. The schematic of a single segment's light collection is shown in Figure 3.10. Because of the light attenuation in the LS, the light collection by a PMT at one end decreases exponentially with increasing distance from that PMT to the vertex, resulting in the segment's total light collection non-

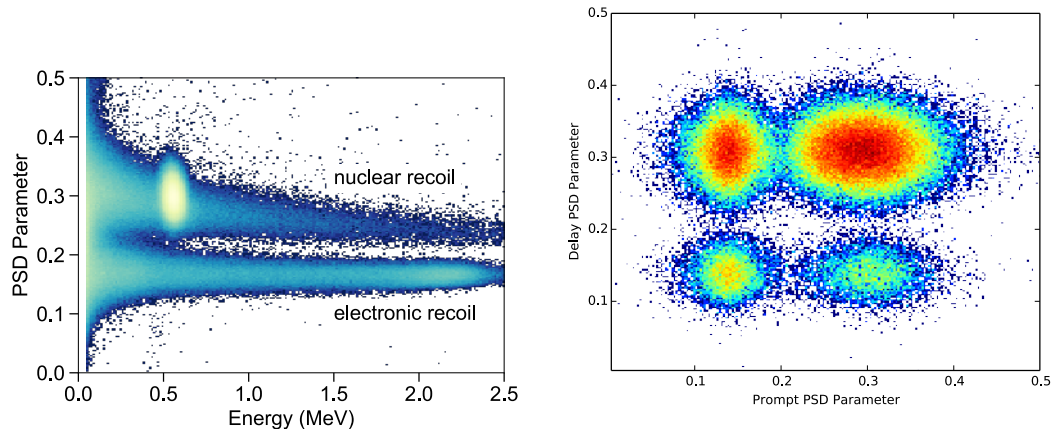


Figure 3.8. The IBD event selection based on PSD [81]. (Left) The distribution of  $^{252}\text{Cf}$  neutron and gamma events in an energy and PSD parameter space. A well-constrained distribution of  $n$ -Li capture can be seen at the low energy high PSD spot. (Right) The distribution of prompt-delay pair event in the PSD and time coincidence parameter space, where the top-left spot is the distribution of IBD candidates.

uniformity along the  $z$  direction. The detection timing difference between the PMTs is also dependent on the  $z$  position, making it a useful tool in  $z$  position reconstruction. Further discussion about the  $z$  position calibration and reconstruction is detailed in Chapter 6.

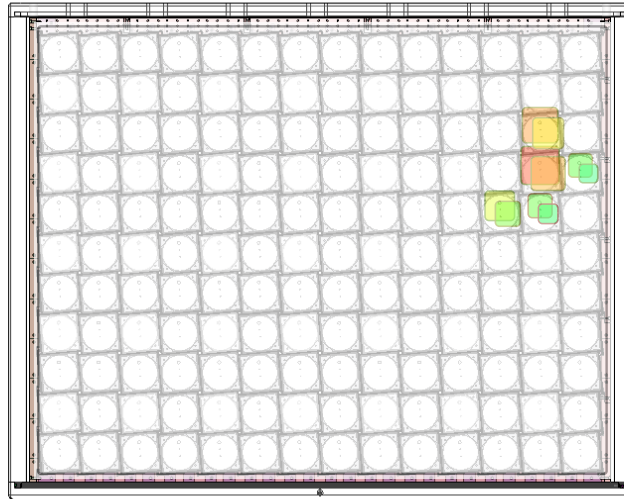


Figure 3.9. An illustration of an event cluster. The colored segments are segments which collected scintillation light within the cluster's time window. The reconstructed energy of this event is the summed energy detected by each segment hit in this cluster. The size and color of each colored box are correlated to the light collected in each PMT. The reconstructed positron is in the segment with the most significant light collection.

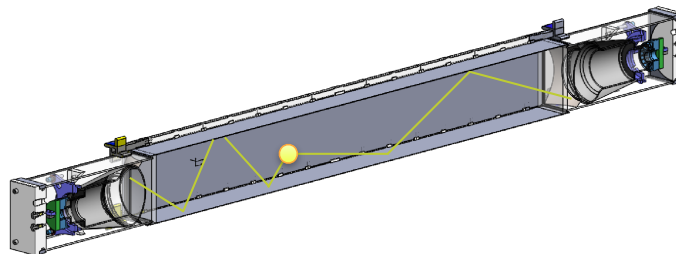


Figure 3.10. An illustration of the light collection within one segment. When scintillation light is generated from an incident particle, the light is constrained in the segment by the specular reflective separators. The two PMTs on the ends of a segment detect different light and at a different time with respect to the vertex location.

## CHAPTER 4

### DETECTOR RESEARCH, DEVELOPMENT, CONSTRUCTION, AND COMMISSIONING

Research and development for the PROSPECT AD began in 2014. The timeline of PROSPECT R&D is shown in Table [4.1](#). With the goals of maximizing the  ${}^6\text{LiLS}$  performance and background subtraction, as well as minimizing the dead volume and liquid degradation, the detector design was tested and demonstrated by multiple prototype detectors.

After two years of R&D, the fabrication of the detector components and the  ${}^6\text{LiLS}$  were organized in different facilities that mainly included the Illinois Institute of Technology (IIT), Yale University (Yale), and Brookhaven National Laboratory (BNL). Comprehensive quality control (QC) and quality assurance (QA) were included in fabrication procedures to ensure detector performance, especially detector stability and segment uniformity.

During the detector R&D, I co-led the efforts of design, fabrication, QC and QA of the optical grid components. I also took significant role in the assembly of the PMT modules, the detector inner volume, as well as the detector commissioning at the HFIR facility.

This chapter briefly describes the prototype detectors of PROSPECT, and details the design and fabrication of the detector components. Descriptions of detector assembly and commissioning are also included.

Table 4.1. PROSPECT R&D and construction phases.

Phase	Time	Goal	Location	Reference
0.1 liter prototype	Aug. 2014	DAQ, LS performance	Yale University	
2 liter prototype	Dec. 2014 to Mar. 2015	Background survey, shielding	HFIR	[78]
20 liter prototype	Mar. 2015 to Aug. 2016	Single segment performance	HFIR and Yale	[82]
50 liter prototype	Jan. 2016 to Mar. 2019	Two-segment event reconstruction, detector stability	Yale University	[81]
Optical grid component fabrication	Nov. 2016 to Sept. 2017	Component fabrication and optical measurements	IIT	[80]
LS fabrication	Jan. 2017 to Oct. 2017	LS production, $^6\text{Li}$ loading, $^{227}\text{Ac}$ loading	BNL	[79]
PMT module assembly	Sept. 2016 to Oct. 2017	PMT delivery, test, module assembly	Yale	
Detector assembly	Oct. 2017 to Dec. 2017	Detector assembly, electronic initial test	Yale	[76, 80]
Detector commissioning	Dec. 2017 to Mar. 2019	LS filling, shielding assembly, calibration system assembly, detector initial commissioning	HFIR	
Data acquisition	since Mar. 2018	Data acquisition	HFIR	[81]

## 4.1 Prototype Research

In early R&D phases, prototype detectors were assembled to develop and demonstrate a variety of designed detector features. During this phase, many candidate materials were tested. The first PROSPECT prototype detector was built with a cylindrical test cell filled with 0.1 liter  ${}^6\text{LiLS}$ . This prototype demonstrated the  $n$ -Li capture and PSD features of the  ${}^6\text{LiLS}$ .

From December 2014 to March 2015, a 2-liter prototype detector (PROSPECT-2) was deployed at the designed detector location in the HFIR facility building with a primary purpose of performing an on-site background survey. As shown in Figure 4.1, this prototype was a single volume cylindrical detector surrounded by specular reflectors with two PMTs on its ends. By comparing the reactor-on and -off gamma and neutron detection rate, this prototype demonstrated a shielding strategy that could effectively eliminate reactor correlated gamma and  $n$ -Li capture events [78].

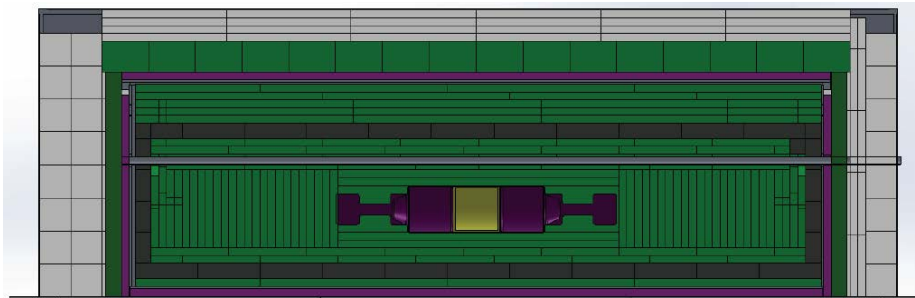


Figure 4.1. PROSPECT-2 prototype installed at HFIR. The 5” cylindrical LS detector (yellow), PMTs and HV bases (purple) are surrounded by 5% borated polyethylene sheets (green), lead (dark grey), more 5% borated polyethylene sheet, an Al containment box (grey), 30% borated polyethylene sheet (purple), more 5% borated polyethylene sheet, and polyethylene sheet (light grey).

Two 23-liter prototypes (PROSPECT-20) [82] were deployed at HFIR and Yale, respectively. The goals of these two prototypes were to further characterize background, as well as study the scintillator performance and stability [82]. Figure 4.2 shows the design of the PROSPECT-20 detector. The dimensions of PROSPECT-20

prototype were similar to a single segment of the full PROSPECT AD. PROSPECT-20 demonstrated the PSD performance, energy reconstruction, and position reconstruction with respect to gamma calibration sources deployed along with the detector. Several candidate designs and materials for the PMT module were also tested in these prototype studies. For instance, PROSPECT-20 first included and tested the utilization of specular reflectors and two-PMT readout to optimize the PSD performance and light collection of the detector.

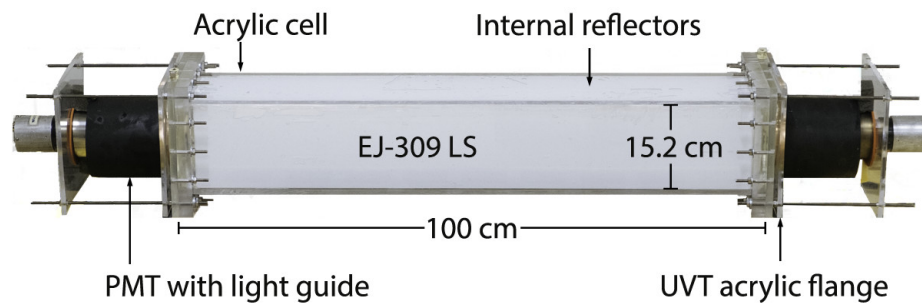


Figure 4.2. The schematic of the 23-liter prototype with labeled key components [82].

A prototype containing 50 liters of  ${}^6\text{LiLS}$  (PROSPECT-50) [81] was assembled and tested at Yale to validate the product components for the final PROSPECT AD. Figure 4.3 shows the schematic of this prototype. The PROSPECT-50 detector consisted of two segments whose dimensions are identical to the designed dimensions of the segments of the finalized detector. The chemical compatibility of detector components, including PMT modules, optical grid, calibration system, and cables, were tested in direct contact with  ${}^6\text{LiLS}$ . PROSPECT-50 also provides a parallel light yield stability monitor for the PROSPECT AD. Cosmogenic background, gamma, and neutron calibrations were measured with this 50 liter prototype. These measurements led to the development of analysis packages for segment-based event reconstruction and validated the detector simulation through data to Monte-Carlo comparisons.

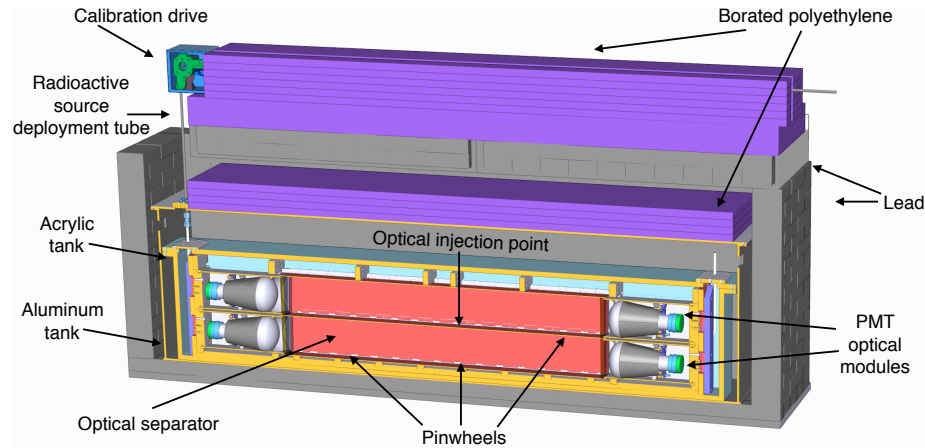


Figure 4.3. A schematic of the PROSPECT-50 prototype with labeled key components [81].

## 4.2 ${}^6\text{Li}$ Loaded Liquid Scintillator

${}^6\text{LiLS}$  is the target material of the PROSPECT AD. The base scintillator, EJ-309, is a di-isopropyl naphthalene based liquid organic scintillator with 2,5-diphenyloxazole and 1,4-bis(2-methylstyryl) benzene dissolved as the wavelength shifter to cover the wavelength range of the PMT light collection in PROSPECT. The  ${}^6\text{Li}$  isotope was loaded with the LiCl solution that dissolved in the base scintillator with an aqueous surfactant. The  ${}^6\text{LiCl}$  solution was fabricated in the National Institute of Standards and Technology using enriched lithium carbonate ( $95\pm 1\%$   ${}^6\text{Li}$  by atom). EJ-309 contains  $5.43 \times 10^{22}/\text{cm}^3$  H atoms, making  $n$ -H capture the second most abundant neutron capture interaction in the PROSPECT AD. The  ${}^6\text{LiLS}$  was also uniformly spiked with  $1.8 \text{ Bq } {}^{227}\text{Ac}$ . The two  $\alpha$  decays initiated by  ${}^{227}\text{Ac}$  can be used to passively characterize position reconstruction resolution and the relative volume difference among segments.

The PROSPECT-50 prototype was used to show that the solution of oxygen in the  ${}^6\text{LiLS}$  can cause oxygen quenching and reduce the light yield after the scintillator was exposed to air. Covering and dissolving the scintillator with nitrogen is necessary

to prevent oxygen quenching during  ${}^6\text{LiLS}$  production and detector operation.

QA measurements of the produced  ${}^6\text{LiLS}$  are shown in Figure 4.4. Relative light absorbance ( $1\sigma = 0.3\%$ ) is observed between each batch in the wavelength range of interest. A relative light yield comparison between  ${}^6\text{LiLS}$  and LAB (a commonly used liquid scintillator) was made for each batch of production to ensure consistent light yield throughout the fabrication. The figure-of-merit of pulse shape discrimination (FoM, a parameter defined to quantify the neutron and electron separation in PSD),

$$FoM = (\overline{PSD}_n - \overline{PSD}_e) / \sqrt{FWHM_n^2 + FWHM_e^2}, \quad (4.1)$$

was evaluated throughout the production for each batch of produced  ${}^6\text{LiLS}$ . The designed energy resolution of the  ${}^6\text{LiLS}$  is  $4.5\% / \sqrt{E(\text{MeV})}$ , which was demonstrated by the PROSPECT-50 prototype [81].

### 4.3 Optical Grid

The neutrino oscillation measurement in PROSPECT needs a position-sensitive IBD detector. Because the available site for PROSPECT AD deployment has less than one meter water equivalent (m.w.e) overburden, the PROSPECT AD should also be designed as a particle track sensitive detector to identify cosmogenic backgrounds. The optical grid subsystem is thus a vital structure for both of PROSPECT's primary neutrino physics goals. This subsystem is designed to meet the goals of:

- Minimizing the inactive volume and mass;
- Maximizing the light collection efficiency with high reflectivity;
- Minimizing the cross-segment light transmission;
- Ensuring material compatibility with  ${}^6\text{LiLS}$ ;
- Enabling the calibration system's installation in the detector volume.

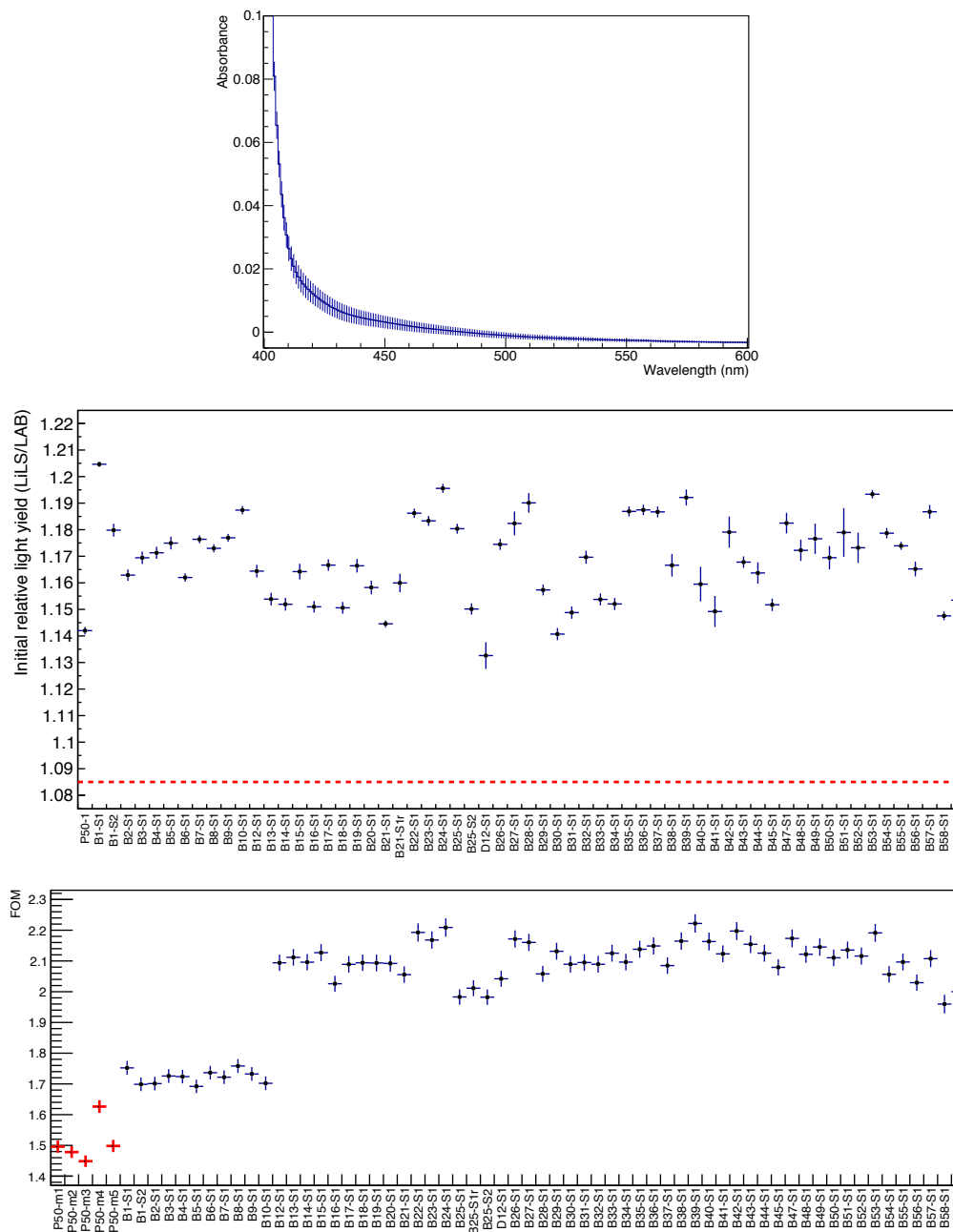


Figure 4.4. (Top) The average of the relative absorbance of all the measured LiLS samples. (Center) The relative light yield ratio between  ${}^6\text{LiLS}$  and LAB. (Bottom) The FOM evaluated from each batch of product  ${}^6\text{LiLS}$ . [79]

The major components of the optical grid were designed and fabricated at IIT. I played key roles in the material searching, fabrication, QC and QA tests, and construction of this subsystem. An article was published by the IIT group of PROSPECT,

see Reference [80].

**4.3.1 Optical Grid Design.** The structure of the optical grid is shown in Figure 4.5. This subsystem consists of specular reflective separators and 3D printed polylactic acid (PLA) rods. The separators and PLA rods interlock each other to assemble a stable  $14 \times 11$  grid structure, whose dimensions can be found in Table 3.2. The interlocking pieces enforce a  $\sim 5^\circ$  tilted angle for each segment. The segments of the optical grid are enclosed by 154 PMT modules on each end, forming the inner detector structure which is supported by external acrylic supports.

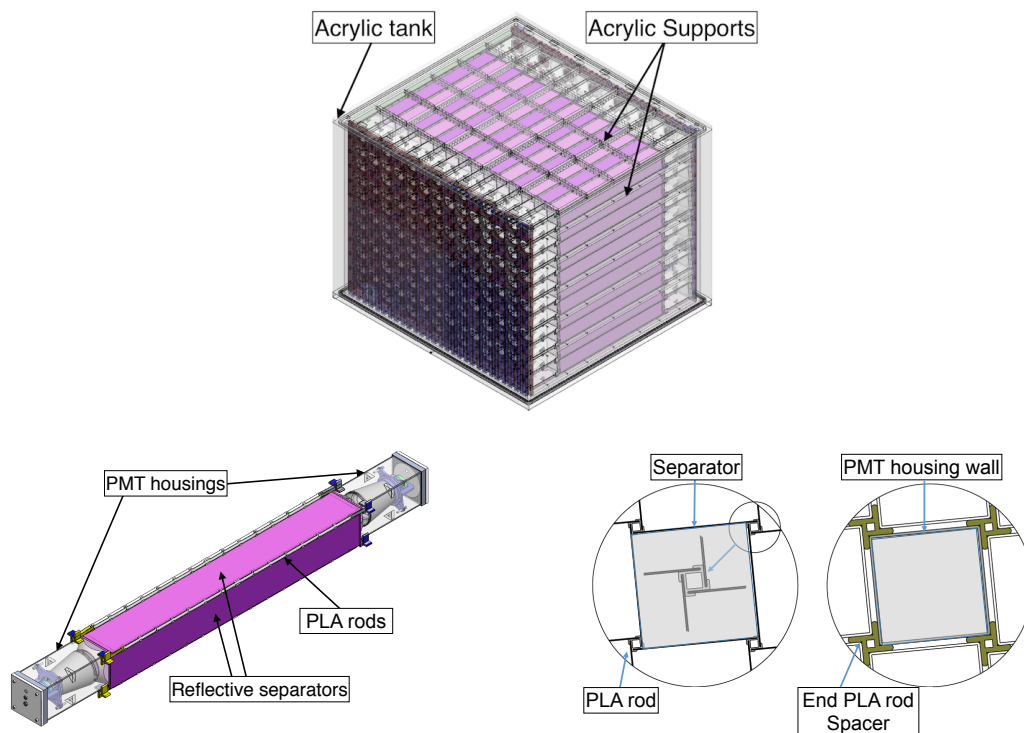


Figure 4.5. Detailed PROSPECT optical grid schematic. (Top) The active detector enclosed by liquid-tight sealed acrylic tank. (Bottom left) The individual segment with a 12.7 cm (5 in) diameter PMT on each end and enclosed by 4 reflective separators. (Bottom right) The cross section view of the PLA rods and segment, where the separators are slotted on the PLA rods and the PLA rods are hollow to allow calibration sources to be inserted.

**4.3.2 Separators.** The separators are composed of a laminated sandwich of a carbon fiber backbone, reflector layers, adhesive layers, and 0.05 mm-thick protective

Fluorinated Ethylene Propylene (FEP) films, as shown in Figure 4.6. Except for the FEP film, poor compatibility between the separator materials and the  ${}^6\text{LiLS}$  was found in chemical compatibility tests. In order to prevent direct contact between the  ${}^6\text{LiLS}$  and the incompatible materials, the FEP protective films were heat-sealed and folded, as illustrated in Figure 4.6 (right).

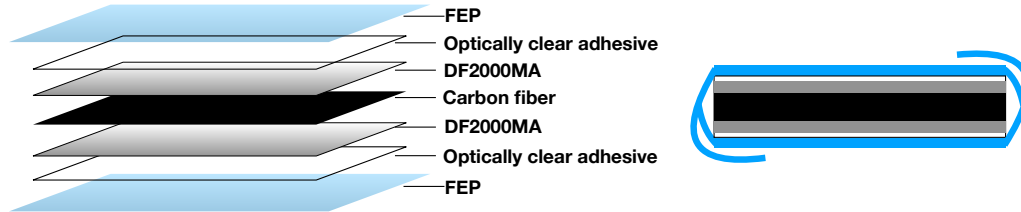


Figure 4.6. (Left) Illustration of the sandwich structure of a separator. (Right) Illustration of the separator with the overhung FEP folded.

Table 4.2 lists designed and measured optical grid component dimensions. The total length of the separators, excluding the heat-sealed overhanging FEP, was designed to be  $120.65 \text{ cm} \pm 0.25 \text{ cm}$  ( $47.5 \text{ in} \pm 0.1 \text{ in}$ ). The designed distance between the front surfaces of the two PMT housings is  $117.4 \text{ cm}$  ( $46.25 \text{ in}$ ), with the reflecting separator surface extending beyond the front windows of the PMT housings and out of the active optical volume of the segment. Since the separators extend past the faces of the PMT housings, the tolerances on the separator length are not stringent. Based on the PMT housing dimensions and extra width needed for securely coupling to the PLA rods, the nominal width of separators was designed to be  $15.35 \text{ cm} \pm 0.04 \text{ cm}$ . The summed thickness of all laminated material is  $1.03 \text{ mm} \pm 0.1 \text{ mm}$ . Accounting for the allowed thickness of the assembly with the PLA rods and the imperfect coupling between each two-layers, the allowed and measured thickness is higher than the summed thickness of all individual layers.

The reflective material used is DF2000MA, an adhesive-backed organic re-

Table 4.2. Designed and measured dimensional parameters of separators.

Material	Dimensions and tolerance (mm)
Nominal length	$1206.5 \pm 2.5$
Nominal width	$153.5 \pm 0.4$
Nominal thickness (sum of material thickness)	$1.03 \pm 0.1$
Allowed thickness for assembly	1.119-1.124
Measured width	$153.6 \pm 0.6$
Measured thickness	$1.18 \pm 0.05$

flecting film. DF2000MA is made of multiple polymer layers with varying refractive indices, which produce multiple total internal reflections [83]. Among the tested materials in PROSPECT R&D, DF2000MA exhibits superior specular reflectance in the range of wavelength from 400 nm to 550 nm, as shown in Figure 4.7. The FEP film was laminated on top of the DF2000MA with optically clear adhesives. Having a substantially lower index of refraction than the  ${}^6\text{LiLS}$  ( $\sim 1.3$  versus  $\sim 1.55$ , respectively), the FEP film also ensures total internal reflection of grazing angle incident scintillation light back into the  ${}^6\text{LiLS}$  bulk.

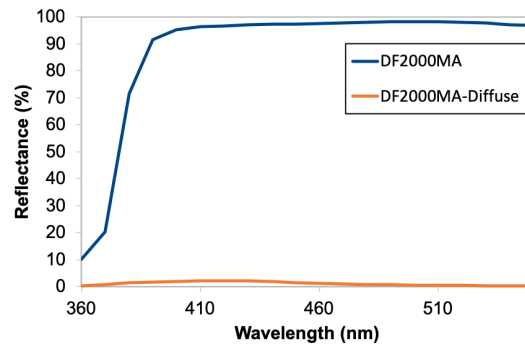


Figure 4.7. Total reflectance and diffuse reflectance of DF2000MA.

The lamination of all separators was conducted in a class 10000 clean tent at IIT. Each layer of different material was laminated at room temperature with a silicon roll laminator. Because the puncture of FEP film can cause exposure of inner separator materials to the  ${}^6\text{LiLS}$ , the lamination procedures were designed to minimize the possibility of causing scratches on separator surfaces or leaving dust between layers. Photographs of the lamination process and a laminated separator are shown in Figure 4.8. In the end, each separator was labeled with stickers on the excess of FEP film for QC and QA purposes, then shipped to a company specializing in heat sealing FEP films.

The QA measurements of the separators includes surface quality evaluation, dimension measurements, reflectance measurements, and sealing tests. Separators with wrinkles or dust whose diameter is greater than 1 mm were rejected. A separator with width or thickness out of tolerance were also rejected. The total reflectance and diffuse reflectance of the separators was measured with a compact spectrometer in the fabrication cleanroom. By measuring relative total reflectance compared to a small size separator sample, separators with visible optical defects were rejected. Sealing tests were conducted twice, first after FEP heat sealing and then during final cleaning. It was found during R&D that the adhesive turns white in air when it is contacted with ethyl alcohol. Therefore, ethyl alcohol was applied on the separator surface to identify a puncture or failed sealing. Separators passing the sealing tests were accepted for detector assembly. The count of laminated separators that passed each level of QC is shown in Table 4.3.

**4.3.3 3D Printed PLA Rod.** The PLA rods were designed to support the separators with low density and low volume material, while contributing a precise interface between separators and other detector supporting structures. In addition, the PLA rods provide enough free space for optical and radioactive calibration structures to

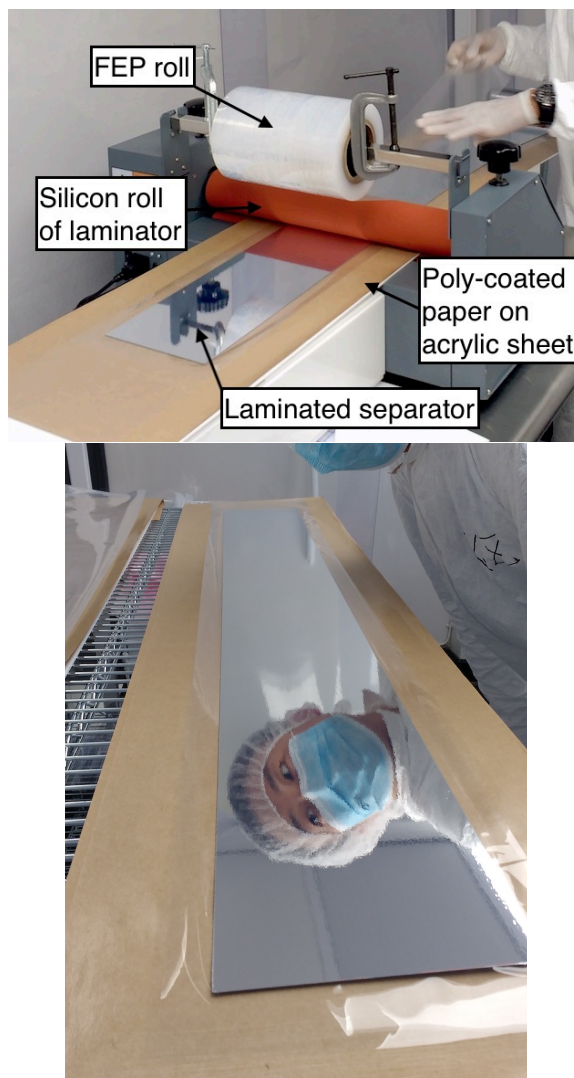


Figure 4.8. (Top) Photograph of lamination setup, when FEP film were being laminated on one side of separator. (Bottom) Photograph of a laminated separator.

feed through into the detector inner volume. Fused Deposition Modeling (FDM) 3D printing was deemed to be the best choice for the production of the PLA rods. This method of 3D printing has advantages of its ability to produce complicated geometries, a wide choice of materials, ease of prototyping, and minimal setup cost. Among the tested materials for 3D printing, PLA was found compatible to  ${}^6\text{LiLS}$ . Using white-dyed PLA, PROSPECT also takes advantage of its high diffuse reflectivity and low light transmission, as shown in Figure [4.9](#).

Table 4.3. The count of laminated separators that passed each level of QC. 98.6% (367 out of 372) of laminated separators passed QC; 333 separators were assembled into the PROSPECT AD.

QC level	Count of separators
Laminated	372
Surface quality	371
Optical QA	370
Dimensional QA	369
Heat sealing quality	367
Used in detector assembly	333

The PLA rods are longitudinal tubes with a square cross-section. There are small tabs printed on the outer surface for interlocking with the separators, forming a pinwheel-shaped cross-section. Because of the part failure rate and the limited size of available 3D printers, all PLA rods are no more than 15.69 cm in length. There are nine types of PLA rods designed according to their location in the assembled detector, as shown in Figure 4.10. These nine types can be categorized into three main categories listed below.

- Standard PLA rods: A 15.69 cm long rod with the tabs at its center and each end to allow the insertion of separators. The tabs on the ends are  $\sim 6$  mm long, and the tab at the center is  $\sim 13$  mm long to balance the structural stability and reflector exposure. Among the standard PLA rods, there are PLA rods slightly longer to accurately fit the length of each segment and ensure light-tight closure between segments. These standard PLA rods are labeled as type-1 and type-9, respectively. There are 720 (360) type-1 (type-9) PLA rods needed in the

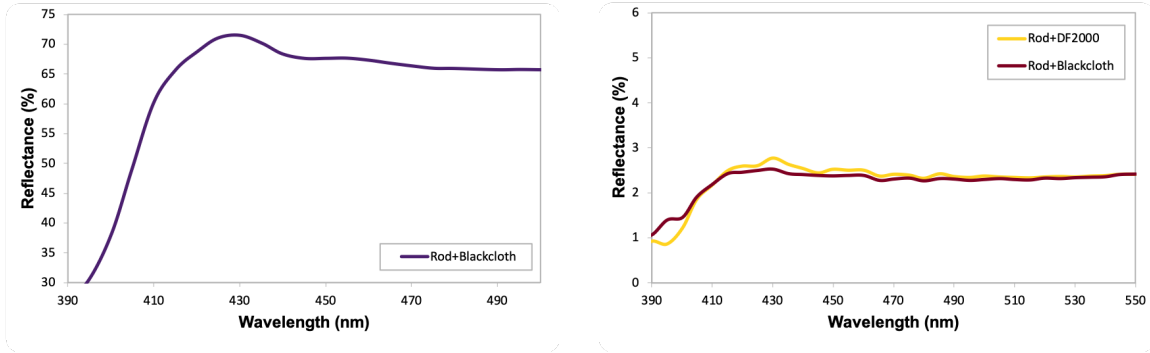


Figure 4.9. (Left) Absolute diffuse reflectance of PLA rods. (Right) Total reflectance of PLA rods relative to bare DF2000MA. When PLA was backed by DF2000MA reflector, the reflectance can be compared against the measurement of PLA backed by a black cloth to indicate the transmission of light.

#### PROSPECT AD.

- Center PLA rods: Similar to the standard PLA rod but with a 2.54 cm (1 in) wide center tab that allows further machining for the insertion of optical calibration system components. The center PLA rods are labeled as type-2. There are 180 type-2 PLA rods needed in the PROSPECT AD.
- End PLA rods: A 9.53 cm long rod whose one end is a standard tab for the separator to insert and whose other end is a pinwheel-shaped, thick, rigid spacer to maintain set spacings between PMT modules and strung PLA rods. The number of arms on the spacers depends on the location of rods in the detector. The end PLA rods are labeled as type-3 to type-8. There are 360 end PLA rods needed in the PROSPECT AD.

There are 1620 PLA rods of different types needed for PROSPECT. The PLA rods are 3D printed by a company specialized in commercial 3D printing with multiple 3D printers to parallel print all PLA rods. According to the manufacturer, the PLA rods were printed with 100  $\mu\text{m}$  PLA filament.

Temperature instability during 3D printing can cause burnt spots on the PLA

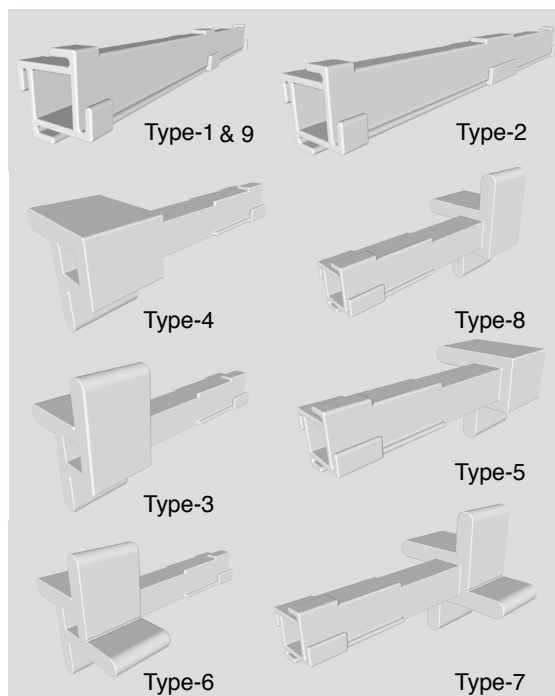


Figure 4.10. Schematic of PLA rods labeled by type.

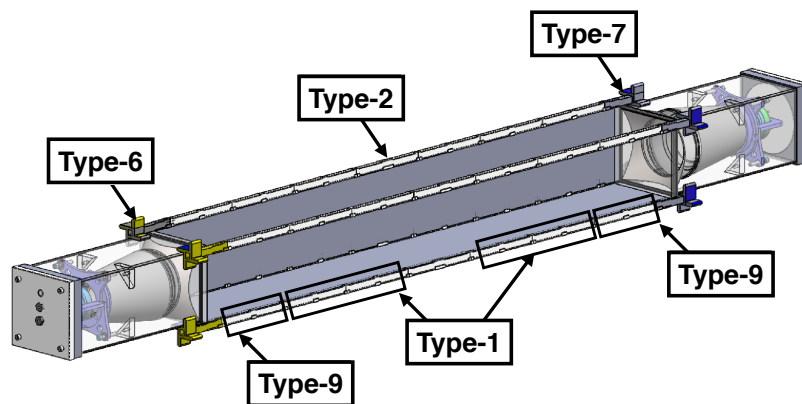


Figure 4.11. The assembled locations of different types of PLA rods. In this figure, the end PLA rods are type-6 and -7. If a segment is at a corner of the detector, the end PLA rods at the specific corner of the segment would be type-4 and -5. Similarly, if the segment is on the edge of the detect, the end PLA rods on one edge would be type-3 and -8.

surface. Because the burnt PLA's compatibility with  ${}^6\text{LiLS}$  is unknown, PLA rods with burnt spots were rejected. The surface quality of the PLA rods is evaluated

in QA, for shape imperfection can cause a puncture to the separators' FEP film. 10-20% of the PLA rods were rejected for burns, contributing the majority of the rejects. Hence, the surfaces of each PLA rods were filed with stainless steel files. The spacer volume was further filed through CNC machining to ensure precise dimensions required for accurate placement of end PLA rods between the PMT modules.

Before the assembly of the PROSPECT AD, the PLA rods were strung along a thin supporting acrylic rod, as shown in Figure 4.12. The string of PLA rods was firstly assembled with the corresponding separators, then assembled into the detector.

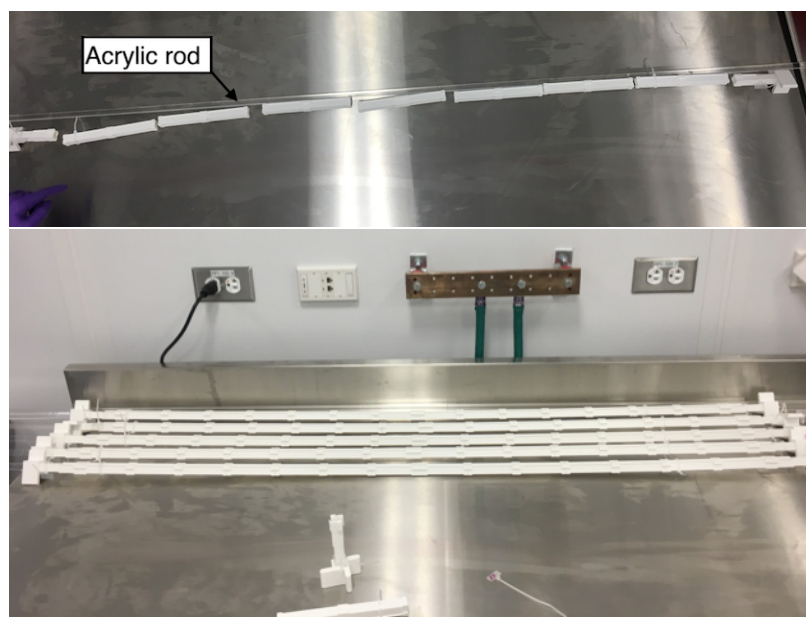


Figure 4.12. (Top) PLA rods and a acrylic rod before stringing. (Bottom) The pre-assembled long PLA rods strung on acrylic rods.

**4.3.4 Mass of the Optical Grid.** Comprehensive measurements of the optical grid components were made to quantify the key parameters that are important to validate the detector uniformity, stability, and provide quantities for PROSPECT's physics analysis. The measured properties include mass and dimensions of the components, optical reflectance, and uniformity of the components, as well as material compatibility with the  ${}^6\text{LiLS}$ .

The mass of the separators was measured in batches during the optical grid assembly (see Section 4.6). Every batch of separators assembled in the PROSPECT AD were weighed separately, and the average was calculated. The PLA rods were weighed in randomly selected groups of 20 to 50 PLA rods, and the average mass was calculated. Including the calibration system inserted into the the PLA rods, the total mass of the optical grid in the detector active volume is  $134.8 \text{ kg} \pm 1.9 \text{ kg}$  ( $158.1 \text{ kg}$  with the calibration system and supporting acrylic rods), contributing  $\sim 3\%$  ( $3.5\%$  with PTFE tube and acrylic rods) of dead mass to the PROSPECT active target region.

Table 4.4. The results of mass measurements on the separators and the PLA rods. All separators and PLA rods were weighed in batches and the quoted uncertainties reflect variation in the average component mass per batch.

Category	Average mass(g)	Total amount	Total mass(kg)
Separator	$326 \pm 10$	333	$108.7 \pm 1.7$
Standard PLA rod (type-1)	$12.3 \pm 0.1$	720	$8.86 \pm 0.07$
Center PLA rod (type-2)	$12.8 \pm 0.2$	180	$2.30 \pm 0.04$
Standard PLA rod (type-9)	$12.5 \pm 0.02$	360	$4.50 \pm 0.07$
Four arms end PLA rod (type-6&7)	$29.7 \pm 0.2$	260	$7.72 \pm 0.05$
Three arms end PLA rod (type-3&8)	$26.8 \pm 0.1$	92	$2.47 \pm 0.01$
Two arms end PLA rod (type-4&5)	$20.8 \pm 0.1$	8	0.2

#### 4.3.5 Dimensional Characterization of Optical Grid Components. Ex-

haustive dimensional measurements were done on separators. The thickness of the separators is an essential dimension due to its correlation with particle energy loss in the dead volume of the PROSPECT AD. Each separator was measured with a thickness gauge at 12 different locations on the separator. The results of the thickness measurements are shown in Figure 4.13. The average separator thickness is  $1.18 \pm 0.05$  mm.

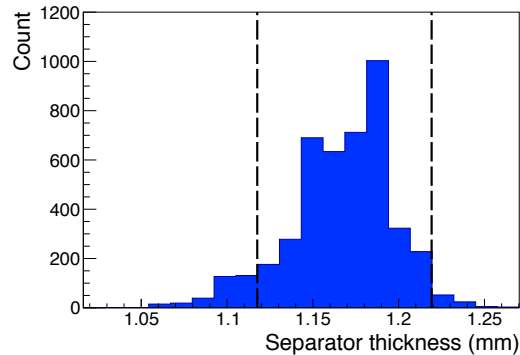


Figure 4.13. Thickness measurements made on 351 separators, where the dashed line represents fabrication tolerances.

5% of all produced PLA rods were measured to ensure their dimensional uniformity among batches of production. Dimensional repeatability of 3D printing of PLA was demonstrated at the  $\pm 0.13$  mm level through the measurement.

**4.3.6 Optical Performance of the Optical Grid.** The separator reflectance was measured with an Ocean Optics STS-VIS spectrometer to ensure optical uniformity. The relative total reflectance (specular+diffuse) comparing to a smaller separator sample and the absolute diffuse reflectance were measured. As shown in Figure 4.14, the total reflectance of all separators varied within 2%, and the diffuse reflectance was  $< 10\%$ .

The scintillation light reflects on the separator surface with random incident angle. Ensuring reflectance uniformity with different incident angles of light is essential. A laser goniometer was built at IIT to measure the correlation between

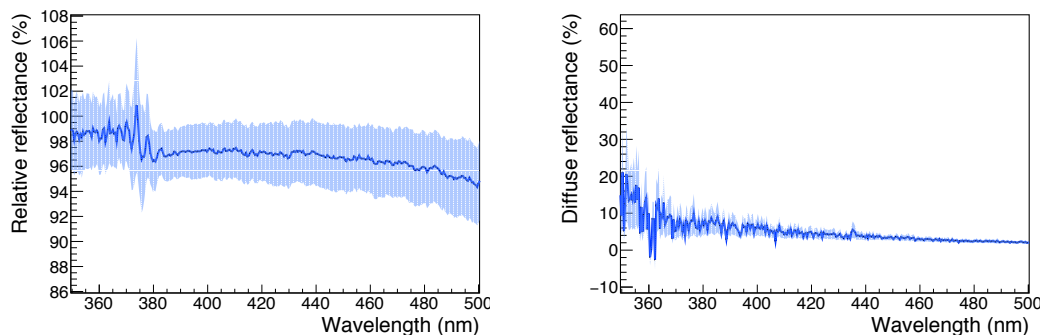


Figure 4.14. (Left) The relative reflectance of the mass production separators compared against a  $5\text{ cm} \times 5\text{ cm}$  separator sample with  $1\sigma$  error, showing 5% of difference from the sample but  $\pm 2\%$  variation among all separators. (Right) The diffuse reflectance of the mass production separators with  $1\sigma$  error, exhibiting  $< 10\%$  absolute diffuse reflectance.

reflectance and incident angle in EJ-309. The result of the goniometer measurement is shown in Figure 4.15. With increasing incident angle, the reflectance of bare DF2000MA decreases significantly in EJ-309 beyond  $50^\circ$ , while the reflectance of the separator remains flat because of the total internal reflection from the FEP film at large incident angles.

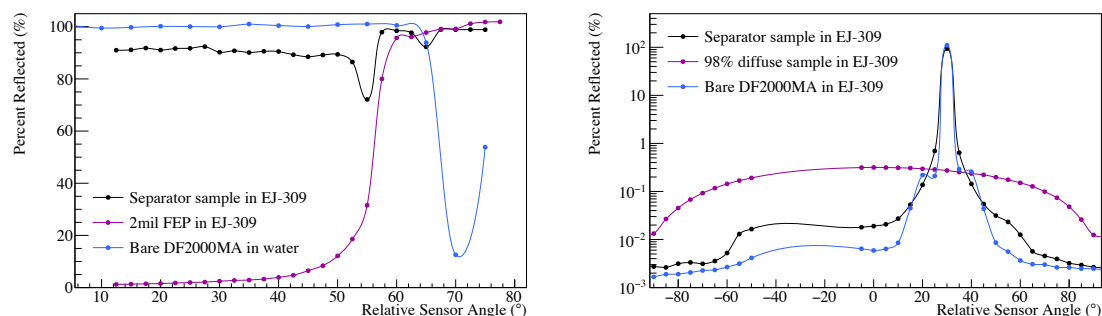


Figure 4.15. The results of goniometer measurements on PROSPECT's separator sample. (Left) The specular reflectance of the laminated separator sample, FEP and bare DF2000MA in clear liquid, with respect to incident angle, shows the total internal reflection effect at large angle. (Right) The diffuse reflectance measured by the goniometer. The bare and laminated reflector compared against a 98% diffuse reflective sample.

The optical characterization of PLA rods is shown in Figure 4.9. The light reflection of the PLA rods is dominated by diffuse reflection, with 65% to 75% absolute

diffuse reflectance. Comparing to the separator, the specular reflectance of the PLA rods is 2% to 3%. By comparing the reflectance of PLA backed by reflector and light trap, the light transmitted through a wall PLA rod is  $< 1\%$ .

**4.3.7 Optical Grid Compatibility.** The compatibility of the separator and PLA rods with  $^6\text{LiLS}$  were tested by long term  $^6\text{LiLS}$  quality monitoring. Samples of the separators and PLA rods were soaked in  $^6\text{LiLS}$ . When testing compatibility, the  $^6\text{LiLS}$  contacted by each material was subjected to light absorbance spectroscopic measurements with an Agilent Technologies Cary 5000 UV-Vis-NIR spectrometer. Incompatible material can cause a change in the absorbance spectrum of  $^6\text{LiLS}$ , comparing to a reference  $^6\text{LiLS}$  sample. The result of 6-month-long monitoring measurements are shown in Figure 4.16, indicating no significant change in the absorbance spectrum comparing to the reference.

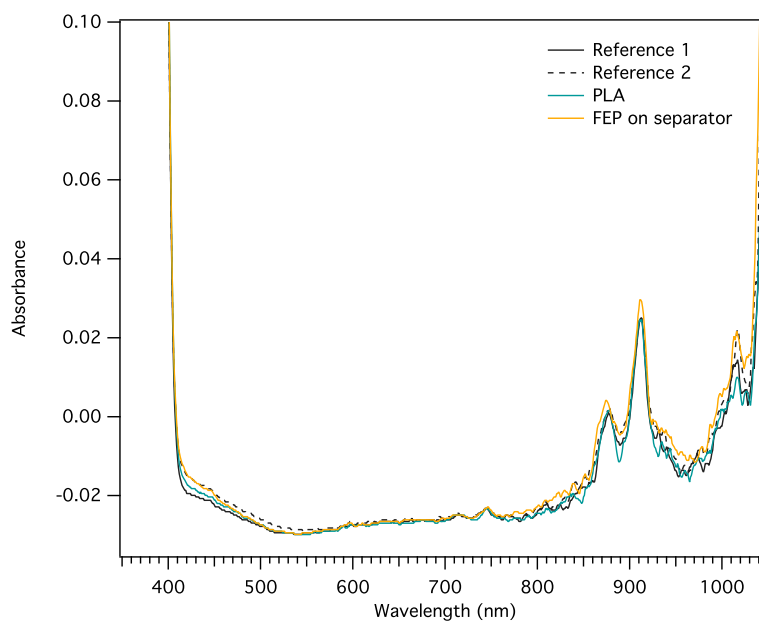


Figure 4.16. The absorbance spectra of  $^6\text{LiLS}$  in contact with selected samples. After 6 months of contact with different detector components, all test liquid samples showed similar absorbance spectra compared with references.

The PLA rod mechanical stability while in contact with  $^6\text{LiLS}$  is also tested by a stressed lever test as shown in Figure 4.17. A 100 kPa stress is precisely applied to

the PLA rod at the fulcrum by adjusting the weight and lever arm length. The applied stress was calculated with an assumption of a square-shaped PLA rod cross-section. EJ-309 was dropped at the fulcrum to maintain constant contact with PLA rod at the stressed spot. In the 14-month-long lever test, the PLA rods with and without EJ-309 exposure remain straight, demonstrating PLA rods' mechanical stability.

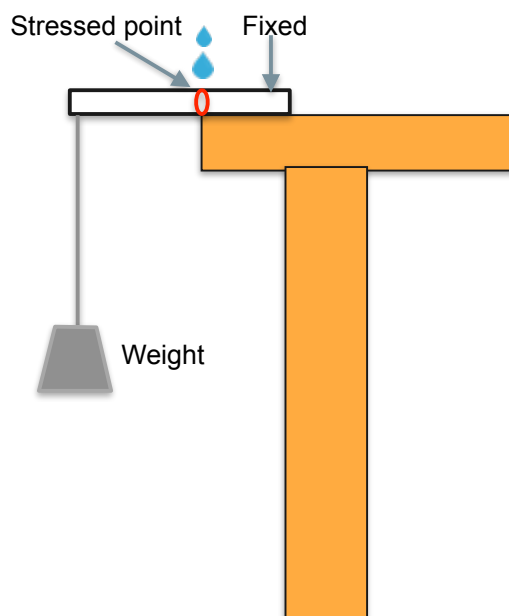


Figure 4.17. A schematic of the lever test, where the liquid drops represent  ${}^6\text{LiLS}$ .

#### 4.4 PMT Modules

As mentioned in Figure 3.5, PROSPECT utilizes two types of PMTs with 12.7 cm diameters and similar characteristics, including 240 Hamamatsu R6594 SEL PMTs and 68 ADIT ElectronTubes 9372KB PMTs. To avoid light leakage and cross-talk among segments, the PMT module was designed with the purpose of creating light-tight segments within the optical grid. Therefore, all PMTs are contained in the PMT housing shown in Figure 4.18 so that the PMT modules can be assembled inside the detector inner volume and submerged in  ${}^6\text{LiLS}$ . The front window, sidewalls, and back plugs of the PMT housing are transparent, white-dyed, and black-dyed

acrylic, respectively. Each housing is filled with optically clear mineral oil to minimize the pressure difference between the inside and outside of the housing. A 150 cc gas-filled bag inside the housing dampens any pressure variations due to thermal expansions. The mineral oil and conical reflectors on the interior surface at the front window compose a light guide portion of the segment to increase light collection. The dimensions of the sidewall are designed to fit precisely with the spacers of the end PLA rods. The back plugs of the PMT housings stack directly on each other in the PROSPECT AD. Hence, the segment dimension and variation is dependent on the dimension of PMT housings. The front windows of the PMT housings are by design not contacting the optical grid, but have approximately 1 mm gap between them and separators to allow for filling of  $^6\text{LiLS}$  into the segments. The back plug and cables were assembled into the module with O-rings for achieving the liquid-tight condition. All PMT modules were assembled in a class 1000 cleanroom at Yale University.

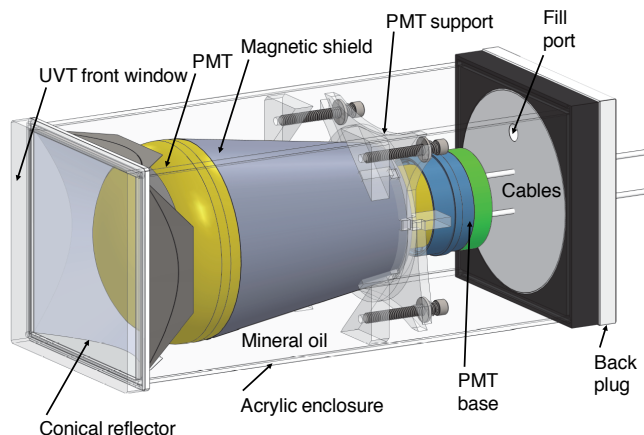


Figure 4.18. The detailed design of the PMT module.

The mass and volume of the PMT modules after filling of mineral oil were measured. Excluding cables, the mass of each Hamamatsu PMT module is  $5.78 \pm 0.12$  kg and the mass of each Electron Tubes module  $5.49 \pm 0.12$  kg. The volume of each PMT

housing is  $6.6 \pm 0.3$  liter.

All PMT modules were subjected to PMT resistance tests and functionality tests before being assembled into the PROSPECT AD. The PMT resistance was measured with multimeters during assembly. In PMT functionality tests, groups of 16 fully assembled PMT modules were placed in a dark box where a laser-pulse LED was deployed as a light source. The PMT modules collected single photoelectron (PE) data with a variety of high voltage (HV) applied. PMT modules with abnormal light response were re-assembled or rejected.

#### 4.5 Calibration System

The calibration system of PROSPECT consists of the  $^{227}\text{Ac}$  spiked in the  $^6\text{LiLS}$  (see Section [4.2](#)), optical calibration systems (OCS) inserted in the detector through some of the PLA rods, and radioactive source calibration systems [\[84\]](#). The schematic of the OCS and the radioactive source calibration setup is shown in Figure [4.19](#).

The goal of optical calibration is to characterize the single PE response of every segment by calculating the mean ratio of analog-digital converter (ADC) channel to count of PE. The OCS consists of a 15 mW single mode fiber-pigtailed laser diode assembled to a modified center PLA rod as a diffuse 450 nm wavelength light source. All 42 light sources deployed at the center of the selected PLA rods are connected to a high-performance laser generator.

The radioactive calibration system inserts calibration sources into the detector to characterize detector response to physics events with known particle energy and vertex location. Radioactive sources are sealed in cylindrical aluminum capsules with stainless steel caps to keep the radioactive sources sealed. The capsules are attached to timing belts driven by motors installed outside of the shielded detector. To ensure smooth insertion of the calibration sources, polytetrafluoroethylene (PTFE) tubes

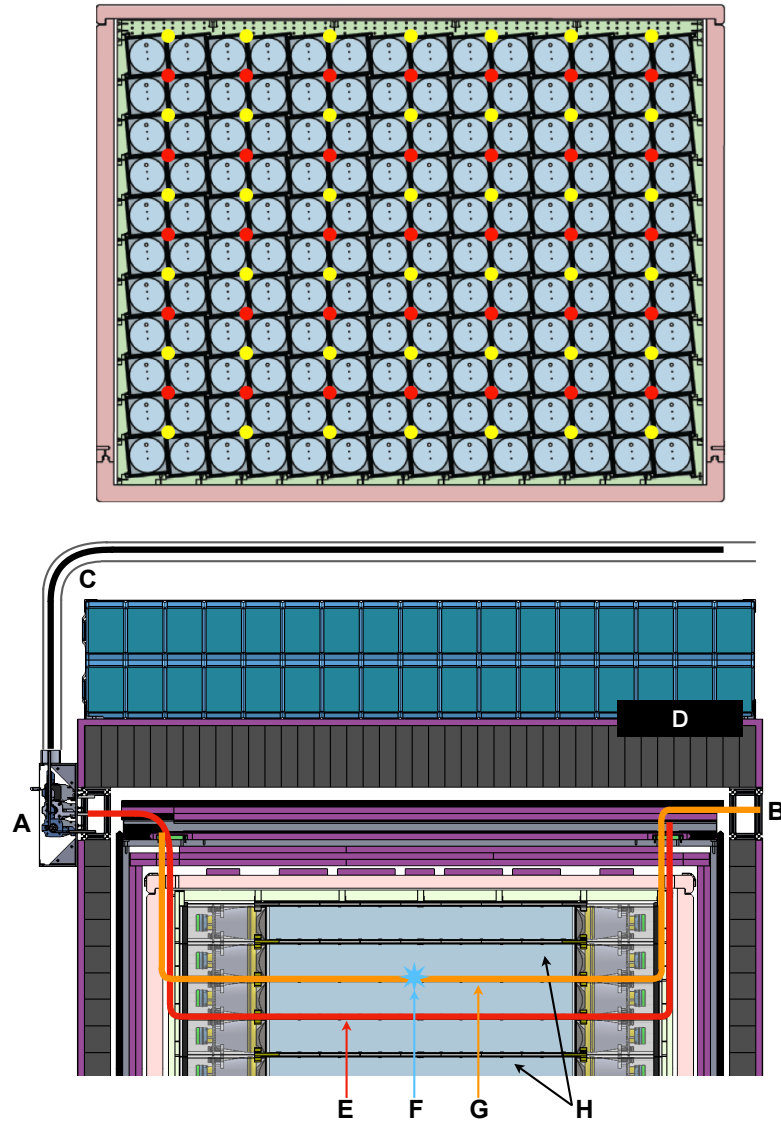


Figure 4.19. The setup of PROSPECT calibration system [76]. (Top) Locations of OCS and radioactive source calibration tubes are shown on the (X, Y) plane. Yellow dots represent the OCS tube location, while red dots represent the radioactive source calibration location. (Bottom) Detailed design of the calibration system along the axial direction (Z direction) of segments. (A) source drive motors, (B) optical fiber connector panel, (C) belt storage tube, (D) shielding, (E) source deployment tube, (F) light injection point, (G) fiber tube, (H) detector segments.

are installed in the 35 PLA rods for calibration. The PTFE tubes also prevent direct contact between  ${}^6\text{LiLS}$  and the calibration system. The dimensions of the capsules ( $r = 3 \text{ mm}$ ,  $l = 12 \text{ mm}$ ) are identical despite the differences in contained radioactive

isotopes. Because the capsule location is not visible in the detector, the calibration sources can be deployed precisely at the desired location by controlling the speed and time of source driving in the detector through 35 PLA rods as shown in Figure [4.19](#).

#### 4.6 Detector Construction and Commissioning

The detector construction and commissioning consists of several phases: components fabrication, detector inner volume assembly, dry commissioning, detector shipment,  $^6\text{LiLS}$  filling, wet commissioning, external shielding assembly, and calibration source driver assembly. The fabrication and assembly timeline is listed in Table [4.6](#). During my thesis research, I also played major roles in the detector assembly, filling, wet commission, and initial calibrations.

Table 4.5. The fabrication and assembly timelines, as well as the primary locations of each mile stone.

Milestone	Date (Location)
Separator Delivery to Yale	11/22/2016 (IIT) to 10/26/2017 (Yale)
PLA Delivery to Yale	10/20/2016 (Autotiv) to 07/26/2017 (Yale)
PMT Module Delivery to Yale	1/2017 (Yale) to 11/10/2017 (Yale)
Detector Assembly	10/30/2017 (Yale) to 11/17/2017 (Yale)
Detector Shipment	1/30/2018(Yale) to 1/31/2018 (ORNL)
$^6\text{LiLS}$ Filling	2/24/2018 to 2/25/2018 (ORNL)
Wet Commissioning	2/26/2018 to 3/17/2018 (ORNL)
External Shielding Assembly	2/28/2018 to 3/3/2018 (ORNL)
Calibration System Assembly	3/4/2018 to 3/5/2018 (ORNL)

The inner detector volume was assembled in a clean tent at Wright Laboratory,

Yale University. The detector components, including optical grid components, PMT modules, and acrylic support, were assembled on a 6.3 cm thick transparent cast acrylic base, which is also the base of the liquid-tight acrylic tank. All components were subjected to thorough cleaning procedures: soaking and rinsing with 1% Alconox solution (PLA rods were ultrasonic cleaned with the same solution) followed by Alconox removal with a 10 M $\Omega$ -cm water bath. PMT modules were wholly filled with mineral oil to minimize bubbles appearing at the front windows. The detector assembly was organized on a row-by-row basis. The pre-assembled components (pre-strung PLA rods, separators, PMT housings, acrylic support plates, and other connection hardware) necessary for building a single horizontal row of 14 PROSPECT segments were transported into the detector assembly cleanroom during one shift. At the beginning of each shift, final combinations of one separator and one strung PLA rod were pre-assembled together for ease of assembly. Procedures of assembly are briefly overviewed in Figure [4.20](#). Photographs of the detector assembly, in Figure [4.21](#), indicate the details of the component interlocking.

To ensure dimensional uniformity, a precise metrological survey was conducted after the assembly of every row with a custom-made aluminum gauge and laser height measurement system. This survey was conducted to measure the horizontal and vertical difference among assembled separators and PMT modules. The goal of the metrological survey is to constrain the segment volume variation within 1%. Additional  $\sim 0.25$  mm FEP shims were placed between PLA rod end spacers and PMT housing bodies in the next-row assembly as needed. Shim placements and thicknesses were dictated by the results of the metrological survey of the previous row. The calibration source guiding tubes were inserted into the desired PLA rods as the acrylic rods used to string the PLA rods were removed. Several temperature sensors were also inserted into specific PLA rods.

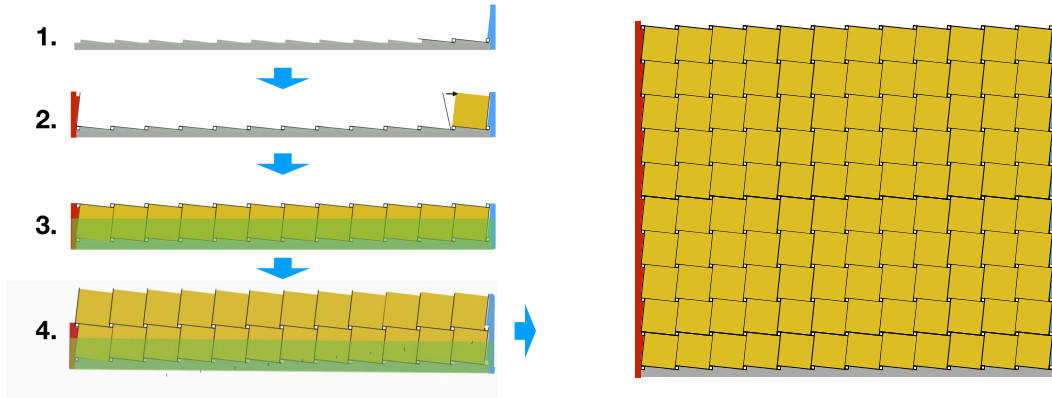


Figure 4.20. Illustration of the optical grid assembly procedure [80], where the black lines represent separators, the white squares represent PLA rods, the yellow squares represent PMT housings, and other colored parts are acrylic support plates. (1) The first-layer horizontal separators and PLA rods being assembled upon the base acrylic support plates. (2) The first-layer vertical separators assembled with PMT modules. (3) The second-layer horizontal separators and PLA rods assembled upon the first layer, closing the bottom row segments, with the green shade representing end acrylic support plates that constrained the PMT housing positions. (4) The following rows of segments were assembled similarly until the optical grid subsystem was assembled.

The assembled detector was contained a transparent acrylic tank with 6.3 cm thick walls, whose inner dimension is 1.995 m (wide)  $\times$  2.143 m (long)  $\times$  1.555 m (tall). The acrylic walls and base were combined with Viton o-rings to ensure a liquid tight condition. The lid of the acrylic tank allows the feeding of PMT signal and HV cables through. Environmental sensors, including liquid level sensors, oxygen level sensors, and nitrogen cover system, were also installed through this lid. After the detector was securely contained in the acrylic tank, the acrylic tank was moved into an aluminum tank. The dimensions of the aluminum tank are 2.255 m (wide)  $\times$  2.205 m (long)  $\times$  1.982 m (tall). The goal of the aluminum tank is to provide a light-tight condition of the PROSPECT AD and additional protection during detector shipment. Borated polyethylene boards with various thickness were filled between the acrylic tank and the aluminum tank, uniformly surrounding the former. A photograph of the acrylic tank and the aluminum tank is shown in Figure 4.22

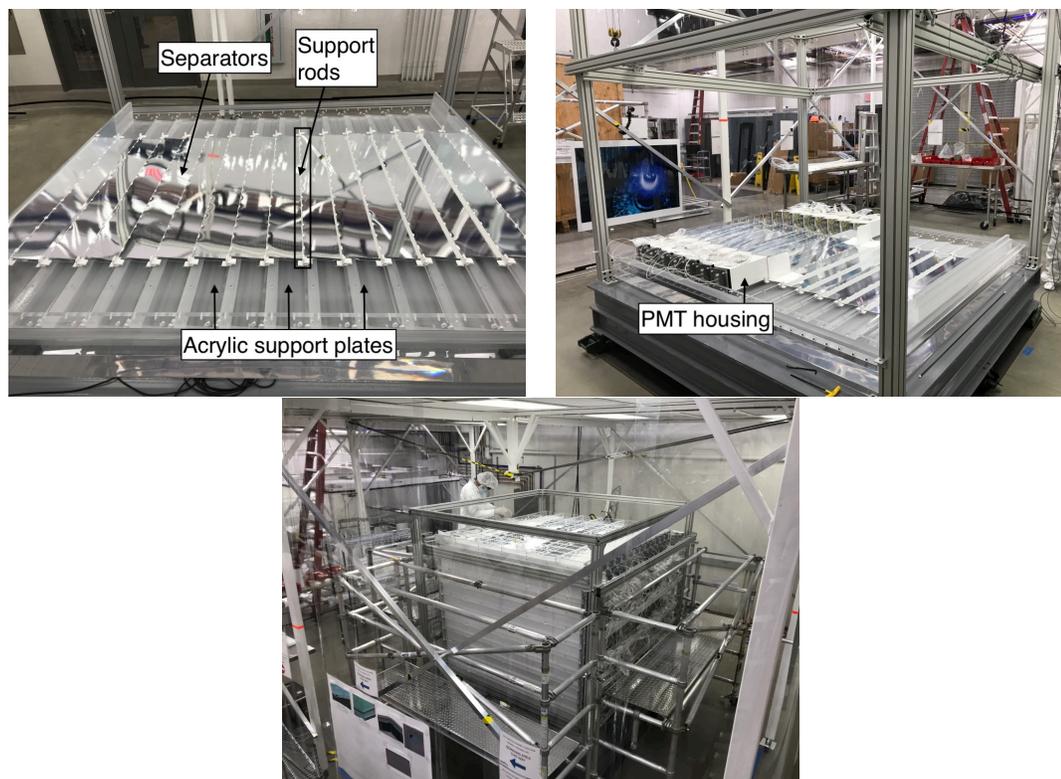


Figure 4.21. (Top left) The bottom layer of the assembled PLA rods and separators on the acrylic support plates. (Top right) The assembly of the bottom layer with PMT modules stacking on the acrylic support plates. (Bottom) Photograph of the assembled inner detector.



Figure 4.22. The aluminum (left) and acrylic (right) tanks as containment vessel of the PROSPECT inner detector volume.

The assembled PROSPECT AD was tested with an unfilled detector (dry commissioning) at Yale University, demonstrating the electronic performance and the data acquisition (DAQ) system via collecting the OCS data and cosmic ray background data. After the dry detector test, the PROSPECT AD was shipped from Yale University to the HFIR building. The detector was cushioned by 0.1 m thick foam underneath and 0.05 m thick foam surrounding, in a wooden shipment crate. A 3×3 detector mock-up was tested to simulate the vibration and shock during detector shipment. No damage was observed in the shipment simulation.

The  ${}^6\text{LiLS}$  were shipped in drums to ORNL with nitrogen cover gas. The temperature was controlled during the  ${}^6\text{LiLS}$  shipment. Before the detector filling, all  ${}^6\text{LiLS}$  was pumped into a 20-ton Teflon lined shipping container (ISO tank). Nitrogen was used as cover gas for both the detector and the ISO tank during the  ${}^6\text{LiLS}$  filling. The detector is tilted  $0.7^\circ$  along the axial direction of the segments to avoid bubbles being retained in the segments. The filling rate of the  ${}^6\text{LiLS}$  was set to 3 liter/minute with an ultrasonic sensor monitoring the liquid level. There were 4340 kg  ${}^6\text{LiLS}$  filled into the detector acrylic tank.

The external shielding includes a local shielding wall and detector passive shielding. The local lead shielding of a 0.1 m thickness was installed between the wall of the reactor pool and the detector. The detector's passive shielding appears in several layers surrounding the detector. From inside to outside, the passive shielding consists of a layer of 2.5 cm thick borated polyethylene, a layer of 2.5 cm thick layer of lead for gamma shielding, and a layer of 2.5 cm to 7.5 cm thick high-density polyethylene as a neutron absorber. On top of the detector, a layer of 0.46 m tall water bricks was added as additional overburden to suppress cosmogenic neutron background.

The radioactive source driving motors and the nitrogen flow control system

were installed outside of the shielded detector. The HV cables and signal cables were connected to a DAQ crate for full detector commissioning. A photograph of the installed detector is shown in Figure 4.23.

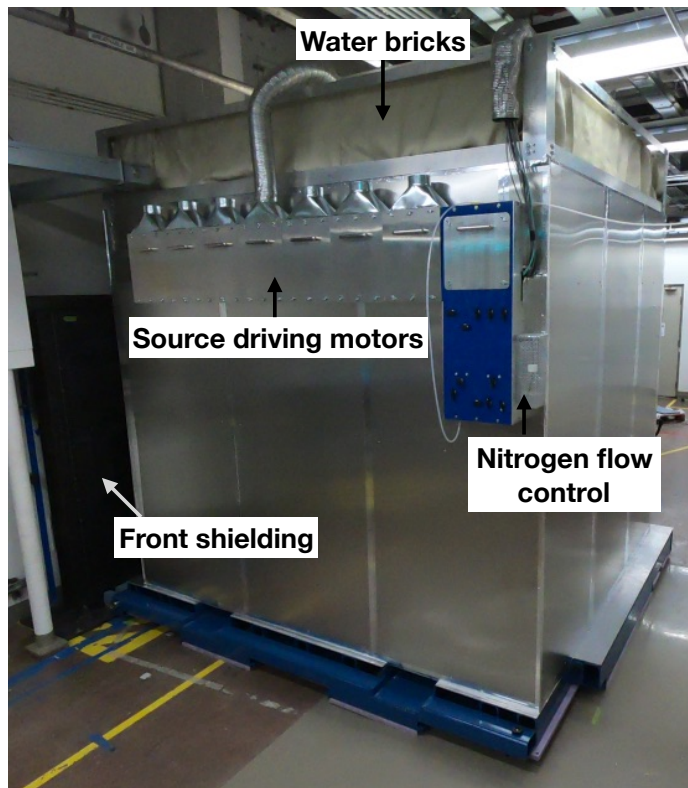


Figure 4.23. A photograph of the PROSPECT AD. The calibration source motors and nitrogen flow control systems were shown on the side of the detector.

#### 4.7 Data Acquisition System

The DAQ system, shown in Figure 4.24, is composed of 21 CAEN V1725 16-channel digitizers (ADC) with 250 MHz sampling rate, a Phillips Scientific 757D NIM Fan-In/Fan-Out module, two DAQ control systems, a local storage array, and a run control computer. Each channel of the digitizers is connected to one of the 308 PMT signal output cables. The ADCs are grouped into two, operated by two VME crates, and controlled by two computers.

The dynamic range of the data collection is set by adjusting the HV gain of

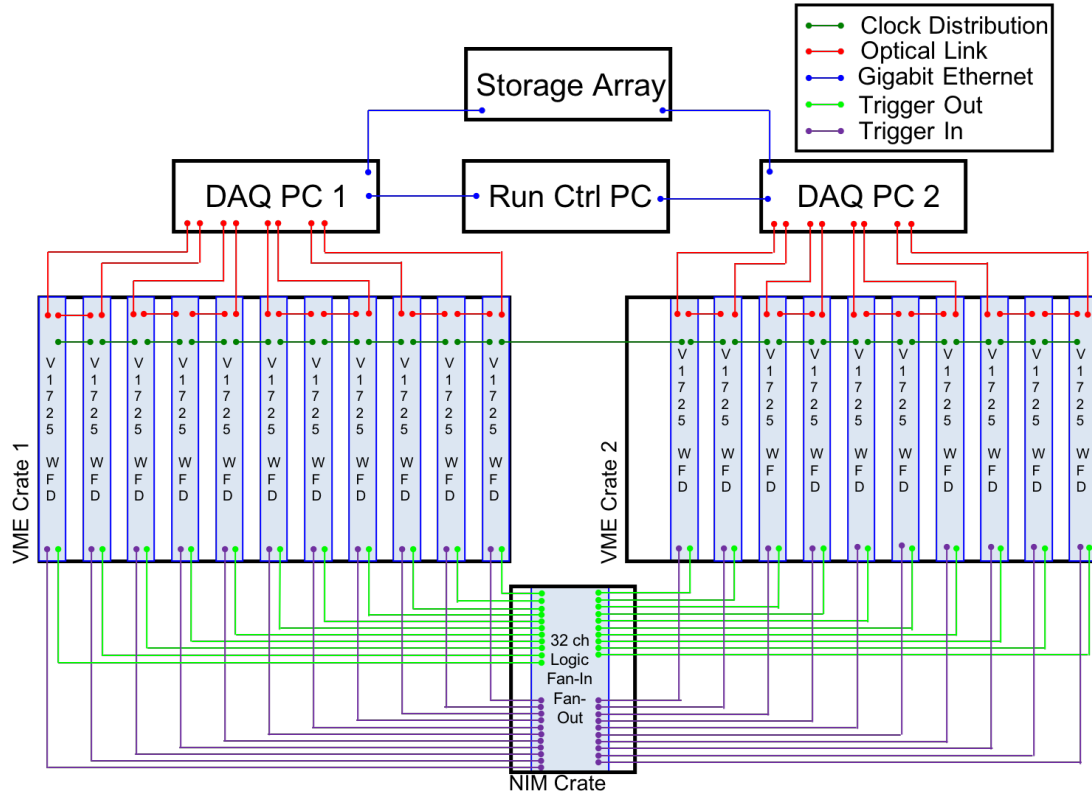


Figure 4.24. Schematic diagram of the DAQ system.

the PMT channels. In order to exclude cosmic ray background and cover the range of IBD prompt energy, as well as the cosmogenically produced  $^{12}\text{B}$  beta energy spectrum, the dynamic range of the general data acquisition is set to 15 MeV. During optical calibration, the dynamic range is narrowed down by increasing the gain to cover the single PE regime. The acquisition window of an ADC pulse is 148 samples long, equivalent to 592 ns. The DAQ triggering logic is shown in Figure 4.25. The DAQ system is triggered on thresholds of the ADC signal height collected from each PMT. A 50 channel primary trigger threshold, which is equivalent to the signal magnitude of approximately five PEs, is set (later changed to 25 channel considering light yield decrease) to trigger the DAQ logic. When the pulse heights from both PMTs of one segment exceeds the primary threshold within a 64 ns coincidence window, a zero length encoding (ZLE) threshold is set to trigger the light collection of each PMT.

The pulses from all PMTs whose height exceeds the 20 channel ZLE threshold, are recorded to the local storage. These thresholds were set to balance the PROSPECT AD's ability to reconstruct the 511 keV positron-electron annihilation gamma-ray and the size of lower energy datasets.

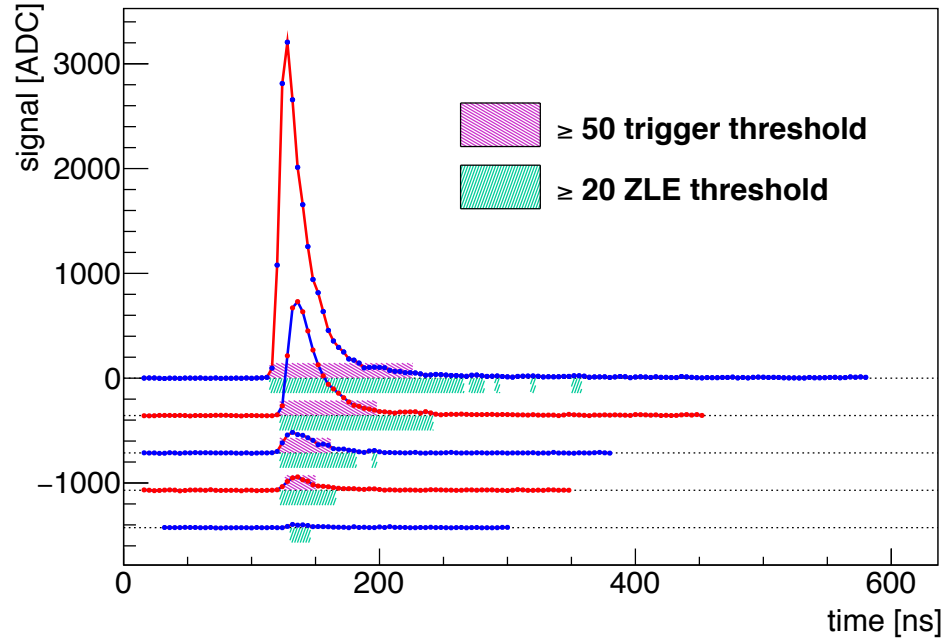


Figure 4.25. Example of a DAQ triggering signal, where the pulses are collected from different PMT channels. The DAQ trigger is generated by the coincidence of the highest pair of a pulse from a single segment. The following pulses with a height exceeding the ZLE threshold are saved in data.

Data acquisition runs are controlled through a run control computer, which can also be remotely controlled. An experiment operator can adjust the HV, and thresholds of the DAQ system through the run control computer. The collected data is temporarily saved at a local storage array and is transferred to a storage facility at Lawrence Livermore National Laboratory (LLNL).

## CHAPTER 5

### PHYSICS OF LIQUID SCINTILLATOR DETECTORS

The PROSPECT AD reconstructs event energy by collecting light produced by the  ${}^6\text{LiLS}$ . The PMTs of PROSPECT collect optical photons (photons with visible wavelength) from scintillation light yield. The light yield of the  ${}^6\text{LiLS}$  in response to an incident particle is not directly proportional to energy. Instead, complicated molecular effects in the scintillator, called Birks' quenching, causes nonlinear energy response. Additional nonlinear light yield is contributed from the Cherenkov radiation of charged particles with high enough energy. It is a vital step to understand the nonlinearity of light yield in PROSPECT to reconstruct particle energies and determine the absolute energy of  ${}^{235}\text{U}$ -produced  $\bar{\nu}_e$ .

#### 5.1 Organic Scintillator Light Yield

The  ${}^6\text{LiLS}$  of PROSPECT AD is an organic scintillator. The fluorescence process of organic scintillators is defined by the de-excitation photons of molecules from a variety of energy levels. Particle energy is absorbed by a scintillator molecule to excite its electron configurations. The de-excitation photon released by the excited molecule is the light yield of an organic scintillator. The scintillation photon yield per incident energy, referred to as scintillation efficiency, is a vital property of a specific scintillator. In an ideal energy-light conversion, the light yield with a scintillation efficiency  $S$  can be expressed as

$$\frac{dL}{dx} = S\left(\frac{dE}{dx}\right). \quad (5.1)$$

However, this efficiency is usually affected by radiationless de-excitation, such as molecular thermal motion, and light absorption by impurities, such as oxygen dis-

solved in an organic LS . The mechanics of energy deposition in the scintillator differs with different types of particle interactions.

**5.1.1 Beta Interactions.** Electron (betas) and positrons are the main subjects measured to reconstruct the reactor neutrinos' energy. Only a small portion of the beta particle's kinetic energy is converted to the scintillation light. The major beta energy absorption mechanisms are the collision with atoms in the medium and the Bremsstrahlung effect. Collisional loss is the major contributor for lower energy betas (below 10 MeV in  $^6\text{LiLS}$ ), where the energy loss is due to ionization and excitation of the atoms in the medium. The Bremsstrahlung effect absorbs electron/positron energy when the coulomb forces in the medium deflect it. The energy loss of beta particles is commonly calculated based on the material compound components with the ESTAR database [85], as shown in Figure 5.1, where the total energy loss is

$$\frac{dE}{dx} = \left(\frac{dE}{dx}\right)_c + \left(\frac{dE}{dx}\right)_r. \quad (5.2)$$

In the range of reactor neutrino produced IBD positron energy (0, 10) MeV, the major contributor of the positron energy loss is collisional loss. Because of the stopping power of the scintillator of PROSPECT, the length of the positron path is limited to a scale of several centimeters.

**5.1.2 Muon Interactions.** Interactions absorbing the energy of cosmic muons is similar to beta particle interactions. Due to its high kinetic energy and mass-to-charge ratio, a cosmic muon can travel through multiple segments of the PROSPECT AD. Occasionally, a Michel electron is generated when a muon decays inside of the detector volume.

**5.1.3 Gamma Ray Interactions.** Two gamma rays, each with 0.511 keV energy, are generated from the annihilation of an IBD positron. The annihilation gamma events are part of the IBD prompt event along with positron kinetic energy deposition as described in Section 5.1.1. Gamma energy is also utilized in energy scale calibration

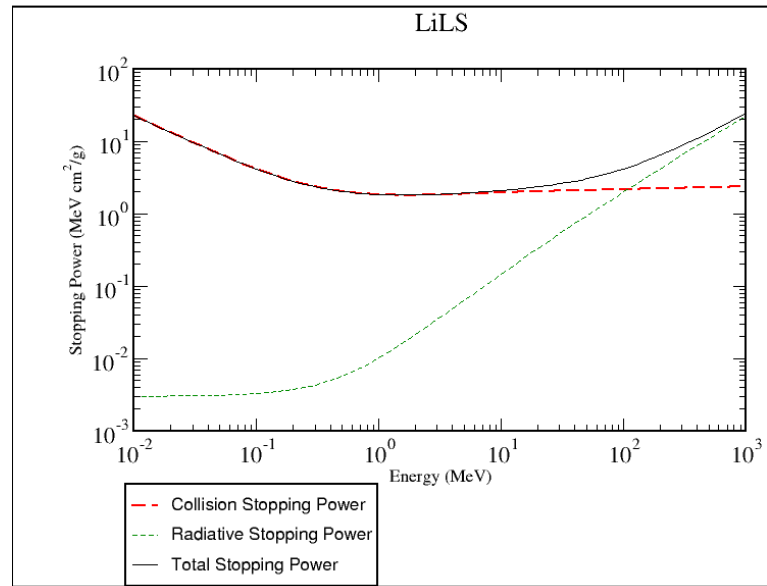


Figure 5.1. The electron  $dE/dx$  through  ${}^6\text{LiLS}$  calculated by E-star [85]. When electron energy is higher ( $> 10$  MeV), the Brestrahlung effect contributes more significantly.

for PROSPECT. Gamma interaction channels in scintillator include a photoelectric effect, Compton scattering, and electron-positron pair production.

Due to the photoelectric effect, gamma energy is partially absorbed by atoms in the medium. Photo electrons (PEs) are emitted in the process when gamma energy overcomes the binding energy of the electron at its original shell. A PE's energy generally ranges from the scale of 1 keV to 10 keV. The photoelectric effect is the major contributor causing energy loss of gamma rays with energy below 0.1 MeV. If a single energy gamma loses all of its energy through photoelectric absorption, its energy deposition in a large detector volume would be a delta function.

The Compton scattering of a gamma photon also emits free electrons in the medium. The energies of the scattered electron and gamma are dependent on the scattering angle. Thus, the Compton recoil electron energy is a continuous spectrum for a single energy gamma-ray input. The maximum energy of the Compton recoil

electron is obtained when the scattering angle is maximized. The energy difference between the incident gamma photon and the Compton recoil electron is given by

$$E_C \equiv E_\gamma - E_{e^-}(\theta = \pi) = \frac{E_\gamma}{1 + 2E_\gamma/m_e}. \quad (5.3)$$

The cross-section of Compton scattering as a function of the scattering angle is dependent on the medium's electron structure and density.

When the energy of the incident gamma exceeds the 1.022 MeV energy threshold, the electron-positron pair production reaction can occur among the gamma ray interactions. Ideally, the total energy of the electron and positron pair equals the gamma energy. The probability of pair production varies with respect to the absorber's atomic numbers.

The photoelectric effect mainly absorbs gamma energies below 0.1 MeV. When the energy of a gamma-ray exceeds the pair production threshold, pair production becomes a major cause for gamma energy loss in the higher energy range. The Compton scattering cross-section varies with gamma energy but becomes the most significant contributor of gamma energy absorption between 0.1 MeV to 10 MeV. Hence, Compton scattering is the major cause of gamma energy loss in PROSPECT's IBD measurement. Despite the type of interaction, a gamma photon energy is measured through its interaction generating electron and positrons. Therefore, the PSD signature and the detector response to a gamma-ray is similar to a beta particle, with the exception that gamma-ray energy deposition spreads significantly farther in distance than an MeV-scale beta in organic scintillator.

**5.1.4 Heavy Nucleon Interactions.** As described in Chapter 3, PROSPECT relies on the  $n$ - ${}^6\text{Li}$  capture interaction to tag IBD event candidates. The alpha particle and triton products of the  $n$ -Li capture lose their energy as charged particles.

Charged heavy particle energy is absorbed through coulomb force interactions.

When charged nucleons enter media, the coulomb force between the nucleons and orbital electrons excites the electrons to higher energy states or ionizes the atom. Thus, alpha particles, tritons, and protons excite scintillator molecules similar to electrons and positrons. For a 1 MeV scale charged nucleon, the energy loss  $dE/dx$  is significantly higher because of the higher cross-section for ionization and collision with atoms.

Unlike particles described previously, neutrons do not deposit energy through ionization directly due to its neutral electrical charge. Therefore, the neutron energy loss mechanism is dominated by interactions with charged particles. In particular, fast neutrons can transfer kinetic energy to a proton, alpha particle or nucleus in the medium, causing a recoil of charged heavy particles. During recoil interactions, fast neutrons are slowed down and eventually lose most of their kinetic energy. The inelastic scattering between a neutron and another nucleus transfers neutron energy to the nucleus, which de-excites by emitting a gamma photon. Thermal neutrons, with kinetic energy less than 0.025 eV, can be captured by proton-abundant atoms like hydrogen, boron, and lithium with high probability. Typical products of neutron capture are isotopes in excited states. De-excitation gamma photons from the product isotopes can be detected. In the case of the  $n$ -Li capture process, an alpha particle and a Triton are generated.

## 5.2 Birks' Quenching

A scintillator's light yield is ideally proportional to the energy loss as in Eq. [5.2](#). In reality, the quenching effect in an organic scintillator causes nonlinear light yield with respect to the energy deposition. Multiple factors affect the quenching effect, including radiationless molecular movements and the impurities in components absorbing the energy of scintillation light. A semi-empirical light yield conversion was developed by Birks [\[86\]](#)[\[87\]](#). This conversion is referred to as Birks' Law, which is

based on experimental measurement of organic scintillators' light yields and the theoretical assumption that the quenching effect varies with incident event ionization density. Birks' Law of scintillator quenching is expressed as

$$\frac{dL}{dx} = \frac{S \frac{dE}{dx}}{1 + k_{B1} \frac{dE}{dx} + k_{B2} \left(\frac{dE}{dx}\right)^2}, \quad (5.4)$$

where  $k_{B1}$  and  $k_{B2}$  are the first and second order Birks' constants that vary for different scintillators. Nonlinearity of light yield is severe at lower energies near the Bragg peak of the concerned particle.

Birks' Law also indicates significantly lower light yield from incident particles with high  $\frac{dE}{dx}$ . Thus, the effective light yield efficiency from protons and alpha particles is generally lower than electrons and gamma photons, resulting in severe differences between experiment-reconstructed energy and the actual deposited energy. The reconstructed energy is hence referred to as MeV electron equivalent (MeVee). For instance, the total energy of the alpha particle and Triton from  $n$ -Li capture is 4.78 MeV, while its PROSPECT detector reconstructed energy is  $\sim 0.55$  MeVee. The nonlinear scintillation response to different particles with various energy is shown in Figure [5.2](#)

Different scintillators have unique sets the Birks' quenching constants  $k_{B1}$  and  $k_{B2}$ . Measurements of  $k_{B1}$  and  $k_{B2}$  are usually made by comparing the electron and heavy-ion light yields at constant incident energy. However, the measured quenching constants are particularly challenging to simulate in most experiments due to large uncertainty of  $dE/dx$  calculation in MC simulations. The method used in PROSPECT simulations is discussed in Chapters [6](#) and [7](#).

### 5.3 Cherenkov Radiation

Photons produced through Cherenkov radiation [\[88\]](#) are another source of light in PROSPECT. When a charged particle's speed in a medium is higher than the phase

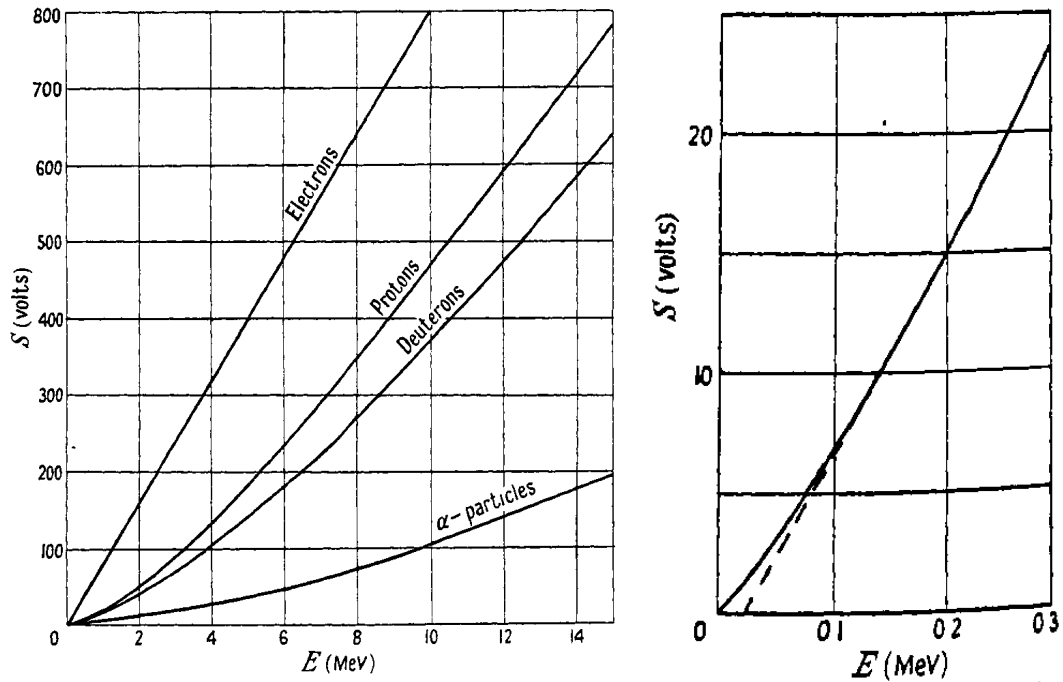


Figure 5.2. (Left) The nonlinear scintillator response to different particle types [86]. (Right) The light response of a scintillator to low energy electrons.  $S$  is the light signal output of Birks' measurement with organic scintillator anthracene. Because of high  $dE/dx$ , protons and alpha particles produce significantly less scintillation light per MeV, compared to an electron.

speed of light, a Cherenkov photon is emitted as the polarizable medium molecules are polarized by the charged particle. Coherent light is radiated at an angle with respect to the particle's traveling direction and speed. The number of photons generated in Cherenkov radiation is

$$\frac{d^2 N}{dx d\lambda} = \frac{2\pi\alpha z^2}{\lambda} \left( 1 - \frac{1}{\beta^2 n^2(\lambda)} \right), \quad (5.5)$$

where  $N$  is number of photons,  $\alpha$  is the fine structure constant,  $z$  is the particle's electric charge,  $\beta$  is the speed of the particle, and  $n(\lambda)$  is the index of refraction of the medium. The actual optical spectrum of the Cherenkov light is dependent on the scintillator index of refraction, transmission efficiency, and absorbance. The thresholds of Cherenkov radiation production for electrons and gammas are shown in Figure 5.3, where the threshold for electrons is  $\sim 0.2$  MeV when the medium index of

refraction is 1.5.

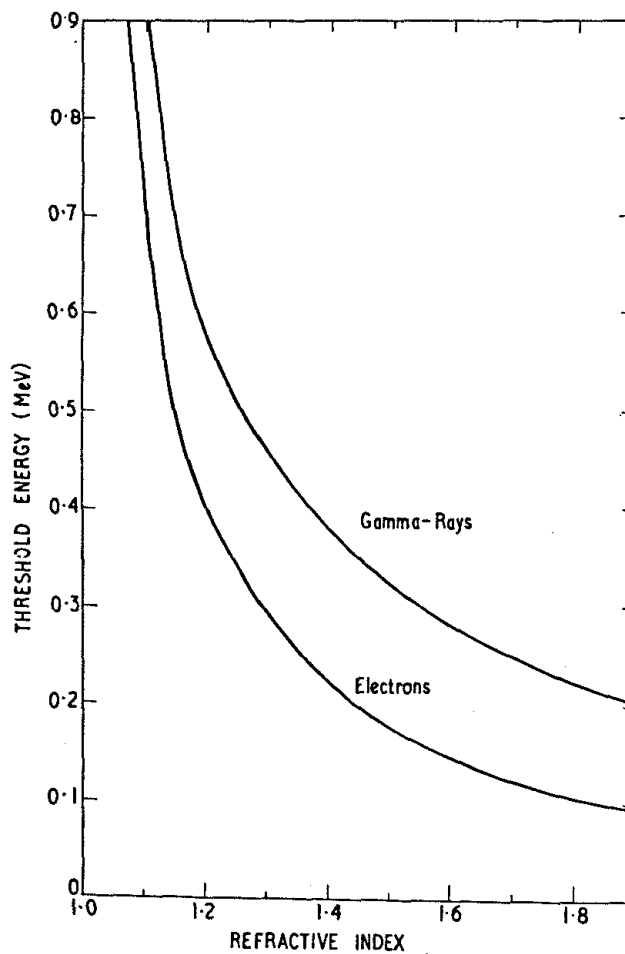


Figure 5.3. The Cherenkov radiation thresholds of gammas and electrons in media with different indices of refraction.

Cherenkov radiation of charged particles produce prompt photons in the PROSPECT AD that is indistinguishable from scintillation light. The nonlinear energy response caused by Cherenkov radiation is discussed in Chapters [6](#) and [7](#).

## CHAPTER 6

### MONTE-CARLO SIMULATIONS FOR PROSPECT

In PROSPECT’s reactor neutrino measurement, Monte-Carlo simulation (MC) is necessary to

- Test detector configurations during R&D
- Characterize detector performance
- Study detector energy response to a variety of particles
- Determine systematic uncertainties of detector geometry and light response
- Generate spectrum models and toys for parameter searches and sensitivity studies

PROSPECT-G4 (PG4) is the PROSPECT customized MC simulation package programmed based on the Geant-4 [\[89\]](#) toolkit. This simulation package allows users to adjust detector geometries and material properties to provide important information guiding detector design. PG4 was developed with prototype detectors; and was used to demonstrate the simulation’s reproduction of calibration data. Because of limitations in computing resources and time, PG4 contains necessary simplifications in its description of PROSPECT’s detector geometry and particle interactions. Adjusting PG4’s simulation of detector geometry, particle generation functions, and energy response is one of the essential parts in my thesis research.

#### 6.1 Geometrical Simulation

PROSPECT detector configurations are simulated in PG4. The simulated structures include  ${}^6\text{LiLS}$ , the optical grid, PMT modules, containers, and shielding.

Although most of the materials utilized in the PROSPECT AD are saved in Geant4 material databases with their chemical components and densities,  ${}^6\text{LiLS}$  is customized in PG4 by characterizing the density, chemical components, and doping percentage of the scintillator. The simulated  ${}^6\text{LiLS}$  is composed of  $0.9781\text{ g/cm}^3$  density EJ-309, which is composed of 84.14% C, 9.52% H, and 6.34% O by weight. Additional water and LiCl solution was added with the concentration easily adjustable in simulation. The reflectances of the optical grid separators are set based on direct optical measurements described in Chapter 4.

Some approximations was made to simplify the programming and running of PG4. The DAQ cables and systems are not included in the simulation because they do not contribute dead volume to the active detector volume. For simplicity of programming, the separator pinching tabs of PLA rods are continuous from end to end along each cell. The separator materials consist of only FEP films, and carbon fibers, as the density and chemical components of other laminated materials are not known.

For the radioactive calibration system, only calibration source capsules are simulated in PG4; the source driving components have minimal affect on dead volume in the detector. The source capsule materials and dimensions are programmed according to the actual design.

The on-site shielding wall and the detector shielding walls are also simulated based on the designed material and dimensions.

## 6.2 Particle Generation and Interaction Simulations

Because of neutrinos' low IBD cross-section, direct neutrino simulation is not realistic in PG4. Instead, IBD produced positrons and neutrons are generated to mimic the IBD interaction in the detector. In PG4 simulation, each IBD event con-

tains a positron-neutron pair generated from the same vertex with their sum of energy equal to a user defined neutrino energy plus a rest proton energy (the IBD total energy). The IBD total energy and vertex position can be adjusted for different analysis purposes, including model generation, detector response studies and uncertainty calculations. In the special case of simulating the reactor neutrinos generated from HFIR, IBD total energies are generated based on the Huber model of the reactor neutrino spectrum [67]. As the reactor location is approximately  $45^\circ$  below the PROSPECT detector, the angular distribution of the IBD products is implemented as shown in Figure 6.1.

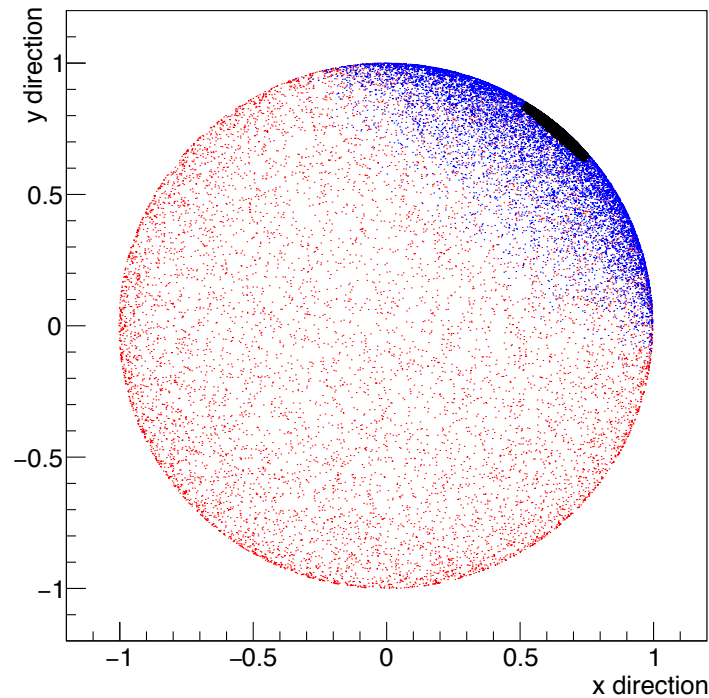


Figure 6.1. The simulated IBD products' angular distributions, with red dots representing positrons and blue dots representing neutrons.

Radioactive sources utilized in calibration are simulated in PG4 with custom built particle generators. The gammas and electrons of the calibration sources are generated from user defined vertexes with energies extracted from the energy levels

and transition probabilities saved in the ENSDF database [45]. For the  $^{252}\text{Cf}$  spontaneous fission neutron source, the emitted neutrons and gammas from its fission reaction are simulated instead of directly simulating the fission process.

The cosmic ray background is simulated with the external cosmic ray shower generator CRY [90].

### 6.3 Truth-level Simulation

Identification of particle type (PID) of PG4 is consistent with Geant4, which uses PDGID [42] of particles. In the case of neutron capture events, the  $A$  and  $Z$  values of the neutron capturing atoms are recorded.

Particle energy depositions and positions in the detector are tracked with the `G4Track` and `G4Step` objects, as illustrated in Figure 6.2. `G4Track` is a snapshot of a particle. Every two points in `G4Track` are connected by `G4Step`. Every two steps are separated by 1) a particle interaction, 2) particle traversal through the boundary of two geometrical volumes in Geant4, 3) a particle traveled the maximum length of each step, 4) a particle stops or exits the simulation world volume. `G4Track` saves the particle's PID, energy, and position information. `G4Step` saves the particle's energy loss from the beginning to the end of a step. Therefore, a particle's energy deposition in each segment of the PROSPECT AD can be saved by summing the the energy deposits in all steps in a segment. Each `G4Step`'s maximum length is set by user. The step size is independent of particle energy and current medium. As a result, the  $dE/dx$  calculated in each step does not precisely reflect actual material stopping power.

PG4's ability to track a particle's energy loss step-by-step enables simulation of nonlinear detector response. In Chapter 5, the Birks' quenching function is deter-

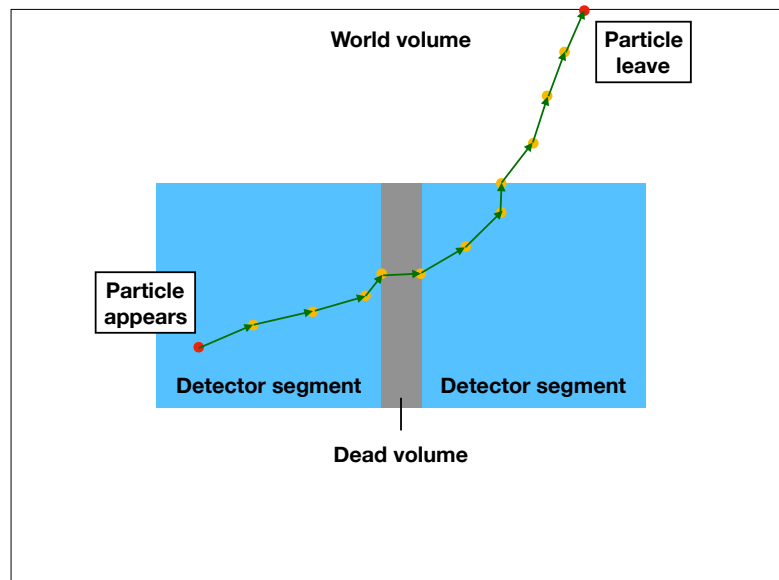


Figure 6.2. An illustration of PG4 event tracking, where an arbitrary is recorded. The yellow dots and the arrows connecting among them represent **G4Tracks** and **G4Steps**.

mined as

$$\frac{dL}{dx} = \frac{S \frac{dE}{dx}}{1 + k_{B1} \frac{dE}{dx} + k_{B2} \left(\frac{dE}{dx}\right)^2}. \quad (6.1)$$

Using the  $dE/dx$  calculated by each step, the quenched light yield can be effectively expressed as the reduction of energy deposition

$$\frac{dE_{quench}}{dx} = \frac{\frac{dE}{dx}}{1 + k_{B1} \frac{dE}{dx} + k_{B2} \left(\frac{dE}{dx}\right)^2}. \quad (6.2)$$

Hence, the quenched energy of a particle is

$$E_{quench} = \sum_i^{steps} \frac{\frac{dE_i}{dx}}{1 + k_{B1} \frac{dE_i}{dx} + k_{B2} \left(\frac{dE_i}{dx}\right)^2}, \quad (6.3)$$

where  $k_{B1}$  and  $k_{B2}$  are effective Birks' constants, since the  $dE/dx$  calculated in each **G4Step** differs from actual material stopping power. PG4's simulation of Birks' quenching is a unique approach in particle detector simulation. It allows the user to adjust the detector's nonlinear response by changing the quenching factors ( $k_{B1}$

and  $k_{B2}$ ) of the simulated detector. This is a necessary simulation feature because the event reconstruction for the segmented PROSPECT AD is complicated, as discussed in Chapter 8.

Cherenkov radiation can also be simplified using the energy loss and speed of particles calculated by PG4. Because of limited computing resources, optical photon simulation for high energy interactions is unrealistic. As discussed in Chapter 5, the number of photons generated as Cherenkov radiation is expressed as

$$\frac{d^2 N}{dx d\lambda} = \frac{2\pi\alpha z^2}{\lambda} \left(1 - \frac{1}{\beta^2 n^2(\lambda)}\right). \quad (6.4)$$

By learning the detector's light transmission spectrum and wavelength shifting efficiency, the optical spectrum of the Cherenkov photon can be used to calculate additional light collection from it. An effective Cherenkov photon contributed energy  $E_c$  can be added to the effective energy in PG4,

$$E_c = k_c \sum_{\lambda} N_{\lambda} E_{\lambda}, \quad (6.5)$$

where  $E_{\lambda}$  is the energy contributed by each photon,  $k_c$  is an effective *Cherenkov energy* coefficient. The contribution of  $E_c$  to the reconstructed energy is adjustable by the user in energy response studies as discussed in Chapter 8.

## 6.4 DAQ Pulse Simulation

The MC output of the PG4 simulation is converted to files with structures identical to actual PROSPECT data. The purpose of this conversion is to force MC simulation to be consistent with detector responses at different times, because the evolution of detector response over time has been observed. The structure of the PG4 MC output and the actual PROSPECT data are shown in Figure 6.3. A PG4 MC output contains primary particles and particle interactions, where the 'ionization event' saves the energy deposition and timing information in each segment. The 'neutron capture' category is set to save the neutron interaction, especially the

neutron-atom interaction to record the neutron capture events and the interactions related to the events. The low level PROSPECT ‘detector pulse data’ saves the ADC timing and channel information. The ‘physics data’, also referred to as high level data, saves the event position, time, reconstructed energy and PID information based on calibration and analysis of the low level pulse data. These data processing and calibration procedure is discussed in Chapter 7 and 8.

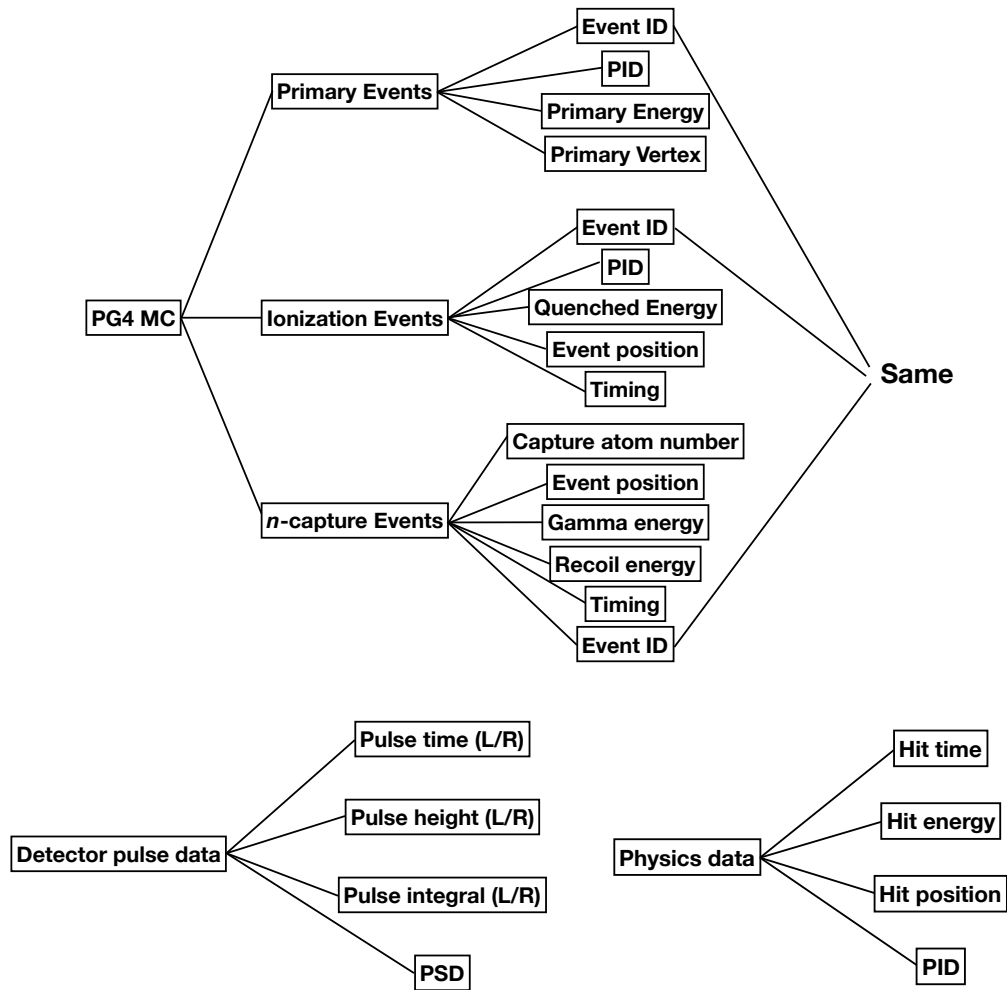


Figure 6.3. A schematic of the data structure of MC simulation and the actual PROSPECT data. (Top) The structure of PG4 output, where the recorded categories share same event IDs. (Bottom left) The low level DAQ pulse data from unpacking the raw data. (Bottom right) The high level physics data of the PROSPECT AD calibrated from the DAQ pulse data.

The PG4 output is converted to simulated pulse and physics data through energy-ADC pulse conversion, which is a reversed conversion of the usual detector calibration, as shown in Figure 6.4. PROSPECT's detector response information at different times, consisting the light response, DAQ gain setting, and PSD distributions, is saved in the PROSPECT calibration database. The MC energy deposition is converted to ADC channels based on this PROSPECT calibration database. The calibration database saves ADC-energy calibration values with respect to time, and the template pulse shapes of different particles at each PMT channel. Hence, the MC events can be converted to the simulated pulse data with PSD values, PMT pulses, and event time coincidences with time and position variations taken into consideration. The simulated pulse data can be calibrated to obtain simulated physics data, which is discussed in Chapter 7. These procedures ensure precise detector response simulation even in the presence of non-uniformity and time-variation of the detector response.

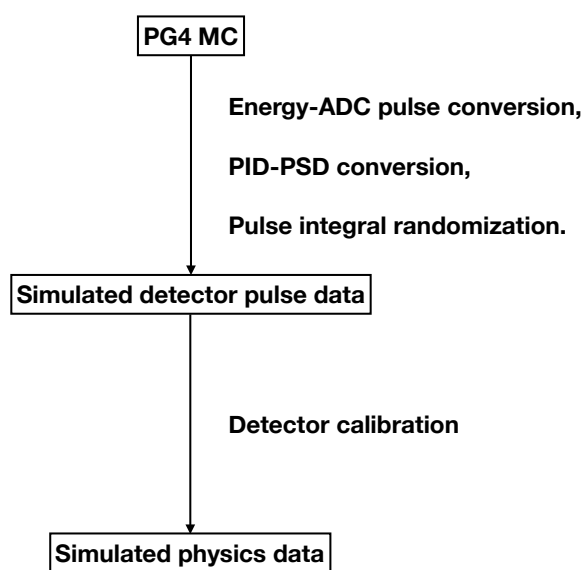


Figure 6.4. A schematic of PG4 output conversion procedures.

## CHAPTER 7

### DATA PROCESSING AND LOW-LEVEL CALIBRATION

The purpose of detector calibration is to convert the raw DAQ signal output to event information with physical meaning. The raw output of the from CAEN digitizers of the DAQ system is in binary format. To convert the DAQ signal output to calibrated data, multiple procedures of data processing, shown in Figure [7.1](#), are required.

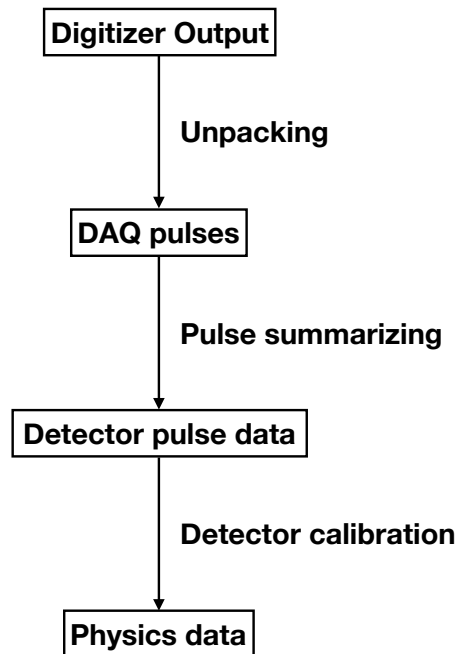


Figure 7.1. Schematic of the data process procedures.

#### 7.1 Data Processing

The raw output from the digitizers are unpacked from the binary format data of each DAQ channel to actual pulses collected by each channel. The information

saved after unpacking includes the absolute time of each sample, the event number assigned to a group of pulses close in time, the channel number and the values of all ADC samples in a pulse. The unpack procedure contains minimum data analysis, merely converting the digitizer output to human-readable format.

The unpacked data saves all samples of every pulse and requires substantial disk space. Summarizing the unpacked pulse data is necessary for the ease of accessing the data. In the pulse summarizing procedure, each pulse's height, integral, absolute time, channel number and PSD value are saved. The summarized values are the key variables used in event reconstruction, including time, reconstructed position, and reconstructed energy.

## 7.2 Timing Calibration

A particles energy deposition, detected by both PMTs of a segment, is referred as a *hit*. A group of hits close in time is defined as a *cluster* detected by the PROSPECT AD. In addition, many of the particle interactions in the PROSPECT AD, including IBD, are identified by time coincidences between clusters. The position reconstruction of each hit relies on accurate timing difference between two PMTs.

**7.2.1 Time Reconstruction.** Because the sampling rate of the digitizers are 250 MHz, the time difference between two samples is 4 ns. The reconstructed time of each pulse is the interpolated timing of the half-height of the leading edge shown in Figure [7.2](#).

The reconstructed hit time is the rise-up time of the first pulse detected in a segment. The beginning time of a cluster is the time of the hit with most scintillation light.

**7.2.2 Timing Offset in Each Segment.** The natural differences in PMT signal transportation causes various time offsets between channels. The event timing

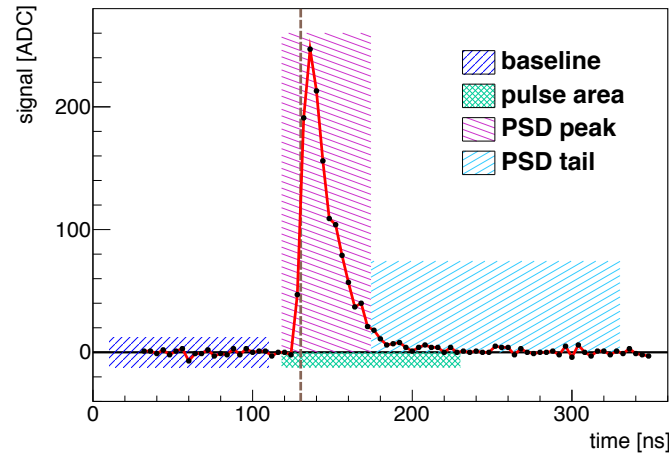


Figure 7.2. An example pulse of PROSPECT. The rise-up timing of a pulse is defined as the time of the half-height leading edge of the pulse.

difference observed by two PMTs of each segment needs to be corrected based on the measurement of time offsets. Cosmic muon tracks are used to measure the time offset of each segment. Through-going muons produce multiple time correlated pulses among PMTs at various distances from the origin of scintillation light. Because the PROSPECT AD is particle track sensitive, the muon tracks can be selected by cuts requiring multiple segment hits ( $\geq 4$  segments and within  $0.4 \times$  segment width difference) with specific PSD value and high energy deposition requirements. Upon the selection of a narrow track of single muon cluster, the segment “corner-clipping” hits are tagged within the detector dynamic range of light collection. The corner-clipping hits are muon energy depositions constrained in a small range to reject additional particle interactions. The time difference  $\Delta t$  of corner-clipping muon hits are calculated. The  $\Delta t$  distribution offset from  $\Delta t = 0$  is the time offset between the two PMTs in each segment. The time offsets in all detector segments are shown in Figure [7.3](#).

The OCS calibration is also used to demonstrate the time offset measured by the segment corner-clipping muon  $\Delta t$  distribution, since all OCS light sources are ideally deployed at the center of each strung PLA rods. With both muon and OCS

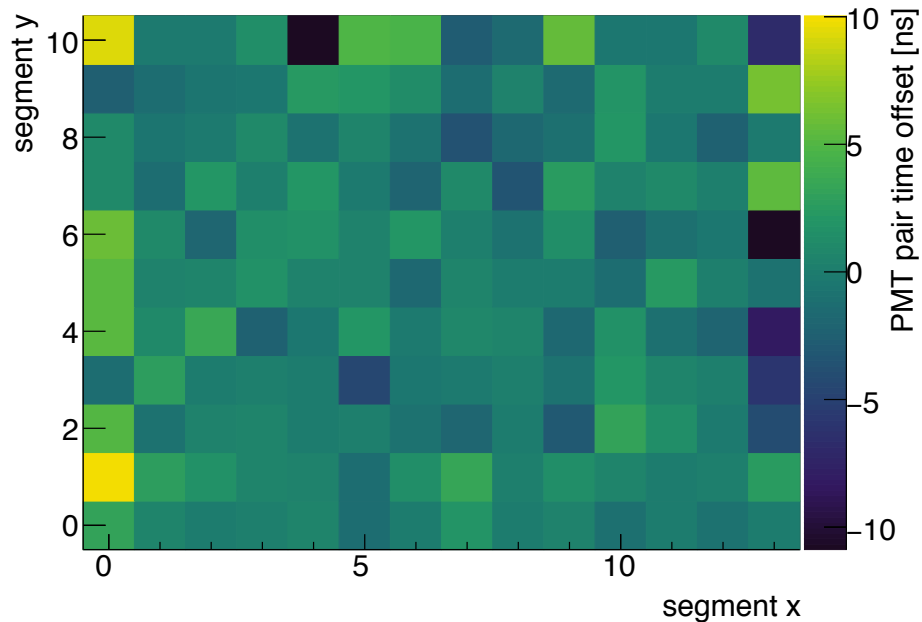


Figure 7.3. The time offset  $\Delta t$  correction of all detector. The Hamamatsu PMTs indicate smaller time differences than the ET PMTs.

timing difference analysis, the run-to-run variation of time offset is  $\sim 50$  ps.

### 7.3 Position Calibration

In Chapter 4, the horizontal and vertical segment locations were defined as  $(x, y)$  positions of the reconstructed events. For the baseline-dependent IBD measurement, the distance between the HFIR core and each segment can be converted from the  $(x, y, z)$  position of segment hits. The  $(x, y, z)$  positions of hits are also used to select correlated events with respect to their distance.

The time difference between the PMTs of each segment is used to reconstruct a hit's position along the  $z$ -axis. The PLA rod tabs, because of their precise widths and distances, make each PLA rod's axis good position calibration “ruler”. By identifying light collection bands of the corner-clipping muon hits from muon tracks, the “Hobbes effect” of muon energy deposition changed by the PLA tabs makes nonuniform event  $dt$  distribution, as shown in Figure 7.4.

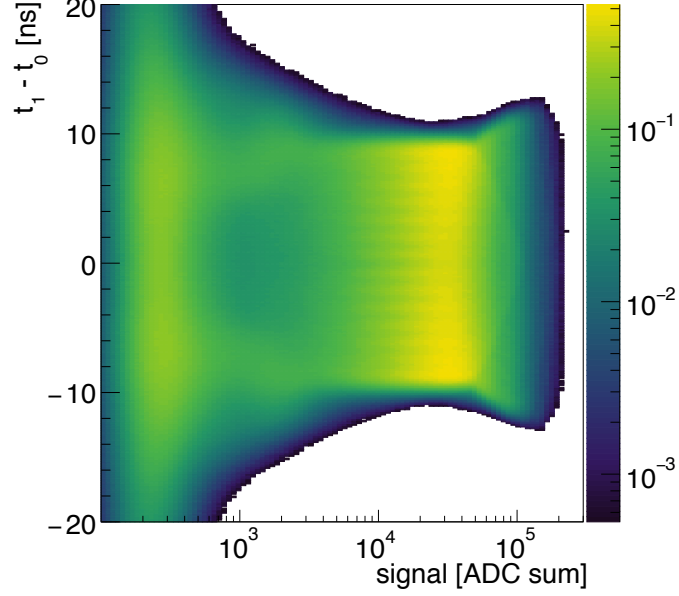


Figure 7.4. The “Hobbes effect” corner clipping muons travel through different sections of a segment, where the  $dt$  distribution varies with the existence of the PLA rods.

The  $dt$  distribution is fitted with a composite function shown in Figure [7.5](#).

$$f(dt) = M(dt) \left[ 1 + k \cos\left(\frac{2\pi}{\delta}(adt + bdt^3)\right) \right], \quad (7.1)$$

where  $M(dt)$  is a “M” shaped function, the fine structure contains the average  $\delta = 78.5$  mm spacing between pinwheel tabs, and  $k, a, b$  are fitting parameters. Therefore, a  $dt$  dependent  $z(dt)$  reconstruction is expressed as

$$z(dt) = a dt + b dt^3. \quad (7.2)$$

Scanning through the segments with calibration sources deployed at different  $z$  position can also be used to calibrate the position reconstruction. The result of scanning all segments with  $^{137}\text{Cs}$  single gammas demonstrated the effectiveness this strategy.

#### 7.4 ADC to Energy conversion

Because the trigger and ZLE thresholds are higher than the SPE signal light collection, PROSPECT converts ADC integrals directly to reconstructed energy. The

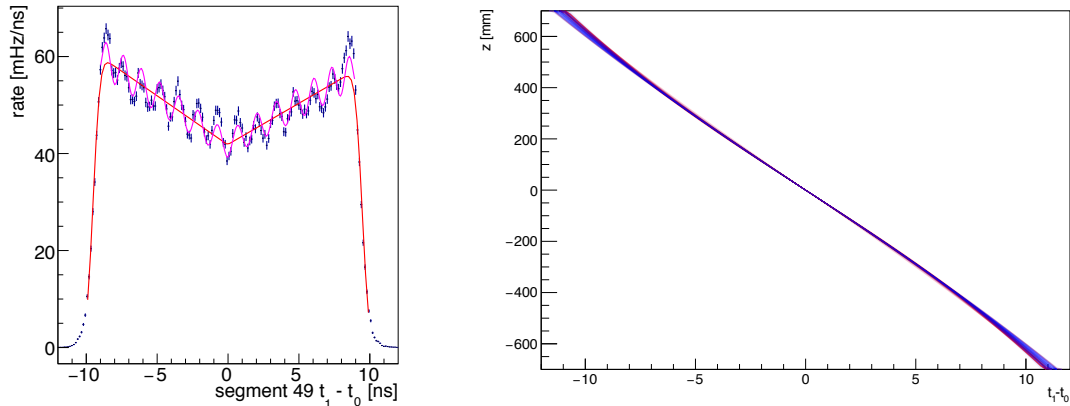


Figure 7.5. (Left) The fitted function of the  $dt$  distribution. (Right) The  $z(dt)$  functions of all segments, where blue (red) represents segments with Hamamatsu (ET) PMTs.

calibration energy utilized for the ADC to energy conversion is the total visible energy of the  $n$ -Li capture events. An advantage of calibrating the energy with  $n$ -Li events is their localized PSD and energy range. The  $n$ -Li captures are selected based on time coincidence between proton recoils caused by fast cosmogenic neutrons and delayed hits in the PSD and energy range of  $n$ -Li captures. Besides, muons and cosmogenic neutrons are constantly detected in the PROSPECT AD. Passive energy calibration can be performed to ensure energy scale stability through the data acquisition period. The total energy of a  $n$ -Li produced alpha particle and Triton is 4.78 MeV, which is severely quenched due to the particles' high  $dE/dx$  rate. The accurate quenched energy of  $n$ -Li capture event is unknown. The initial ADC to energy conversion is hence based on an assumed energy of 0.55 MeV. Further correction is made later as the absolute energy scale is calibrated separately through gamma sources and cosmogenic  $^{12}\text{B}$  calibrations.

The light collection of PMT channels decreases with increasing distance from the source of scintillation light. This effect is due to the light attenuation and leakage when traveling through the scintillator in each segment. To quantify the attenuation and correct the light collection of events with dependence on  $z$  positions, two variables

of a segment's light collection are defined as

$$R(dt) = \frac{S_1}{S_0}; \quad S(dt) = \sqrt{S_1 S_0}, \quad (7.3)$$

where  $S_1$  and  $S_0$  are ADC integrals of two PMTs. A relative light transport efficiency from a source to each PMT channels is defined as

$$\eta_0(dt) = \frac{S(dt)\sqrt{R(dt)}}{S(0)\sqrt{R(0)}}; \quad \eta_1(dt) = \frac{S(dt)\sqrt{R(0)}}{S(0)\sqrt{R(dt)}}, \quad (7.4)$$

where  $dt = 0$  is defined as the time difference of a light source at the segment center. The fitted light transport efficiency curve of all segments in the early data acquisition time period is shown in Figure 7.6.

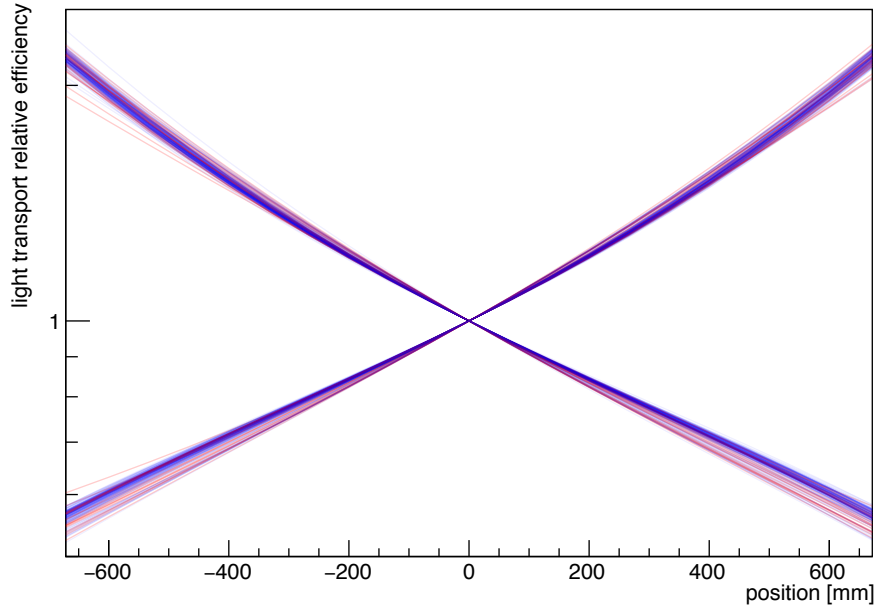


Figure 7.6. The light transport efficiency curve of all segments in log scale, where blue (red) curve represents Hamamatsu (ET) PMTs. The curves show little deviations from exponential function.

The  $\ln(S_1/S_0)$  of each segment was found varying linearly with respect to  $dt$ , as shown in Figure 7.7. The geometric mean is calculated with respect to  $dt$ , as shown in Figure 7.8. The non-uniform ADC integral is corrected with the ADC to energy

conversion factors

$$g_0 = \frac{S}{\sqrt{R}E_n}; \quad g_1 = \frac{S\sqrt{R}}{E_n}, \quad (7.5)$$

where  $E_n$  is the presumed  $n$ -Li visible energy. These factors are unique for each channel at different times, ensuring consistent energy scale at all positions and times in the PROSPECT AD. However, because of the inevitable variation of photo statistics at different location, the resolution of reconstructed energy needs further correction.

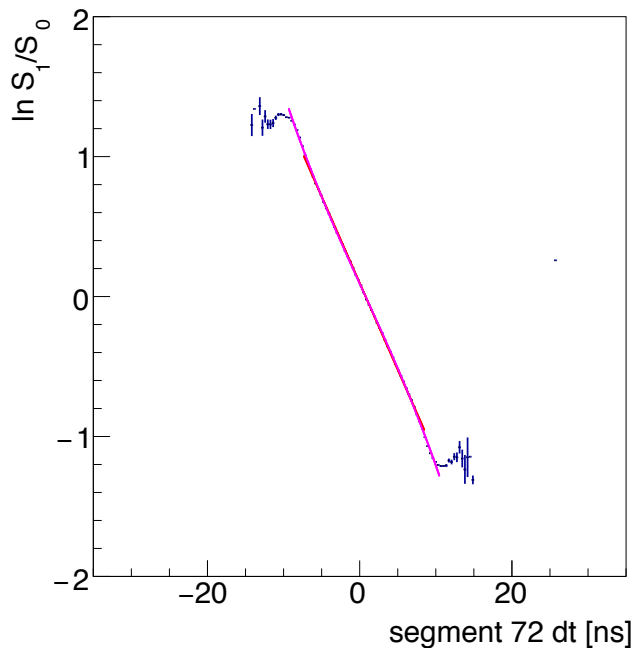


Figure 7.7. The  $\ln(S_1/S_0)$  varies with respect to  $dt$  of a randomly selected segment, where the red line is a linear fit; the pink line is the cubic polynomial used in this analysis.

The SPE conversion between ADC and PE number was studied with OCS calibrations when the gain of each channel was set higher than the regular data taking configuration to cover single PE energy range. By comparing the average ADC integrals of single PE and  $n$ -Li total energy, an MeV/PE photostatistic conversion can be made as shown in Figure 7.9. This photostatistical conversion is used to quantify the effective PE amount of data acquisition runs with regular gain setting, and monitor the stability of energy resolution.

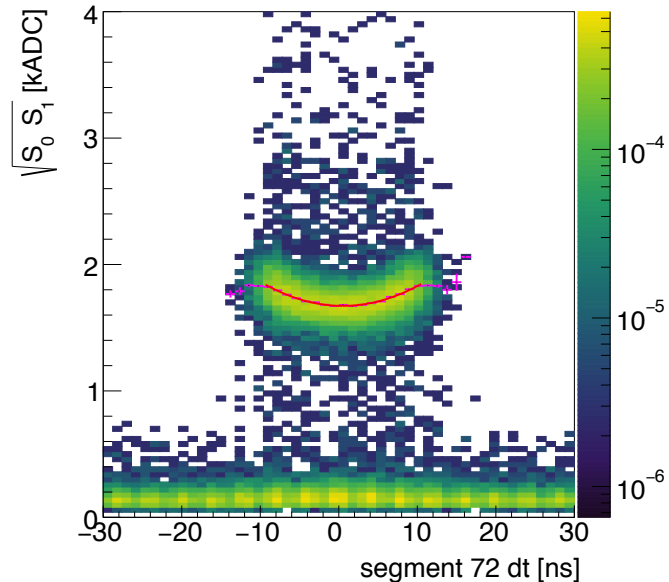


Figure 7.8. The geometric mean of  $n$ -Li events are saved for each event with dependence on  $dt$ . The total collected signal at the center of a segment is the minimum.

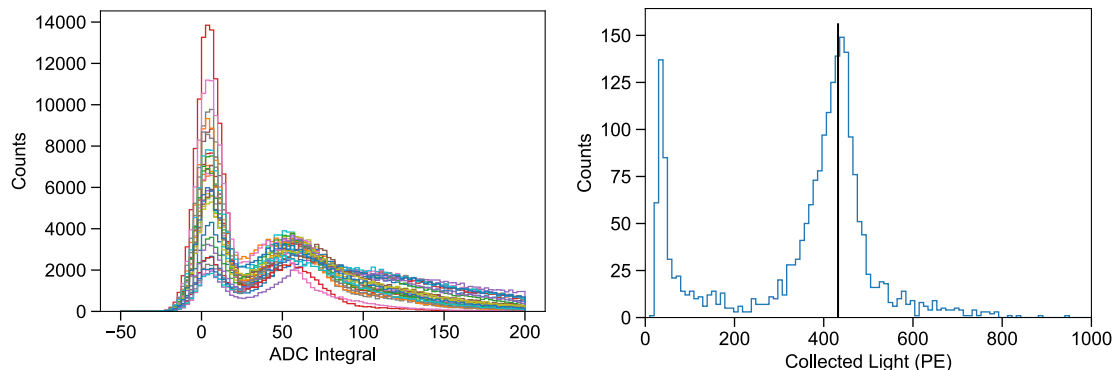


Figure 7.9. (Left) The distribution of ADC integrals of single and double PE. (Right) The distribution of PE amounts of  $n$ -Li capture with presumed 0.55 MeV, suggesting  $\sim 790$  PE/MeV photostatistics.

## 7.5 PSD Calibration

Because of the non-uniform light collection along the  $z$ -direction, PSD values of events at different position are inconsistent. Correction of PSD values with respect to  $\Delta t$  is made with a simplified function

$$n(dt) = g + d \exp k\Delta t, \quad (7.6)$$

where  $g$ ,  $d$  and  $k$  position correction and scale factors. This function has been demonstrated in the PSD stability tracking.

## CHAPTER 8

### ABSOLUTE ENERGY SCALE CALIBRATION

The reactor neutrino spectrum measurement of PROSPECT relies on correct reconstruction of IBD prompt positron energy of IBD events. The absolute energy scale ought to be precisely calibrated for this physics goal.

The reconstructed energy with the PROSPECT AD is naturally different from the energy deposited by particles because of energy loss, light leakage, imperfection of detector components, and nonlinear effects. Most of these effects are simulated with PG4. It is vital to characterize the detector response with correctly simulated detector structure, nonlinearity of energy response and energy resolution to

- Supply an accurate nonlinear detector response model to the MC.
- Quantify the systematic uncertainty in energy response.

In the absolute energy scale calibration, gamma sources, neutron sources calibration and ambient data calibration were used to characterize the absolute detector response, including nonlinearity contributed by the Birks' law quenching and Cherenkov radiation of scintillator, and absolute energy scale adjustments necessitated by the low level calibration presumption of  $n$ -Li visible energy (described in Chapter [7](#)). The corrected  $n$ -Li visible energy was re-calibrated based on the adjustment, while the stability of event reconstruction were also validated.

In addition, necessary detector geometry corrections were implemented, respect to physical measurements on detector material and dimensions to enhance data-MC agreement in gamma collection. At last, the combined fit of all calibration data to PG4's MC simulation was made to constrain the energy resolution and

nonlinearity model. This model, along with reactor neutrino production models, is used to produce a predicted IBD prompt energy spectrum from HFIR.

This energy scale was thoroughly studied in this thesis research, as it is vital for PROSPECT's neutrino spectrum reconstruction. In this study, the PG4 feature simulating nonlinearity effects is a new method for energy scale calibration in a segmented detector. I led this essential calibration work for the experiment to ensure a precise modeling of the PROSPECT's reactor neutrino spectrum.

### 8.1 Energy Scale Calibrations Activities

Three calibration campaigns were organized in 2018 to characterize the detector energy response. The sources used in each campaign are listed in Table 8.1. Each radioactive source is sealed in an aluminum capsule, then inserted through a PTFE calibration tube by a timing belt and deployed at the center of the PLA rods along  $z$ -axis. The positions of PLA rods where energy calibration sources were deployed are shown in Figure 8.1. Once in position, each gamma calibration run lasted for 10 minutes. Most of the  $^{252}\text{Cf}$  and AmBe neutron calibration run lasted for more than one hour because of lower activity in these sources. Several hours of background data were taken within 24 hours of each calibration activity, when the PROSPECT AD ran with identical gain setting with the corresponding calibration run and without deployments of calibration sources. All calibration campaigns were conducted during reactor-off period to avoid reactor correlated gammas and neutrons.

During data acquisition, the trigger threshold of each individual PMT channel, referred to as the ZLE thresholds, were set to reduce the electronic noise and low energy backgrounds in collected by each PMT. The ZLE threshold is a pulse height threshold that requires signal pulses read by PMTs to exceed a specific pulse height. Only the pulses whose height is above the ZLE threshold are recorded in the DAQ

Table 8.1. Calibration source utilized

Source	Decay Type	Energy[MeV]	Time in 2018
$^{137}\text{Cs}$	$\beta^-$	0.662 (de-excitation $\gamma$ )	Apr, Aug, Dec
$^{22}\text{Na}$	$\beta^+$	1.274 (de-excitation $\gamma$ ) + $2 \times 0.511$ (annihilation $\gamma$ )	Apr, Aug, Dec
$^{60}\text{Co}$	$\beta^-$	1.17 + 1.33 de-excitation $\gamma$	Apr, Aug, Dec
$^{252}\text{Cf}$	SF	2.223 (n-H capture de- excitation $\gamma$ )	May, Aug, Dec
AmBe	$^9\text{Be}(\alpha, n)^{12}\text{C}$	4.4 MeV de-excitation $\gamma$ , $\sim 1$ MeV nucleon recoil	Dec
$^{12}\text{B}$	$\beta^-$	3 MeV to 13.4 MeV	Ambient data

storage. During gamma and neutron calibrations, the ZLE thresholds were 10 and 20 ADC channels respectively, which is equivalent to 40 to 80 keV. The light collection varies throughout the PROSPECT AD because of the non-uniformity of the LS attenuation length and light yield efficiency at different positions in the detector. In addition, PMT gain and scintillation light yield of PROSPECT AD also dependent on time in PROSPECT AD. Thus, the ZLE threshold can induce non-uniform reconstructed energy scale based on the position and time of the incident particle. A 90 keV detector-wide ‘analysis ZLE threshold’ is introduced to exclude segment hits whose reconstructed energies are lower than 90 keV. This analysis ZLE threshold resolves the non-uniformity of lower energy reconstruction that is caused by the time and position dependent event selection efficiency. To unpack and analyze the calibration data, the PROSPECT-2x (P2x) analysis package is used to reconstruct the gamma energy of clusters in the full detector and the Compton scattering energy

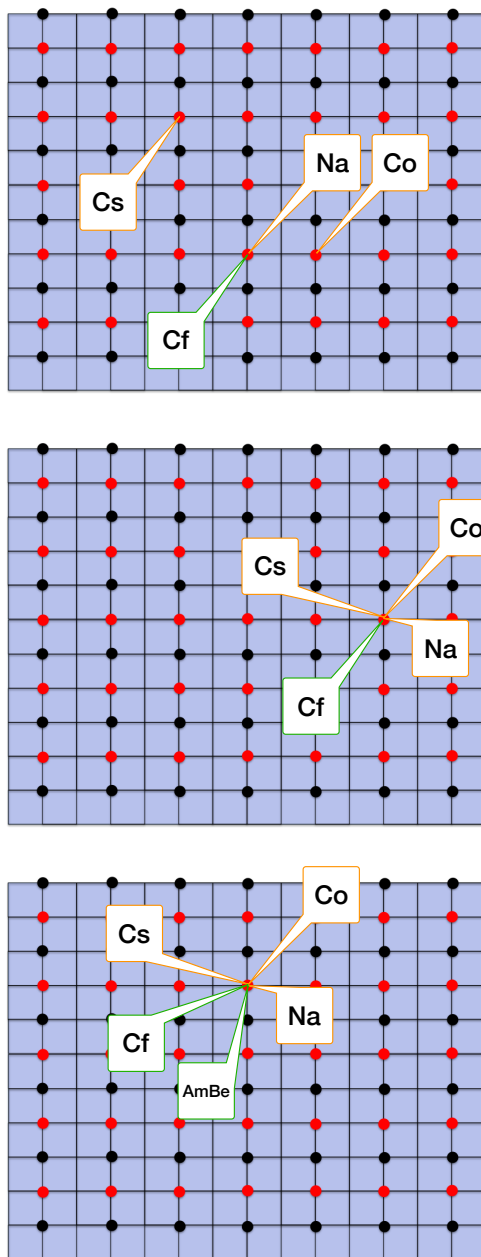


Figure 8.1. Positions of the PLA rods where specific radioactive source was deployed for energy scale calibrations. In this study, each source was deployed at the center of the corresponding PLA rods along  $z$ -axis. (Top) Source locations of 2018 April and May calibrations. (Middle) Source locations of 2018 August calibrations. (Bottom) Source locations of 2018 December calibrations.

deposited in single segments. Once again, the reconstructed energy is the summed energy of all hits in an cluster that passed the analysis ZLE threshold.

The reconstructed energy resolution is highly dependent on the photostatistics of events. Therefore, the energy resolution varies with respect to the non-uniformity of light collection among segments and evolve during the data acquisition period. In data unpacking and analysis, each hit of a cluster is artificially smeared based on the lowest photostatistics dataset in the sample, 325 PE/MeV, as shown in Figure 8.2.

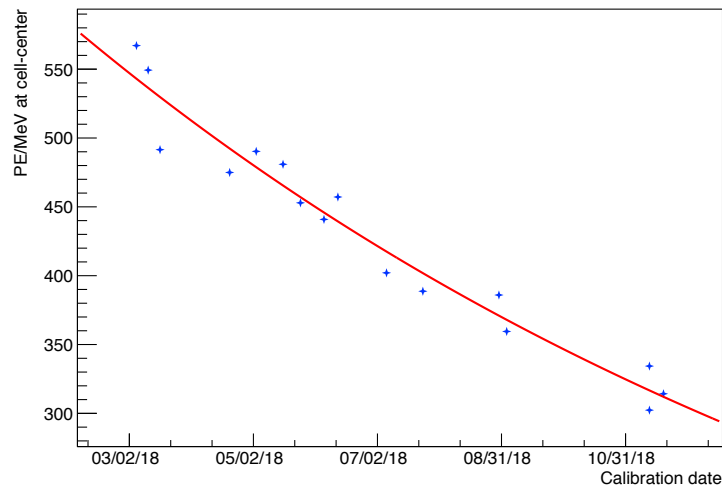


Figure 8.2. PE per MeV tracked through the total data acquisition period. The fitted function suggests  $346 \pm 17$  PE/MeV at the end of the period.

The reconstructed energy of each event is smeared based on the calibrated effective PE/MeV factor characterized with cosmogenic neutrons captured by  ${}^6\text{Li}$  in each run. Every hit is smeared with a factor randomly chosen from a Gaussian distribution, whose standard deviation is defined as

$$\sigma = E \cdot \sqrt{\frac{1}{k} - \frac{1}{n}}, \quad (8.1)$$

where  $k$  is the target PE/MeV factor and  $n$  is the measured PE/MeV factor.

In a summary, an event energy is reconstructed with an additional threshold and randomized resolution correction. The purpose of these two additional adjustments is to eliminate the energy scale and resolution's dependence on events' time

and position.

## 8.2 Calibration Event Reconstruction

For gamma source calibration,  $^{137}\text{Cs}$ ,  $^{22}\text{Na}$  and  $^{60}\text{Co}$  sources were deployed. The gamma-like events are selected within the  $3\sigma$  range of the mean PSD value for gammas and electrons. Background events were analyzed with the background data described in Section [8.1](#). The selection of background events is identical to the selection gamma calibration event.

The time coincidence between prompt and delayed  $\gamma$ -rays is searched to select the  $n$ -H capture gamma energy. The prompt  $\gamma$ -rays (3 MeV to 15 MeV) are emitted from the  $^{252}\text{Cf}$  fission reaction, while the delayed  $\gamma$  ray is the 2.22 MeV de-excitation  $\gamma$  from the  $n$ -H capture interaction. Using PSD distribution bands,  $\gamma$ -ray-like events within 0 to 200  $\mu\text{s}$  after the prompt  $\gamma$  signal were tagged as  $^{252}\text{Cf}$  correlated  $\gamma$  events, while the events -1200 to -200  $\mu\text{s}$  before prompt  $\gamma$  are accidental. The  $n$ -H  $\gamma$  spectrum is measured by subtracting the correlated events in background data. The calibration spectra is shown in Figure [8.3](#).

The number of gammas generated by the decay of each calibration source, as well as the energy of each produced gamma ray are different. As a result, different gamma calibration source generate  $\gamma$ -rays that deposit energy in different number of segments. The number of segments hit by a cluster (multiplicity) in the full PROSPECT detector is a critical variable that affects the reconstructed energy, because of its correlation with the energy loss caused by the dead volume and segment a particle traveled through. The multiplicity of the calibration gamma rays are shown in Figure [8.4](#). The correlation between a cluster's multiplicity and energy is detailed in Section [8.4](#).

The  $^{12}\text{B}$  are mainly produced by cosmogenic neutrons with  $^{12}\text{C}(n, p)^{12}\text{B}$  inter-

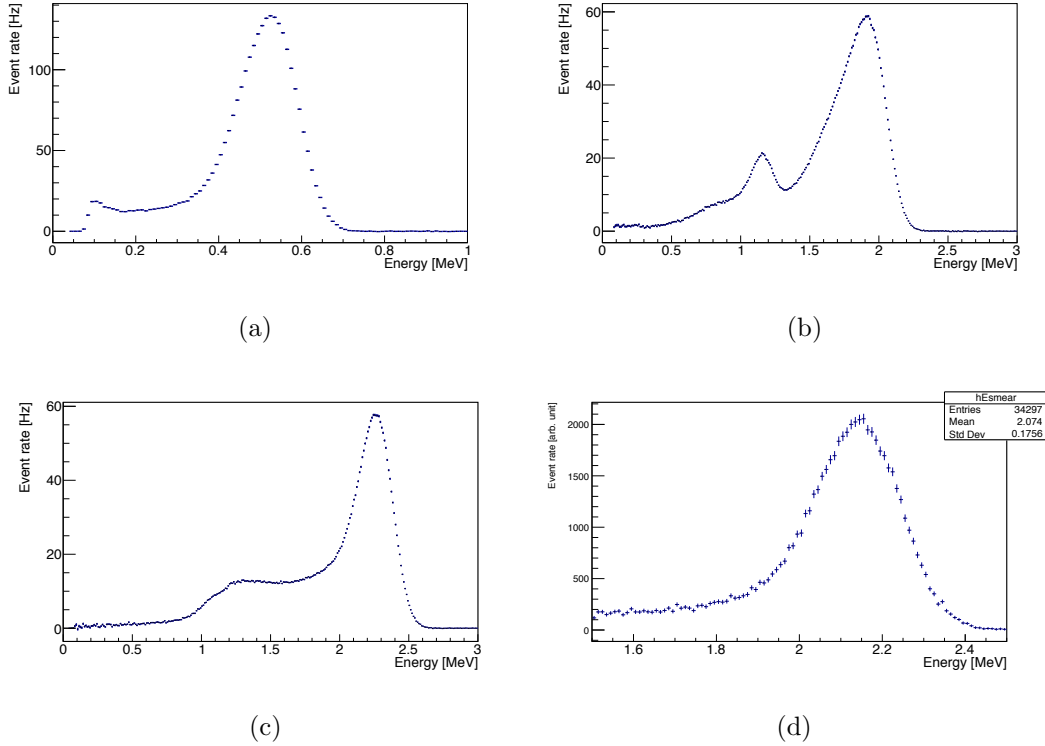


Figure 8.3. The gamma spectra reconstructed with the full PROSPECT AD from calibration sources: (a)  $^{137}\text{Cs}$ , (b)  $^{22}\text{Na}$ , (c)  $^{60}\text{Co}$ , (d)  $n$ -H capture gamma from  $^{252}\text{Cf}$ .

actions, whose cross-section is  $\sim 0.01$  barn. Because the  $\beta$  energy distribution covers a similar range as the IBD prompt energy,  $^{12}\text{B}$  is a valuable calibration source to characterize the reconstructed energy scale for an IBD prompt event's energy. To select  $^{12}\text{B}$  events in PROSPECT, the time coincidence between a prompt neutron recoil signal and a delayed  $\beta$  signal. The prompt and delayed signal are also required to be adjacent. A prompt signal is a single-segment hit with neutron-like PSD in the energy ranging from  $0.7 \text{ MeV}_{ee}$  to  $10 \text{ MeV}_{ee}$ . A delayed signal has gamma-like PSD with energy less than  $15 \text{ MeV}$  and multiplicity  $< 3$ . The  $\Delta t$  between the prompt recoil and the delayed electron events is the range of  $(3, 30)$  ms to exclude neutron capture events. All delayed events are required to be  $< 12 \text{ cm}$  from the prompt events. The lifetime of  $^{12}\text{B}$  was measured as  $28.8 \pm 0.6 \text{ ms}$ , agreed with the nominal  $29.14 \text{ ms}$  lifetime recorded in the ENSDF database, as shown in Figure 8.5. The prompt to delay

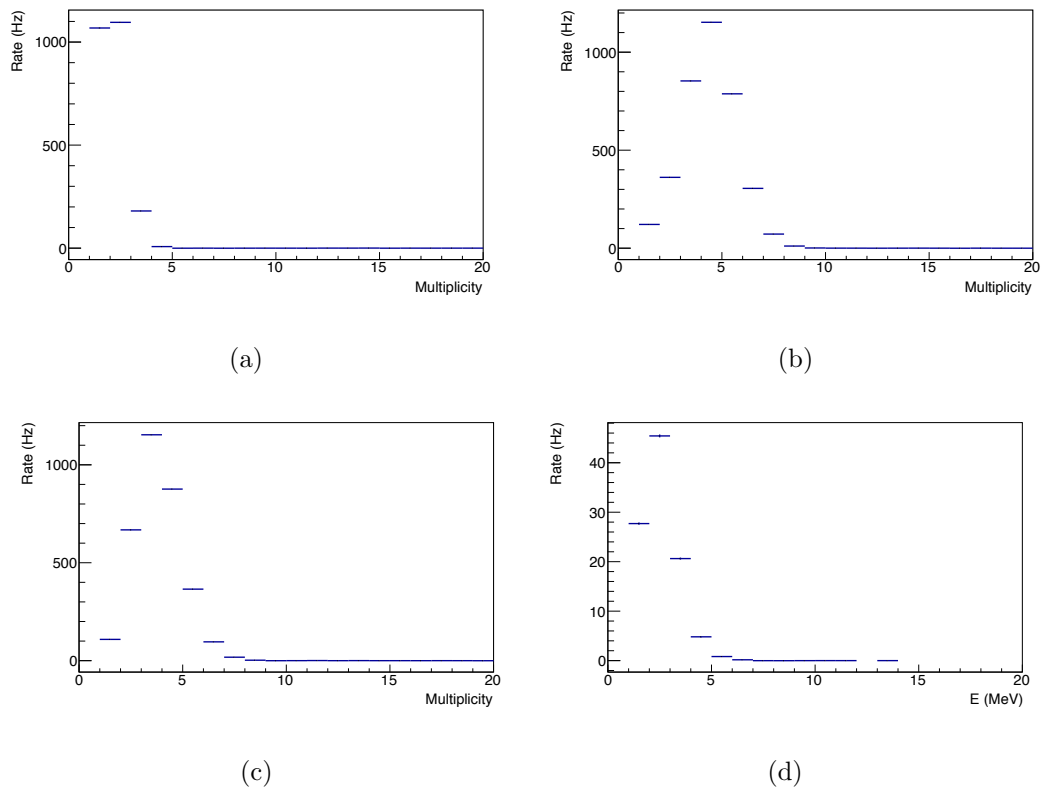


Figure 8.4. The segment hit multiplicity of gamma clusters from calibration sources: (a)  $^{137}\text{Cs}$ , (b)  $^{22}\text{Na}$ , (c)  $^{60}\text{Co}$ , (d)  $n$ -H capture gamma from  $^{252}\text{Cf}$ .

distance is fitted with a Gaussian function whose the best fit standard deviation  $\sigma_d = 2.91$  cm. The value of prompt and delay proximity cut,  $\Delta z < 12$  cm, is set to minimize time variation of event selection efficiency, because the position resolution of the detector evolves with time. In 73 days reactor off data acquisition, there are  $\sim 35300$   $^{12}\text{B}$  beta counted in PROSPECT AD with S:B=0.87. The reconstructed spectrum of  $^{12}\text{B}$  electrons is shown in Figure [8.5](#). Because of the short traveling distance of MeV-scale betas,  $^{12}\text{B}$  events are dominated by beta particles with multiplicities equal to one.

The AmBe calibration source is a composite neutron source, where the  $\alpha$  emitted from  $^{241}\text{Am}$  interacts with  $^9\text{Be}$  through



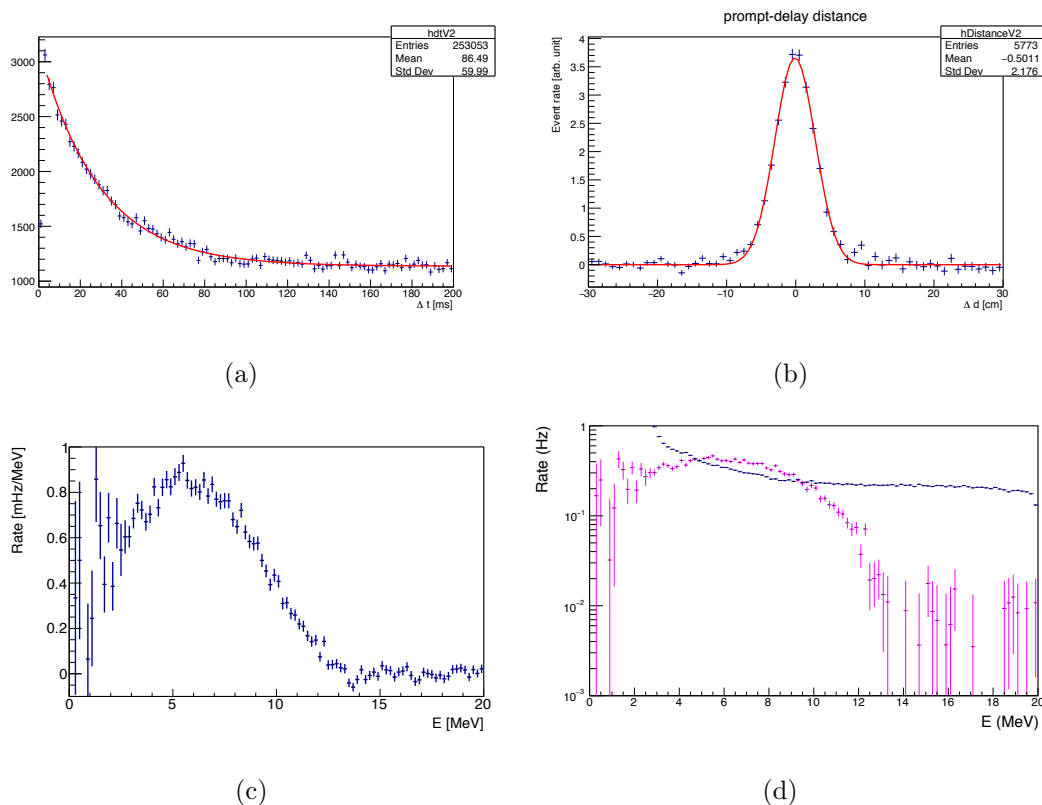


Figure 8.5. The observed of  $^{12}\text{B}$  spectrum in PROSPECT. (a) The delay-prompt time difference of  $^{12}\text{B}$  candidates (b)The delay-prompt distance of  $^{12}\text{B}$  candidates. (c) The reconstructed  $^{12}\text{B}$  spectrum. (d) The  $^{12}\text{B}$  signal spectrum (pink) compared to the background spectrum (blue).

with a 4.4 MeV single energy gamma emission. Although the AmBe calibration data was not included in the data of PROSPECT's neutrino spectrum measurement, the 4.4 MeV gamma is a good cross check for PROSPECT to show its capability to reconstruct particles in the 4 MeV to 6 MeV energy range, where the IBD prompt spectrum distortion was found. The single energy gamma is selected based on the time coincidence between the gamma-like prompt signal and the delayed  $n$ -Li capture signal using the discrimination with PSD. A challenge in the AmBe event selection is that the neutron produced from  $\alpha$ -Be collision has a 1 MeV scale kinetic energy, causing non-negligible signal mixing of the gamma and proton recoil in the prompt event cluster. Therefore, the exclusion of proton recoil from the prompt cluster is

necessary to purify reconstructed spectrum of the prompt 4.4 MeV gamma. The energy spectrum of the AmBe gamma is shown in Figure [8.6](#).

### 8.3 Monte-Carlo Simulation of Calibrations

The purpose of comparing calibration data to MC simulation is to characterize the detector energy response and produce PROSPECT's expected IBD spectrum. The difference between the deposited energy and the reconstructed energy is the result of multiple physical effects in the PROSPECT AD. The Birks' quenching effect and the Cherenkov radiation can cause nonlinear energy reconstruction. Dead volume in the detector contributed by the optical grid also affects the reconstructed energy with gamma leakage and energy loss. In addition, there are relative energy scale differences among segments that are caused by non-uniformity of LS and segment volume. The resolution of reconstructed energy is dominated by the photostatistics of LS. To eliminate the time dependence of the energy resolution, both data and MC events' energies are smeared with respect to the poorest energy resolution (lowest PE/MeV) found during the production data and throughout the detector.

In PG4 simulation, the Birk's constant,  $k_{B1}$  and  $k_{B2}$ , the detection efficiency of Cherenkov light  $k_C$ , and a absolute energy scale  $A$  are the terms used to quantify the energy nonlinearity model and the energy scale. The MC reconstructed energy is

$$E_{MC} = \sum_i^{steps} A(E_{quench,i}(k_{B1}, k_{B2}) + E_{Ckov,i}(k_c)), \quad (8.3)$$

where  $E_{quench,i}(k_{B1}, k_{B2})$  is the effective quenched energy whose magnitude is determined by the Birks' constants, and  $E_{Ckov,i}(k_c)$  is the effective Cherenkov radiation's contribution to the reconstructed energy.

The nonlinearity caused by the ZLE threshold, detector geometry, and other effects are also described in this section.

**8.3.1 Nonlinearity Factors.** The nonlinear energy response of  ${}^6\text{LiLS}$  is mainly

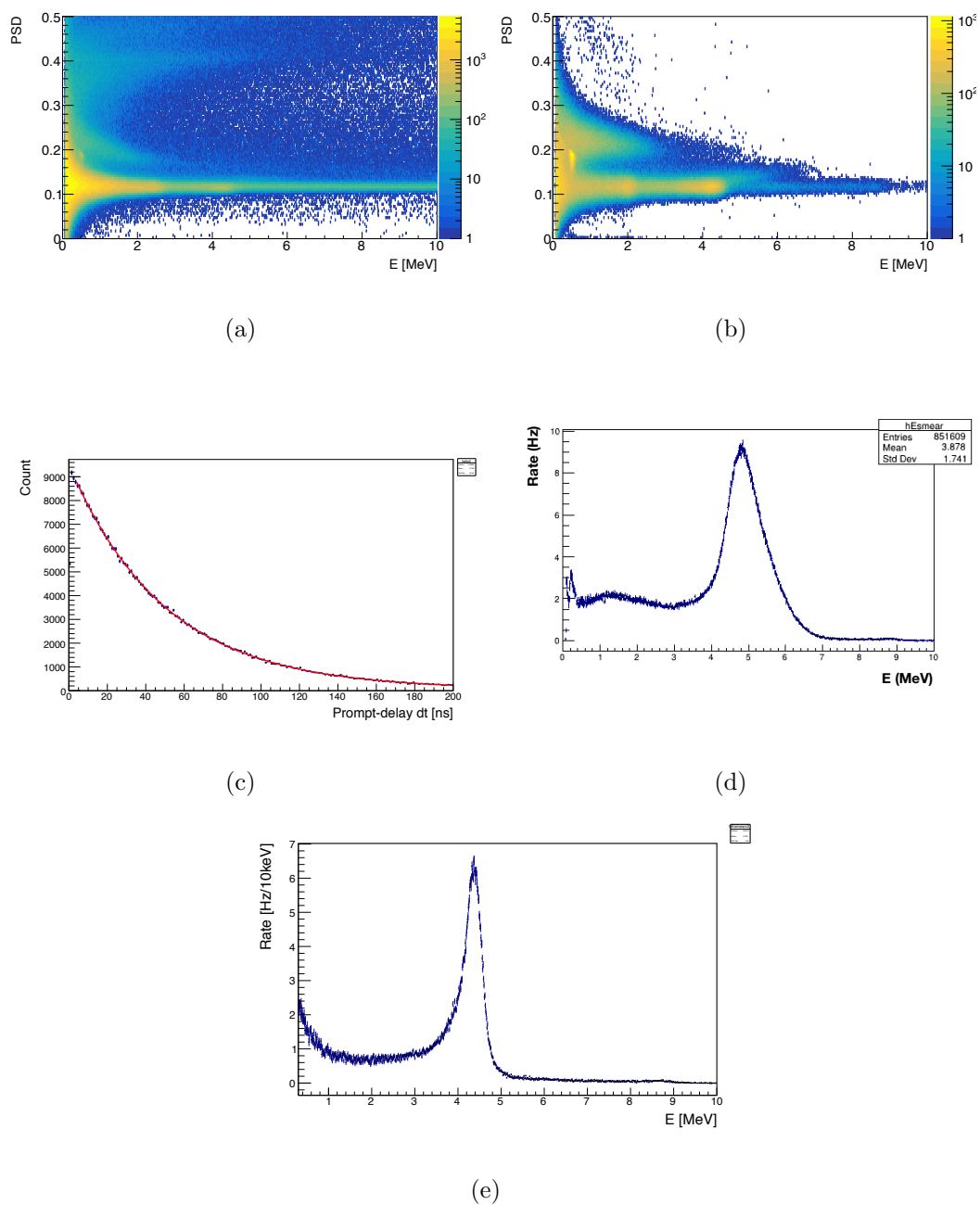


Figure 8.6. (a) and (b) The PSD distribution of all hits detected in the AmBe calibration and simulation, where the gamma PSD distribution is distorted because of the mixing of gamma and prompt proton recoil from the  $\text{Be}(\alpha, n)\text{C}$  interaction. (c) The best fit neutron life time of be AmBe data equals to 49.7 ns. (d) The reconstructed energy of the AmBe prompt events without the exclusion of prompt recoil-like hits. (e) The reconstructed energy of the AmBe gamma after strict exclusion of prompt recoil-like hits.

the result of the Birks' quenching and Cherenkov radiation. The Birks' quenching constants  $k_{B1}$  and  $k_{B2}$  are user defined parameters to model the unique quenching effect for PROSPECT. In Eq. 6.1 and 6.3 in Chapter 6, PG4 simulates the quenching effect by multiplying the energy difference in between `G4Steps` with a Birks' factor:

$$E_{quench} = \sum_i^{steps} \frac{\frac{dE_i}{dx}}{1 + k_{B1} \frac{dE_i}{dx} + k_{B2} \left(\frac{dE_i}{dx}\right)^2}. \quad (8.4)$$

The nonzero value of  $k_{B1}$  reduces the reconstructed energy of lower energy events, as illustrated in Figure 8.7. Although  $k_{B2}$ 's effect is negligible in higher energy, it is capable of affecting particle segment-hit multiplicity through its ability to quench more lower energy events below the 90 keV threshold, as shown in Figure 8.8.

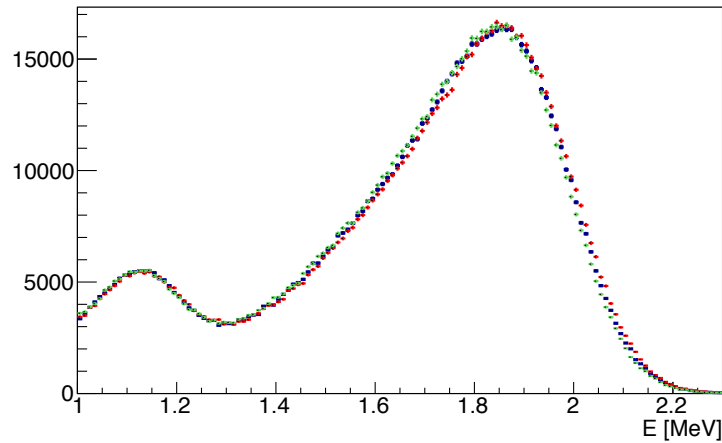


Figure 8.7. The MC quenched energy affected by different  $k_{B1}$  values. (red:  $k_{B2} = 0.124$  mm/MeV, blue:  $k_{B2} = 0.132$  mm/MeV, green:  $k_{B2} = 0.140$  mm/MeV)

According to Chapter 6, the number of photon generated along the particle track is expressed as

$$\frac{d^2 N}{dx d\lambda} = \frac{2\pi\alpha z^2}{\lambda} \left(1 - \frac{1}{\beta^2 n^2(\lambda)}\right), \quad (8.5)$$

where  $N$  is number of photons,  $\alpha$  is the fine structure constant,  $z$  is the particle's electric charge,  $\beta$  is the speed of the particle and  $n(\lambda)$  is index of refraction. Although most Cherenkov light is in the Ultraviolet (UV) wavelength range, the LS is able to absorb and re-emit it to VIS range with currently unknown efficiency. Therefore,

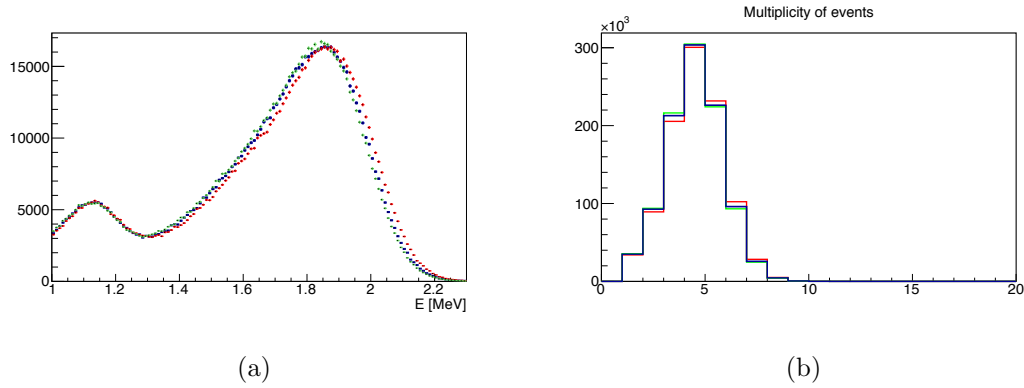


Figure 8.8. The MC quenching induced by  $k_{B2}$ . (a) The energy distribution of  $^{22}\text{Na}$  simulation affected by  $k_{B2}$ . (b) The  $^{22}\text{Na}$  cell-hit multiplicity affected by  $k_{B2}$ . (red:  $k_{B2} = 0.015$  mm/MeV, blue:  $k_{B2} = 0.023$  mm/MeV, green:  $k_{B2} = 0.031$  mm/MeV)

Cherenkov photons can be collected in addition to the scintillation light from high energy incident charged particles and increase reconstructed energy. To simplify the MC simulation, the additional light emitted from the Cherenkov radiation is added to the reconstructed energy as the summed energy of detected Cherenkov photons,

$$E_{ckov} = k_c \sum_{\lambda} N_{\lambda} E_{\lambda}, \quad (8.6)$$

where  $N_{\lambda}$  is number of photons per wavelength calculated by summing the number of Cherenkov photons in all `G4Steps`. The LS's index of refraction and transmission spectrum are assumed to be constant for wavelengths in 200-700 nm range. The effective light collection efficiency of Cherenkov photons,  $k_C$ , can be adjusted to model the effect of Cherenkov radiation on reconstructed energy. The particle energy loss due to Cherenkov radiation is negligible. Figure [8.9](#) shows different  $k_C$  values affecting the n-H capture spectrum.

**8.3.2 Energy Resolution.** The reconstructed energy resolution is a function of energy:

$$\frac{\sigma}{E} = \sqrt{a^2 + \frac{b^2}{E} + \frac{c^2}{E^2}}, \quad (8.7)$$

where  $a$  is affected by the detector geometry,  $b$  is based on the photostatistics (PE/MeV) and  $c$  represents the quantum efficiency of PMTs. This energy dependent resolution

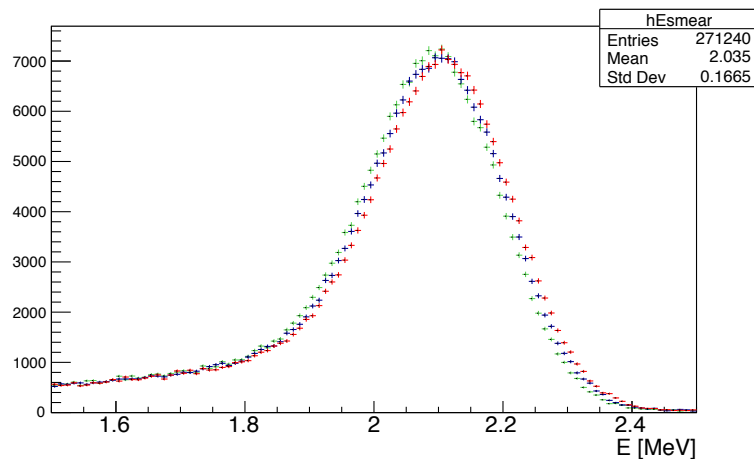


Figure 8.9. The MC Cherenkov radiation effect induced by  $k_C$ . (green:  $k_C = 30\%$ , blue:  $k_C = 35\%$ , red:  $k_C = 40\%$ )

function is widely used in evaluating the LS detectors' energy resolutions. However, the PROSPECT AD's energy resolution is mainly affected by the energy resolution smearing of all hits and the low energy hit exclusion from multi-hit clusters caused by the ZLE threshold. The energy resolution characterized with the gamma calibration sources was not applied to the energy spectrum analysis.

**8.3.3 Other Energy Scale Factors.** The reconstructed energy scale was initially based on the presumption that the reconstructed  $n$ -Li capture energy is 0.55 MeVee in detector. The deviation of the true electron equivalent energy to this estimation can induce a constant energy scale bias throughout the all energy. This absolute energy scale  $A$ , as a fitting parameter, was searched for best fit value simultaneously with other nonlinearity factors. The MINUIT  $\chi^2$  minimization method [91] is used to freely change  $A$  until the  $\chi^2$  between data and MC is minimized.

To ensure precise delta vs. MC comparisons, the ZLE threshold was simulated in the P2x data analysis package by converting the MC energy deposit in MC to pulse with respect to the ADC/PE ratio, as described in Chapter 6. The 90 keV analysis

ZLE threshold is then applied to the calibration MC using same P2x analysis program.

**8.3.4 Detector Geometry Simulation.** The difference between the simulated detector geometry and the PROSPECT AD could lead to a disagreement in energy loss and gamma leakage between MC and data. The reconstructed energy of a multi-hit cluster is affected by the separator thickness, the PLA rods' size, and all dead volume contributing materials in the detector. In this work, PG4's detector structure was simulated with detailed adjustments based on the actual design and measurements of the PROSPECT AD, including the thickness and chemical composition of separators, the PLA rods' dimensions, the structure of calibration system, the density and mixture of the LS and calibration capsule properties. PG4 simulated energy spectra with and without detailed detector structural match are shown in Figure [8.10](#)

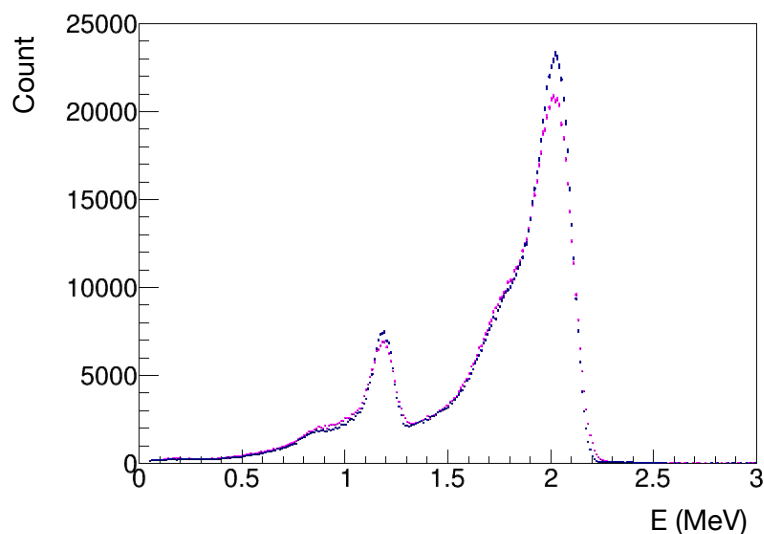


Figure 8.10. An example showing two  $^{22}\text{Na}$  spectra simulated with PG4 with (pink) and without (blue) detailed detector structural match.

Among these detector properties, the thickness of separators plays a non-negligible role in event energy loss. The thickness and uncertainty of the separator is  $1.18 \pm 0.05$  mm, which is described in Reference [80](#).

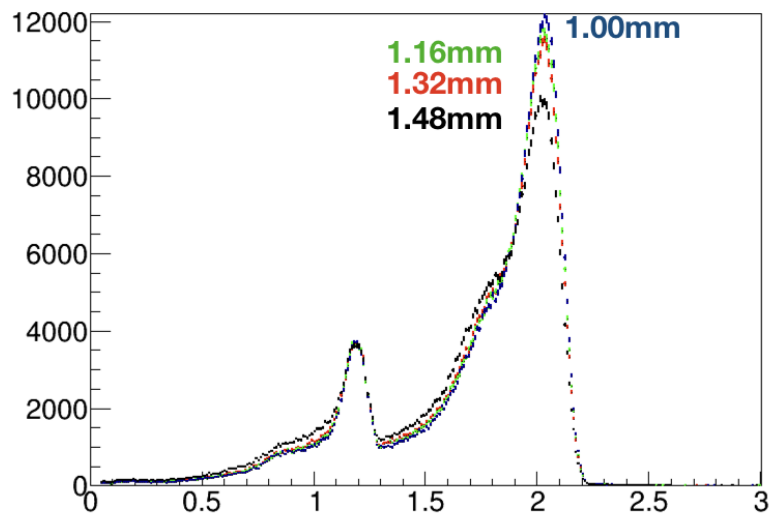


Figure 8.11. An example showing the thickness of separators affecting the energy loss on the spectrum.

The uncertainties of the detector components' dimensions played a negligible role in energy loss. In Figure [8.12](#), with exaggerated variation within 0.25 mm, the PLA rods' wall thickness does not cause visible change to the reconstructed energy scale.

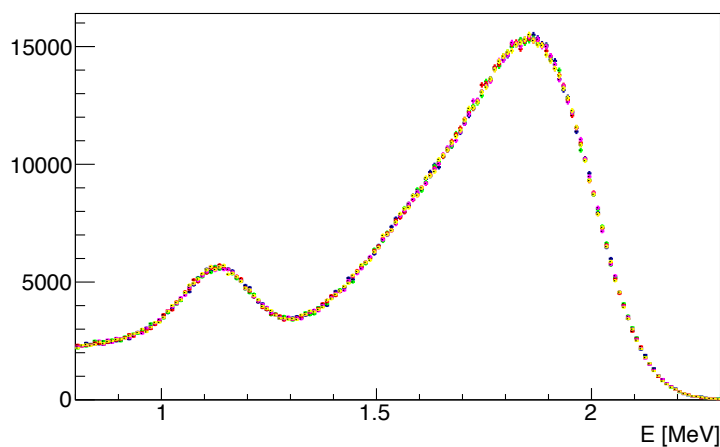


Figure 8.12. A simulated example showing the thickness of PLA rods' negligible effect on the energy loss. (blue: 12.1 mm; red: 12.2 mm; green: 12.3 mm; pink: 12.4 mm; yellow: 12.5 mm)

**8.3.5 Calibration Input Model.** The input model of radioactive calibrations

was based on the decay branchings saved in the ENSDF database. Each gamma calibration was simulated with one million decays for every nonlinearity model generated, which is comparable to the actual count of gammas produced in calibrations. The branching information and energy levels of  $^{12}\text{B}$  decay are extracted from reference [92]. We generated 10 million  $^{12}\text{B}$  decays in simulation, which is considerably more statistics than data collected. During data vs. MC comparison, the  $\sim 1\%$  energy scale uncertainty of the  $^{12}\text{B}$  input spectrum was taken into consideration by pulling in the energy scale of the predicted  $^{12}\text{B}$  spectrum in  $1\%$ . The uncertainty in  $^{12}\text{B}$  decay branching fractions are negligible.

Considering the gamma energy loss by the finite detector volume, the simulated calibration source location is at the same reconstructed source location from actual calibration data.

#### 8.4 Data vs. Monte-Carlo Comparison

The MC energy spectra and gamma multiplicities were compared to calibration data through  $\chi^2$  tests. Calibration runs were simulated with PG4 while a variety of parameters,  $k_{B1}$ ,  $k_{B2}$  and  $k_C$  were float to search for the best fit nonlinearity model, as described in section 8.3.1. The MC files were converted to pulses and processed through a similar analysis loop as the actual calibration data, including the energy-pulse conversion described in Chapter 6. The event based smearing and the analysis ZLE thresholds were also applied. The data vs. MC comparison was made with a similar detector configuration, including the same dead channels, comparable event rate, and same size of fiducial volumes. Then, the analyzed MC calibration spectra were scaled with a constant energy scale  $A$ . Taking both MC's and data's statistical uncertainties into consideration, the  $\chi^2$  of each comparison is expressed as:

$$\chi^2 = \sum_i \frac{(O_i - WE_i)^2}{\sigma_O^2 + W^2\sigma_E^2}, \quad (8.8)$$

where  $O$  and  $E$  represent data and MC respectively,  $W$  is the normalization factor

of MC spectrum or multiplicity, and  $\sigma_O$  and  $\sigma_E$  are the statistical uncertainties of data and MC. To find the best fit detector response model, the combined  $\chi^2$  value is defined as

$$\chi_{data-MC}^2 = \sum_{\gamma} \chi_{\gamma}^2 + \sum_{multi} \chi_{multi}^2 + \chi_{^{12}\text{B}}^2, \quad (8.9)$$

where  $\sum_{\gamma} \chi_{\gamma}^2$  is the summed  $\chi^2$  of gamma energy spectra,  $\sum_{multi} \chi_{multi}^2$  is the summed  $\chi^2$  of gamma multiplicity, and  $\chi_{^{12}\text{B}}^2$  is calculated by data-MC comparison of the  $^{12}\text{B}$  beta spectrum. The MINUIT  $\chi_{data-MC}^2$  minimization method was utilized to find the best fit four parameters.

The  $\chi^2$  value is minimized with data-MC comparison of full-detector reconstructed energy spectra and gamma multiplicity. The best-fit model was then cross-checked with the energy measured with single detector segments that are most adjacent to the calibration sources, which is mostly affected by the LS light yield.

**8.4.1 Full Detector Spectrum Comparison.** The full detector reconstructed energy spectrum is the summed energy a particle cluster. The energy resolution and nonlinearity affected the full detector energy spectrum not only through energy scale, but also through segment-hit multiplicity, for different quenching coefficients can reserve or reject hits through the 90 keV threshold of single cell measured energy.

To simplify the modeling of the detector response, the Birks' constants  $k_{B1}$  and  $k_{B2}$  in Eq. [6.1](#) and the detection efficiency of Cherenkov photons  $k_C$  were adjusted freely to search the best-fit detector response model with the data. Massive calibration simulations were made with 1000 combinations of  $k_{B1}$ ,  $k_{B2}$ , and  $k_C$ . Because of the variety of sources, each combination of parameters requires five simulations with an individual calibration source simulated. The 1000-combination parameter search is limited by computer resources and time available. Therefore, to search for the best fit parameters, four to five levels of narrowing down the range of the covered parameter space is necessary. As a result, searching the best fit parameters with

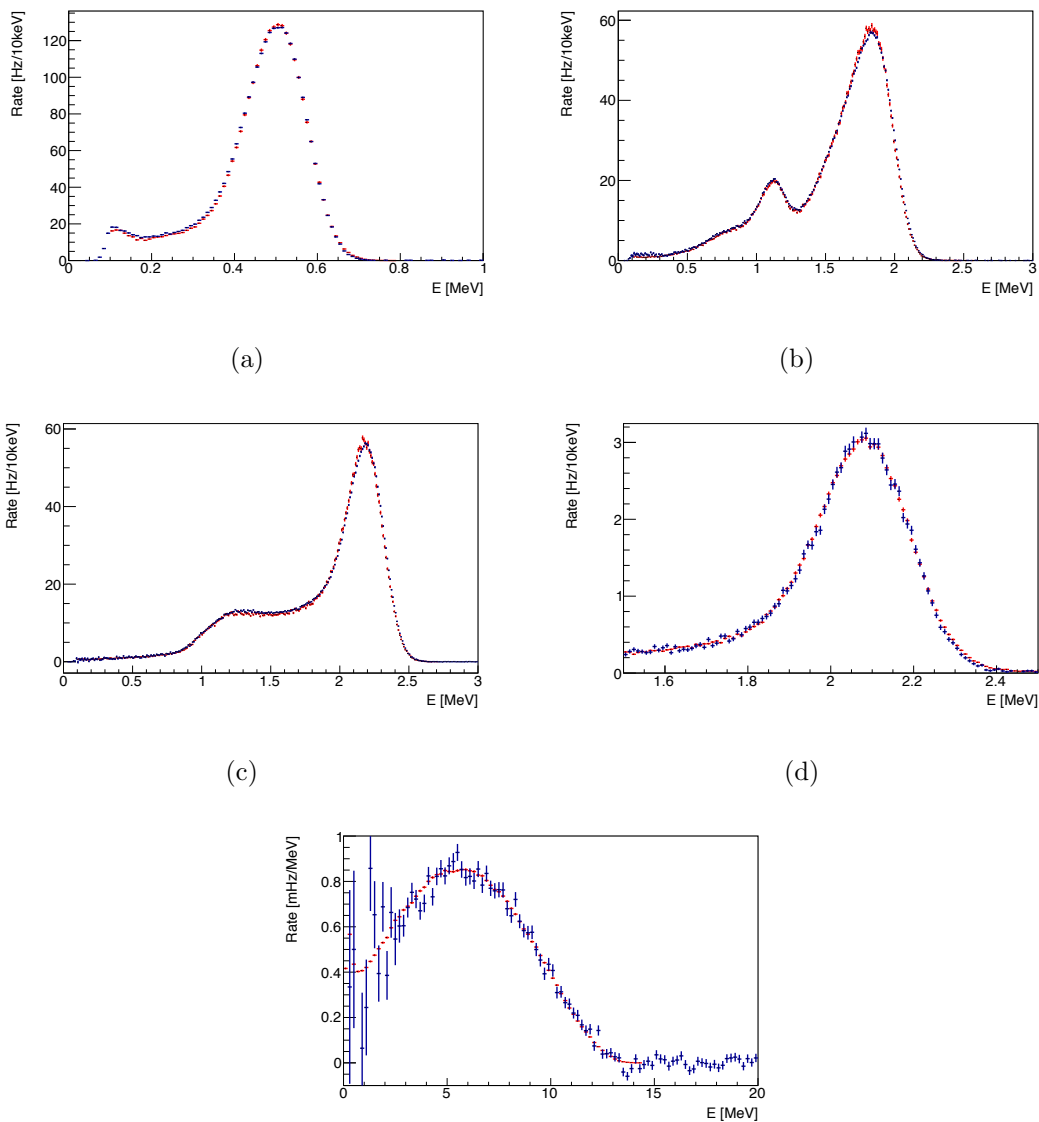
substantial precision took approximately 50000 computer hours. The final parameter search was in the range (0.104, 0.144) mm/MeV for  $k_{B1}$  with 0.004 mm/MeV steps, (0.0011, 0.051) mm/MeV for  $k_{B2}$  with 0.004 mm/MeV steps and (29, 49)% for  $k_C$  with 2% steps.

For the efficiency of massive comparisons, the range of gamma spectrum comparison were defined automatically in software. A custom program was used to search Gaussian-like distributions in the energy spectrum. The range of the fitting is the  $3\sigma$  range of the tagged peaks. In the case of  $^{22}\text{Na}$  calibration, where the distribution contains two peaks, the range is from the lower limit of the lower energy peak and the upper limit of the higher energy peak. For multiplicity, the range of comparison is from 1 to 10. For  $^{12}\text{B}$  comparison, the range of fitting is 3 MeV to 13.5 MeV.

Figure [8.13](#) shows the full detector calibration spectra comparison best-fit model, where  $\chi^2/NDF = 581.5/420$  with the parameters:  $k_{B1} = 0.132 \pm 0.004$  mm/MeV,  $k_{B2} = 0.023 \pm 0.004$  mm/MeV  $k_C = 37 \pm 2\%$ , with an absolute energy scale of  $A = 100.26 \pm 0.46\%$ . There were  $\chi^2/NDF = 205.9/60$  contributed by the multiplicity fitting. The data-MC energy spectra comparison of the best-fit model is shown in Figure [8.13](#), and the multiplicity comparison is shown in Figure [8.14](#).

The  $\chi^2$  distributions dependent on combinations of  $k_{B1}$  and  $k_{B2}$ ,  $k_{B1}$  and  $k_C$ , and  $k_{B2}$  and  $k_C$  are shown in Figure [8.15](#). The nonlinearity parameters shown are correlated. At this current stage, the correlations among the parameters is not studied. As a result, the uncertainty calculated covers all parameter sets in the  $1\text{-}\sigma$  range of each individual parameter.

**8.4.2 Single Cell Spectrum Comparison.** The calibration energy spectra measured by single segments of the PROSPECT AD are independent from the energy loss caused by detector dead volume and the analysis ZLE threshold's low energy hit



(e) Full detector MC-data for  $^{12}\text{B}$  spectrum.

Figure 8.13. The full detector calibration energy spectra data vs. MC. comparison, with statistical errors only. (red: MC, blue: data) (a)  $^{137}\text{Cs}$ , (b)  $^{22}\text{Na}$ , (c)  $^{60}\text{Co}$ , (d)  $n$ -H capture gamma from  $^{252}\text{Cf}$ .

exclusion. The data and MC agreement in single-segment reconstructed energy is a valuable cross-check to the full-detector best fit model. The cross-check is to compare the reconstructed and simulated Compton scattering energy spectrum measured by the single segments that are most adjacent to the calibration sources.

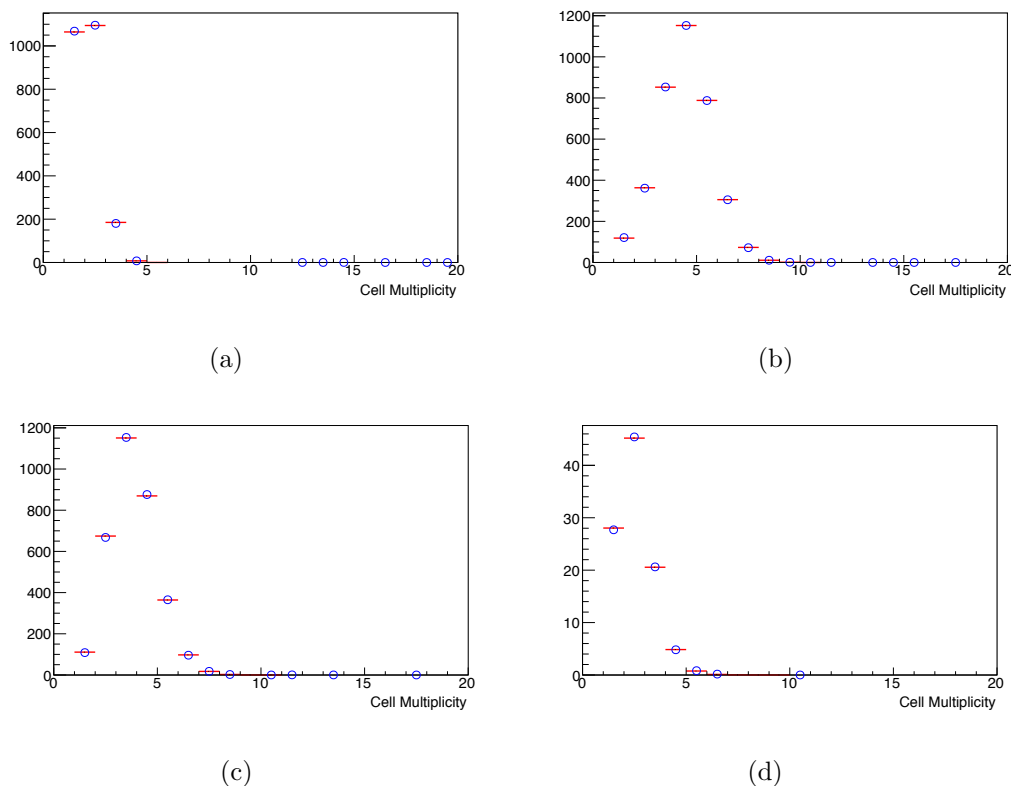


Figure 8.14. Data vs. MC comparisons multiplicity distributions of gamma calibrations. (red: MC, blue: Data) (a)  $^{137}\text{Cs}$ , (b)  $^{22}\text{Na}$ , (c)  $^{60}\text{Co}$ , (d)  $n$ -H capture gamma from  $^{252}\text{Cf}$ .

Each source has four most adjacent segments. To reduce the systematic differences of energy scale between segments, the gamma spectra from four segments were averaged. For gamma radioactive calibrations, the range of fitting is from 0.3 MeV to the ends of the spectra. The range of fitting of the gamma spectrum from  $n$ -H capture was 1.5 MeV to 2.3 MeV. In single cell comparison, we compare only the single hit  $^{12}\text{B}$  electron energy spectrum. The range of fitting for the  $^{12}\text{B}$  spectrum is 3 to 13.5 MeV. To simplify the fitting, the MC spectra were normalized to data based on the spectral integral in the range of interest.  $\chi^2$  comparison of each calibration spectrum was made between data and a best fit MC. Then, the summed  $\chi^2$  of all comparisons was evaluated.

The data vs. MC comparisons with full detector best fits are shown in Figure

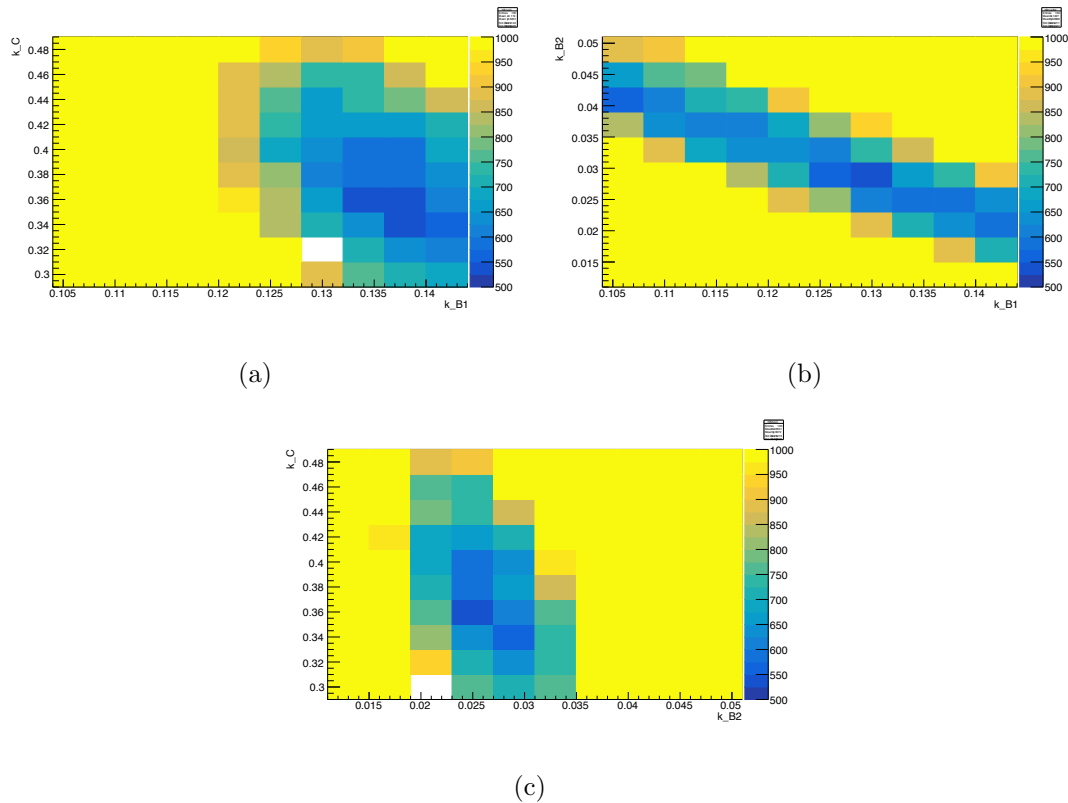


Figure 8.15.  $\chi^2$  distribution with respect to the values of the nonlinearity parameters. (a)  $\chi^2$  distribution dependent on  $k_{B1}$  and  $k_C$ . (b)  $\chi^2$  distribution dependent on  $k_{B1}$  and  $k_{B2}$ . (c)  $\chi^2$  distribution dependent on  $k_{B2}$  and  $k_C$ .

**8.16.** The summed  $\chi^2/NDF = 1003.29/584$  with the parameters of the nonlinearity model obtained in the full-detector fitting in Section **8.4.1**. The average energy shift is  $A = 100.30\%$ . The single segment data vs. MC comparison demonstrated the best fit energy scale factors are compatible with the single LS volume reconstructed Compton scattering energy.

**8.4.3 Agreements Among Different Calibration Campaigns.** The energy scale model discussed in Subsection **8.4.1** was found with combined fitting of gamma calibrations taken in April 2018, neutron calibration performed in May 2018 and  $^{12}\text{B}$  for the first neutrino spectrum analysis. Ideally, this model is expected to be compatible with other calibration campaigns with the same detector and calibration configurations within the energy scale uncertainty. Additional MC vs data compar-

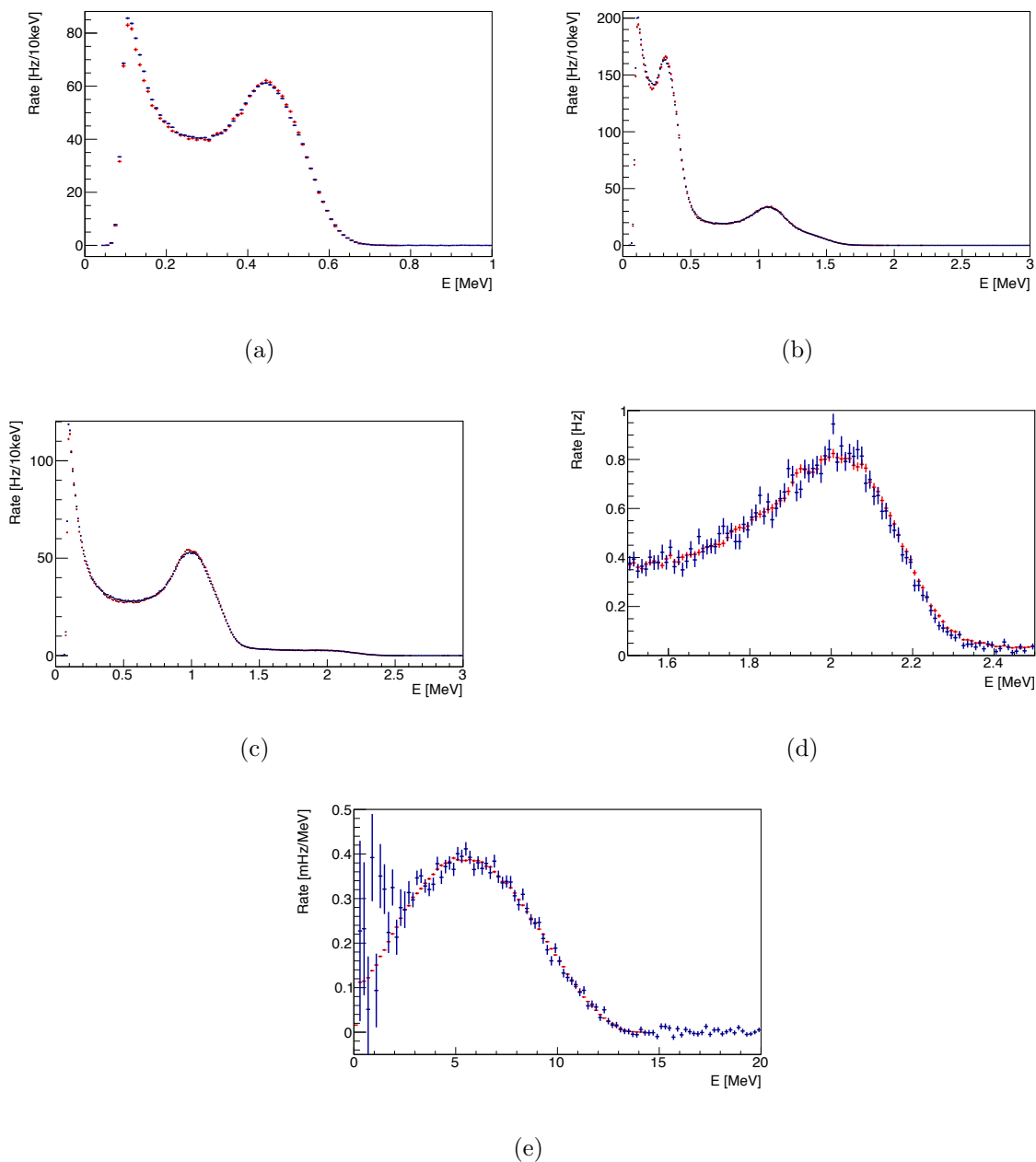


Figure 8.16. The best fit results applied to single-segment data vs. MC comparison. (a)  $^{137}\text{Cs}$ , (b)  $^{22}\text{Na}$ , (c)  $^{60}\text{Co}$ , (d)  $n$ -H capture gamma from  $^{252}\text{Cf}$ , (e)  $^{12}\text{B}$ .

isons were made by comparing calibration spectra and multiplicities of the August and December calibrations. When the MC is compared to data, the nonlinearity parameters were fixed to the best fit values found with the April calibration. This is a powerful cross-check to ensure the best fit detector response model is able to find

good agreement with data independent of time and detector configuration.

The August calibration data was collected with calibration sources deployed at different locations inside the detector to maximize the number of functional segments close to the sources. Similar to the April calibration campaign, the energy scale calibration is organized to deploy only one source in the detector for each calibration. However, one gamma source was possibly left in the volume between the active detector and shielding, shown in Figure 8.17. The contamination from the additional

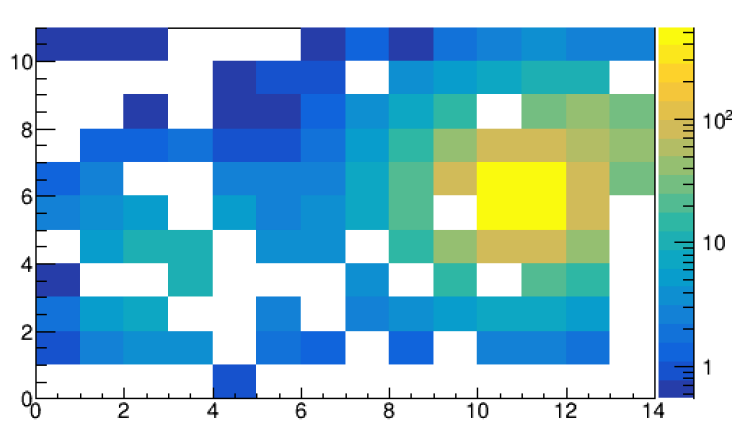


Figure 8.17. The event distribution of gamma event clusters, there is a secondary hot spot indicating another source trapped in the volume between detector volume and shielding.

gamma source can cause an unknown spectrum to be added to the calibration energy spectrum. With a sampling window for each hit of 400 ns, and the time interval between each hit within 20 ns, the overlapping of reconstructed energy from the additional calibration source is rare due to the sources' radioactivity in 1 kBq scale. Hence, the additional source can cause data and MC's disagreement in spectrum shape and multiplicity, but has minimum effect on the energy scale.

The December calibration campaign was organized with same goal as the April and August calibration, with the addition of the AmBe source described in the Section 8.1. Although the  $^{12}\text{B}$  beta energy covers the range of 3 to 13.5 MeV, the

AmBe 4.4 MeV single gamma is an additional powerful cross-check for PROSPECT to demonstrate its energy scale precision in the critical range where the IBD positron spectrum severely disagree with the Huber model. The best fit AmBe MC and data is shown in Figure [8.18](#).

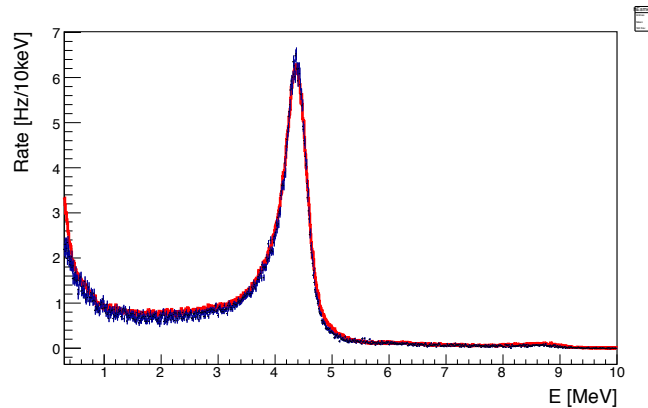


Figure 8.18. AmBe reconstructed energy spectrum compared with the best fit MC.

As a result of the cross-campaign check with the calibrations taken at different time in 2018, the ratio of reconstructed energy of the calibrations and simulations is shown in Figure [8.19](#).

An additional cross-check was made to characterize the reconstructed energy with respect to events with different multiplicities. Figure [8.20](#) shows the  $E_{rec}/E_{mc}$  ratio of events with different multiplicities, in different calibrations in 2018. Despite some of the multiplicity contains extremely small amount to events, the variation of energy scale in different calibration is roughly within 1%.

## 8.5 Position Dependence of Energy Response

The energy response differs at different positions in the detector due to gamma energy leakage. The leakage usually causes coherent downward shifts of the energy distribution. To quantify the energy variation caused by gamma leakage, gamma sources were scanned through multiple PLA rods in the PROSPECT AD along the

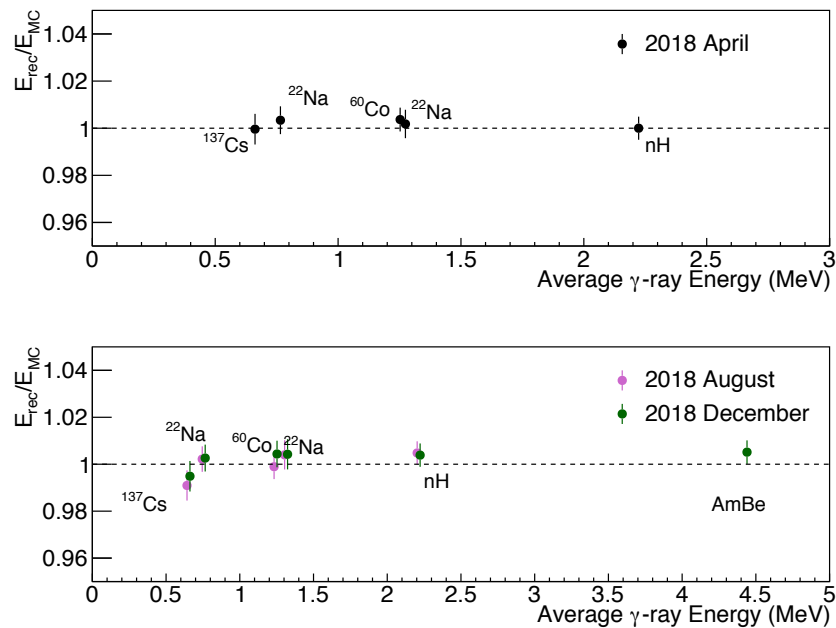


Figure 8.19. The discrepancy between April, August and December calibration energy scale is within  $\sim 0.6\%$  uncertainty. Data points of the August and December calibrations are intentionally shifted for clearer illustration.

$z$ -direction. The  $^{22}\text{Na}$  sources were used to perform this calibration. Event reconstructions of the gamma rays are performed in different volume sizes in the detector, as shown in Figure 8.21. The simulation of gamma leakage was tested by comparing MC simulation to the calibration data for each volume size case. The comparisons include the  $^{22}\text{Na}$  source deployed at the center of detector, near the edge of detector along  $z$  and near the corner of detector on the  $x, y$  plane. The simulated stopping power was also tested by comparing MC simulation to data with energy reconstruction in different sub-volumes of the detector. The one-ring and three-rings volume cases are illustrated in Figure 8.21.

Figure 8.22 shows the results of the different volume comparisons. Sufficient agreement of the energy distributions were found between data and MC. The data-MC differences of energy shift from center to edge are  $8 \pm 1$  keV and  $7 \pm 1$  keV for sources at detector center and corner, respectively. Energy scales are also consistent

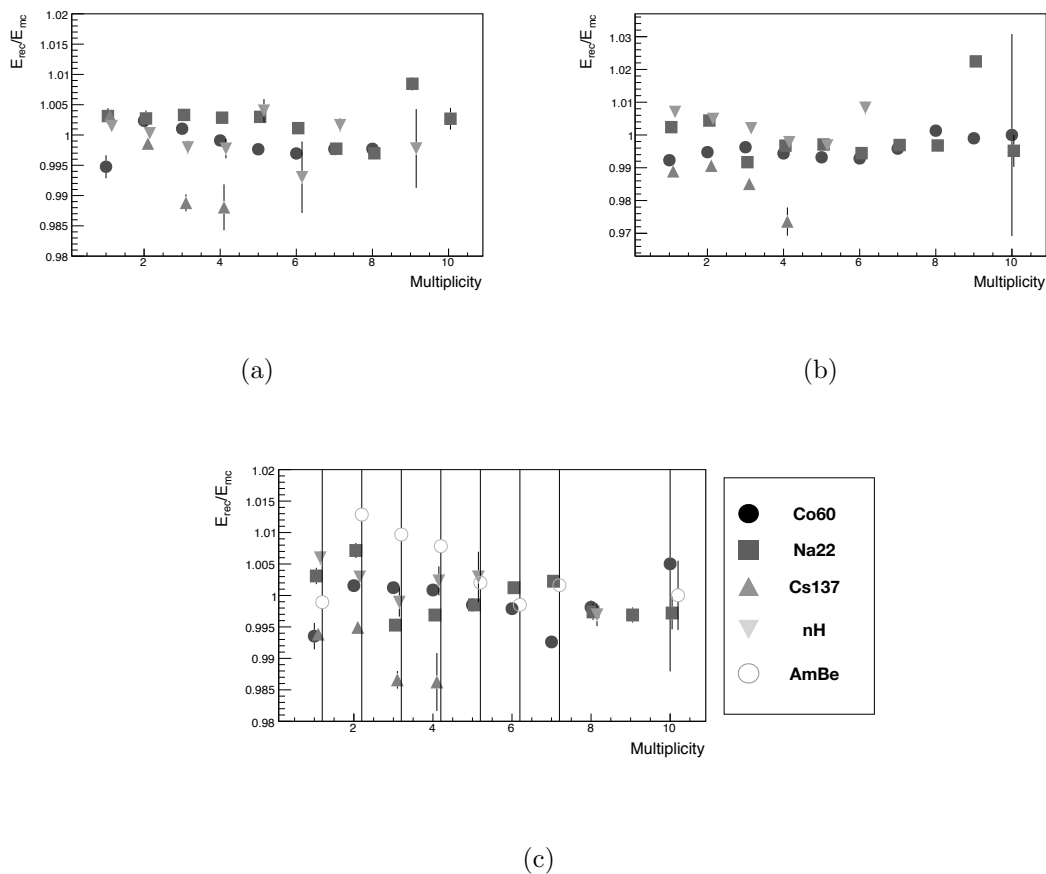


Figure 8.20.  $E_{rec}/E_{mc}$  ratio vs. particle multiplicities in different calibration campaigns in 2018. The statistical errors are shown in the figure. (a) April calibration, (b) August calibration, (c) December calibration.

within the energy scale uncertainty in 1-ring and 3-ring data-MC comparisons. The data-MC difference of energy shifts of 1-ring and 3-ring reconstructions are  $4 \pm 1$  keV and  $5 \pm 1$  keV for sources at detector center and corner, respectively. Therefore, a  $\sim 8$  keV energy shift offset is considered as the uncertainty in the IBD annihilation  $\gamma$  leakage modelling

## 8.6 Energy Scale Stability

The energy scale stability is characterized by analyzing ambient neutron events,

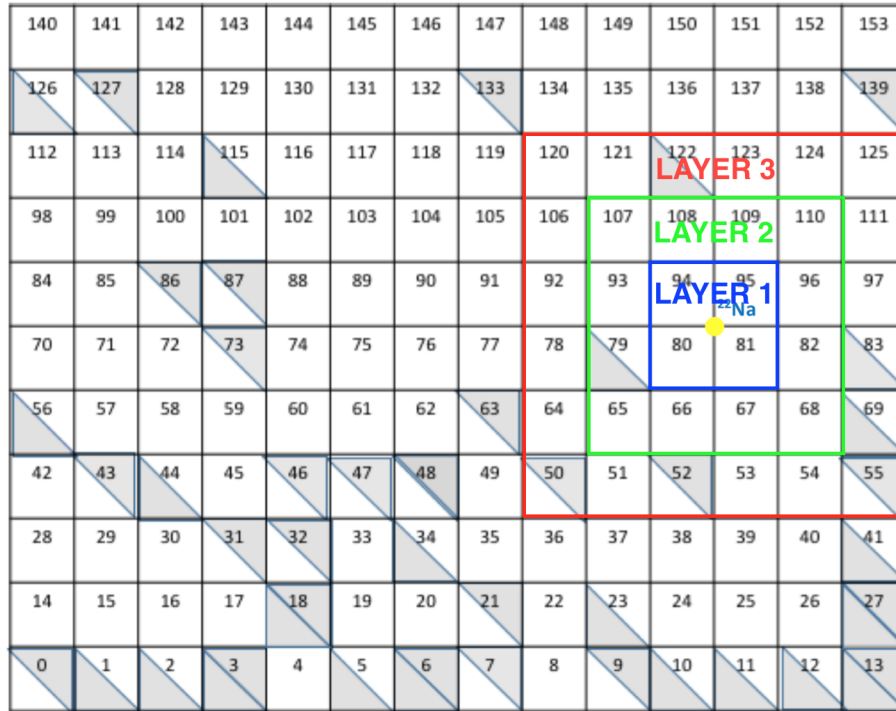
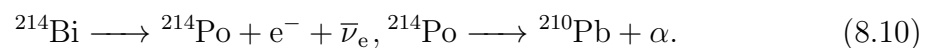


Figure 8.21. Example of different detector volume sizes within three layers (rings) of segments containing the calibration sources. In the case shown in this figure, the  $^{22}\text{Na}$  source is deployed near one edge of the PROSPECT AD.

natural contaminant, and spiked  $^{227}\text{Ac}$  events.

**8.6.1 BiPo Calibration.** The  $\beta$  decay followed by the  $\alpha$  decay from the Bi $\rightarrow$ Po decay chain (BiPo) has a similar time coincidence as IBD events. Alpha particles' small range, highly quenched light yield and high PSD values make their signals stable and easy to select in the PROSPECT AD. Thus, BiPo decay events are used to test the stability of energy scale and resolution. There are two major decay chains involving Bi $\rightarrow$ Po $\rightarrow$ Pb decays. The dominant branch seen in the PROSPECT detector is BiPo from  $^{222}\text{Rn}$ , which is part of the  $^{238}\text{U}$  decay chain, a natural contaminant in most particle detectors. The  $\beta$  and  $\alpha$  are create as:



The  $^{214}\text{Bi}$  decay generates  $\beta$  particles with total energy of 3.275 MeV. The kinetic energy of the  $\alpha$  particle produced in  $^{214}\text{Po}$  decay is 7.685 MeV in 99.99% of decays.

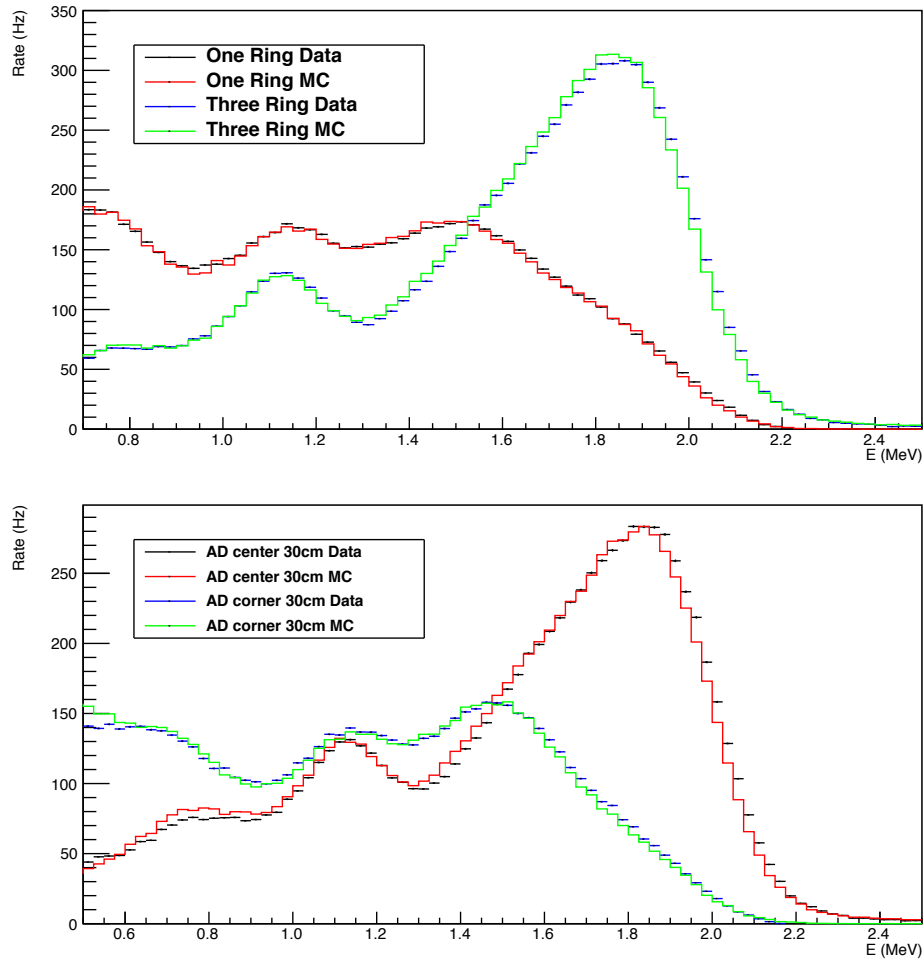
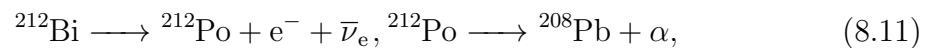


Figure 8.22. (Top) Distribution of total reconstructed gamma energy produced from  $^{22}\text{Na}$  sources deployed at the center of PLA rods. (Bottom) Distribution of total reconstructed gamma energy produced from  $^{22}\text{Na}$  sources deployed near one end of a PMT.

The visible  $\alpha$  energy  $\sim 0.85$  MeV. The other BiPo decay is a part of the  $^{232}\text{Th}$  decay chain, also a natural contaminant of particle detectors.



where the total  $\beta$  energy is 2.25 MeV with 9% probability accompanying with de-excitation gamma ranging from 0.7 MeV to 1.8 MeV. The  $\alpha$  produced has 8.785 MeV kinetic energy and  $\sim 1$  MeV visible energy.

The stability of the reconstructed  $\alpha$  energy is the subject of the energy stability

monitoring.

**8.6.2  $^{227}\text{Ac}$  Calibration.** The Rn-Po decay chain (RnPo) is a part of the decay chain of  $^{227}\text{Ac}$  uniformly spiked in the  $^6\text{LiLS}$ . As shown in Figure 8.23, the RnPo event consists of two coincident  $\alpha$  decays of  $^{219}\text{Rn}$  and  $^{215}\text{Po}$ . The  $^{219}\text{Rn}$  decays with  $Q\text{-value} = 6.95\text{ MeV}$ , and generates an  $\alpha$  particle carrying the majority of the decay energy and a de-excitation  $\gamma$  ray with  $0.27\text{ MeV}$  (10.8%) and  $0.40\text{ MeV}$  (6.6%). The  $^{215}\text{Po}$   $\alpha$  decays produce monoenergetic  $7.39\text{ MeV}$   $\alpha$  particle with 99.99% probability.

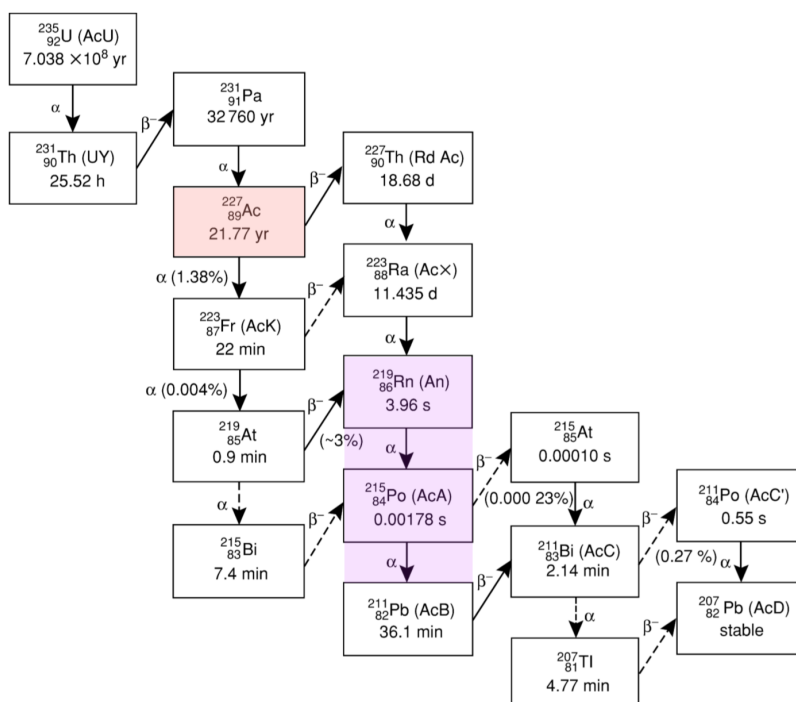


Figure 8.23. The decay chain involving the decays from  $^{227}\text{Ac}$  to the RnPo events.

**8.6.3 Other Stability Monitoring.** The  $2.22\text{ MeV}$  gamma ray of  $n\text{-H}$  capture events from the cosmogenic neutron background is also utilized as a long term monitor of energy scale stability. The de-excitation gamma photons from  $n\text{-H}$  capture are

selected based on time coincidence between proton recoils caused by fast cosmogenic neutron and the delayed gamma hits. Another ubiquitous gamma source is an intrinsic contaminant of  $^{208}\text{Tl}$  uniformly distributed in the detector. The  $^{208}\text{Tl}$   $\beta$  decay produces 2.61 MeV gammas with 99.75% probability.  $^{208}\text{Tl}$  gammas are selected with gamma-like PSD values with no coincident hits. Capture of reactor correlated neutrons in the experimental facilities also produces high-energy gammas. The edge of the reactor correlated gamma spectrum is also monitored to test the detector energy scale stability.

**8.6.4 Quantifying the Stability.** The  $^{214}\text{Po}$ ,  $^{212}\text{Po}$ , and  $^{215}\text{Po}$   $\alpha$  energies, as well as the other single gamma energies are used to monitor the energy scale stability. The energy scale stability for the 2018 reactor neutrino spectrum measurement is shown in the top panel of Figure [8.24](#). The energy scale variation is within  $\pm 0.5\%$  through the full PROSPECT 2018 dataset. The reactor-on and -off difference in energy scale is within  $\pm 0.2\%$ .

## 8.7 Energy Resolution Stability

The energy resolution stability is characterized with the same calibration analysis as the energy scale stability study above. The energy distribution of  $^{214}\text{Po}$ ,  $^{212}\text{Po}$ , and  $^{215}\text{Po}$   $\alpha$  hits, and the single gamma events are fitted with Gaussian functions to quantify the standard deviation in each run. The stability of energy resolution is shown in the upper-middle panel of Figure [8.24](#), indicating energy resolution stability within  $\pm 5\%$  and variation between reactor-on and -off periods of  $\pm 2\%$ .

## 8.8 Position Resolution Characterization

Position reconstruction is vital in IBD selection, for the variation of  $z$  position resolution can cause a change in IBD detection efficiency. BiPo and RnPo events are utilized to characterize the stability of position reconstruction and position resolution.

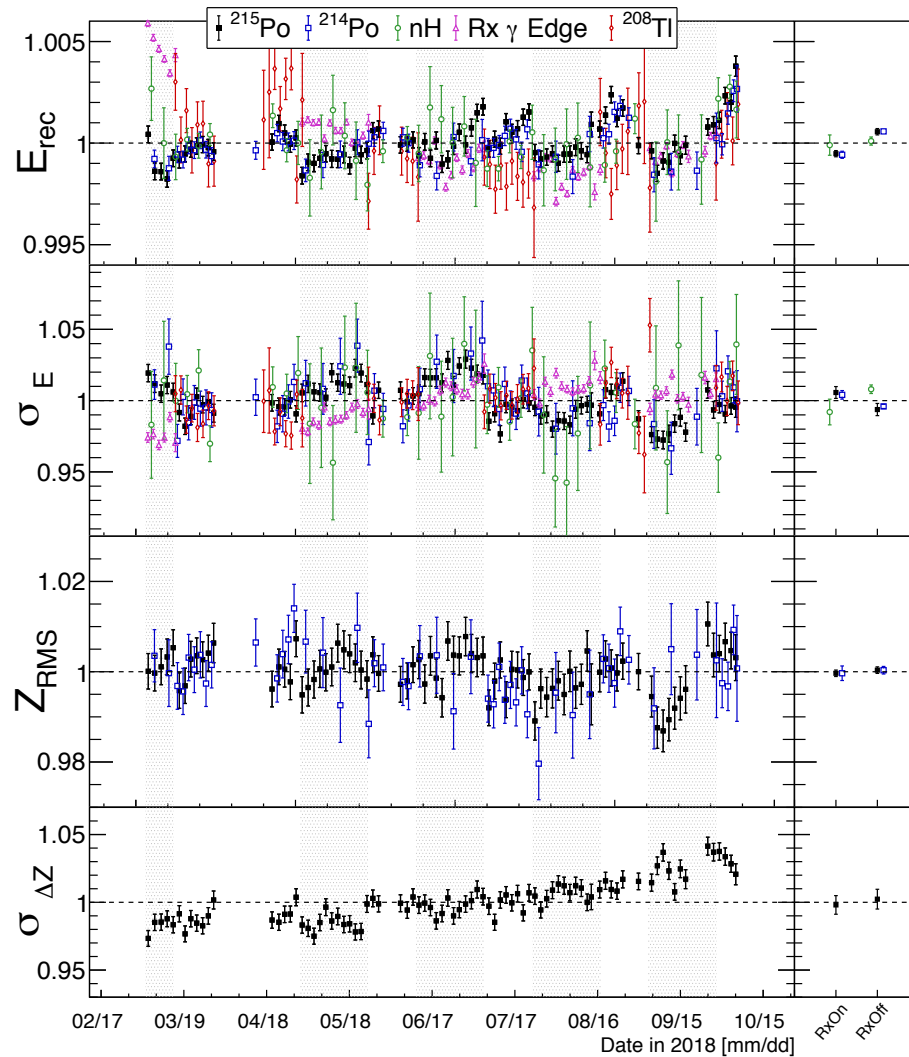


Figure 8.24. (Top) The reconstructed energy scale stability characterized by the BiPo and RnPo  $\alpha$  energy, the gamma energies from the multiple sources. (Top-middle) The energy resolution stability. (Bottom-middle) The RMS of reconstructed  $z$  positions calculated from  $^{214}\text{Po}$ ,  $^{212}\text{Po}$ , and  $^{215}\text{Po}$   $\alpha$  decays. (Bottom) The prompt and delayed  $\Delta z$  of the RnPo  $\alpha\alpha$  decay.

Because the BiPo and RnPo events are uniformly distributed in the detector, the  $z$  position distribution of various Po  $\alpha$  particles can be used to monitor the consistency of  $z$  position reconstruction. Another advantage of the RnPo events is that their vertexes of prompt and delayed signals are approximately at the same position, while the mobility of the  $\alpha$  particles in the PROSPECT AD is on the scale of  $\mu\text{m}$ . Thus, the distribution of prompt and delayed hit distances'  $dz$  is used to quantify the position

resolution along the segments. The  $z$  and  $\Delta z$  distribution of produced  $\alpha$  particles are shown in Figure 8.25. The  $\Delta z$  distribution is fitted with Gaussian function to search for the best fit standard deviation. The resolution of position reconstruction is  $49.9 \pm 0.1$  mm.

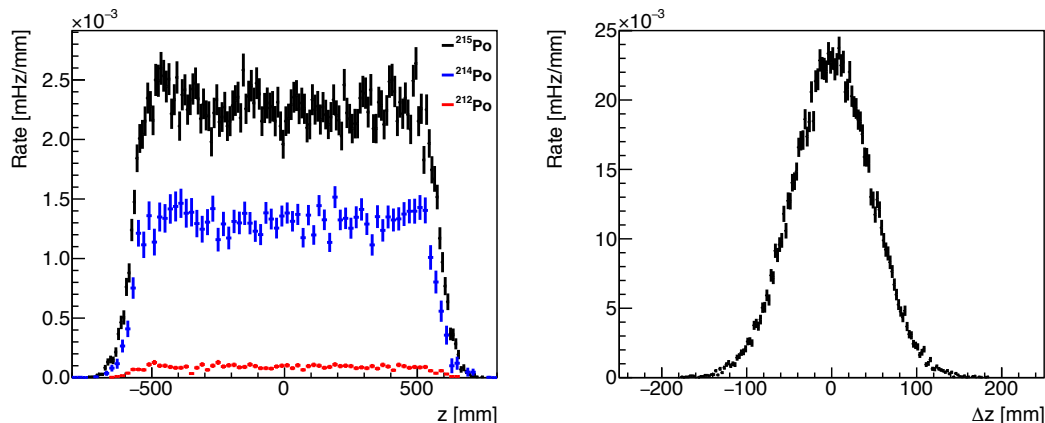


Figure 8.25. (Left) The reconstructed  $z$  distribution of Po produced  $\alpha$  particles in a segment. (Right) The distribution of  $dz$  between prompt and delayed hits of RnPo  $\alpha$ .

The stability of reconstructed position and position resolution is shown in the bottom two panels in Figure 8.24. The variation of reconstructed position are quantified by comparison the RMS of the  $z$  positions of  $^{214}\text{Po}$ ,  $^{212}\text{Po}$ , and  $^{215}\text{Po}$   $\alpha$  hits. The RMS values exhibit stability within  $\pm 1.5\%$  along the 1176 mm long segments, which is equivalent to 2 cm variation. The position resolution calculated with  $\Delta z$  between two RnPo hits indicates 7% (3.5 mm) variation.

## 8.9 Reconstruction Differences Among Segments

Because of  $\alpha$  particles' small range of movement, a RnPo decay's prompt and delay signals are in a single segment. Hence, the spiked  $^{227}\text{Ac}$  is an ideal calibration source to measure the relative segment volume difference by counting the RnPo event rate in each segment. The rate of RnPo events is shown in Figure 8.26, exhibiting that RnPo rates in all segments vary within 2%.

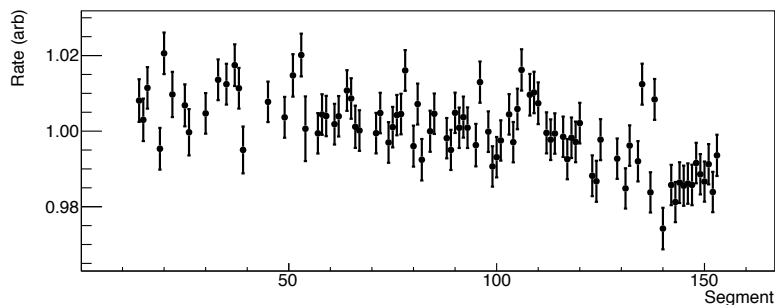


Figure 8.26. The rate of RnPo events in each segment.

The energy of the Po  $\alpha$  decays, as well as the reconstructed gamma energy of  $^{137}\text{Cs}$  gamma calibration throughout the detector, are compared among all segments. The reconstructed energy distribution of the Po  $\alpha$  decays are fitted with a Gaussian function to search for the best mean energy. The gamma energy of  $^{137}\text{Cs}$  detected by each individual segment was compared to a MC template energy spectrum to quantify the energy scale variation among all segments. The variation of energy scale and resolution among segments are shown in Figure 8.27. All segments' reconstructed energies are uniform within  $\pm 1\%$ . Energy resolution of each segment varies within  $\pm 5\%$ .

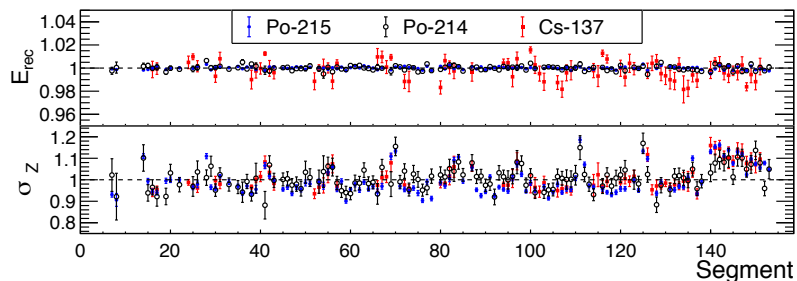


Figure 8.27. (Top) Energy scale variation among all segments. (Bottom) Energy resolution variation among all segments.

## 8.10 Finalized Detector Response Model and Uncertainties for the IBD Spectrum Analysis

According to Section 8.4, the energy non-linearity model was finalized based

on the data vs MC comparison of the full detector reconstructed calibration gammas and neutrons. The energy scale of the PROSPECT AD can be expressed as the ratio of true energy to reconstructed energy of average particles from different calibrations,  $E_{rec}/E_{true}$ , as shown in Figure 8.19. This figure indicates that, at lower energy, the scale is able to vary  $\sim 0.6\%$  from 1. This uncertainty is partially contributed by the energy scale fluctuation caused by the uncertainty the nonlinearity model. Another contributor, a  $0.46\%$  absolute uncertainty that is characterized with  $^{12}\text{B}$  data vs MC comparison discussed below.

Data vs MC comparison of the  $^{12}\text{B}$  energy spectrum was used to demonstrate the energy scale at higher energy, shown in Figure 8.28. The fractional residual calculated between data and MC was fitted with a straight line whose slope is the energy scale difference between data and MC. The best fit slope in Figure 8.28 indicates that the energy scale of data and MC of the  $^{12}\text{B}$  beta spectrum differs by  $0.33 \pm 0.46\%$ .

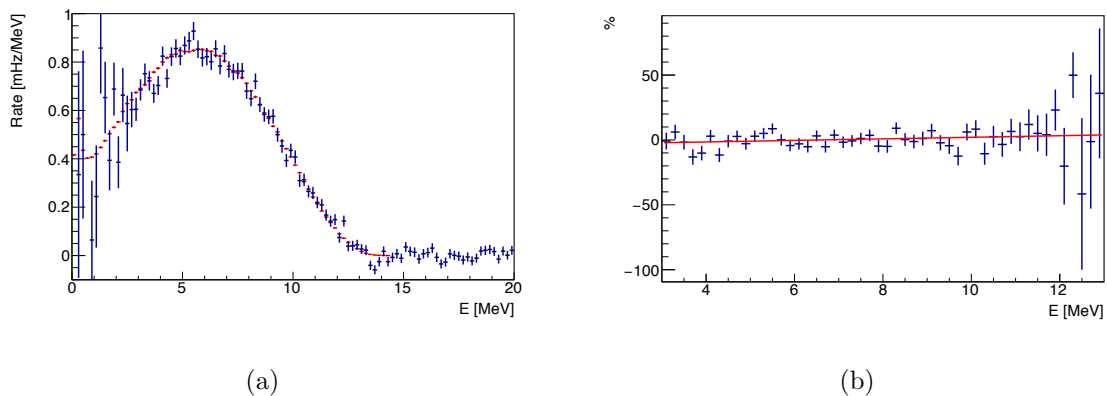


Figure 8.28. (a) Full detector MC-data comparison for the  $^{12}\text{B}$  spectrum. (b) The fractional residual of  $^{12}\text{B}$  data and MC spectrum. The average residual of this comparison indicates a  $0.33 \pm 0.46\%$  energy scale difference between data and MC.

The data vs. MC comparison of the  $^{22}\text{Na}$  gamma spectrum is a good way to indicate the multi-particle event reconstruction capability of the PROSPECT AD, see Figure 8.29. This comparison validates the PG4 model's successful energy reconstruct-

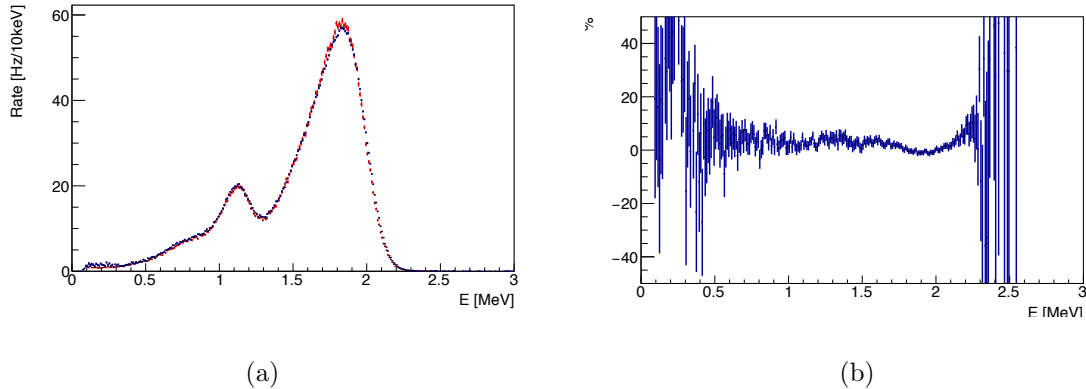


Figure 8.29. The data to MC comparison of the  $^{22}\text{Na}$  spectrum and residual of comparison. (a) Full detector data-MC comparison for  $^{22}\text{Na}$  calibration. (b) The residual of this comparison.

tion of the annihilation gammas. The gamma calibration sources supplied sufficient amount of statistics, such that they contributed negligibly to the overall model uncertainties. The 0.46% energy scale uncertainty and statistical uncertainty in the  $^{12}\text{B}$  spectrum smeared the  $\chi^2$  distribution during the quenching model search, thus enlarging the uncertainty of the nonlinearity model. To be conservative, the 0.46% energy scale uncertainty in  $^{12}\text{B}$  is treated as a systematic energy scale uncertainty.

The energy resolution in Figure 8.30 shows the resolution of each energy distribution of the calibrations, fitted with Function 8.7. The energy resolution at 1 MeV is  $4.76\% \pm 0.2\%$ . This result also validates the Gaussian smearing of all events' energy with the resolution equivalent to 325 PE/MeV photostatistics (described in Section 8.1).

The energy resolutions in the spectrum analysis are forced to be smeared to match the poorest resolution measured in detector during data taking. The uncertainty of the energy resolutions is thus quantified with the uncertainty of the poorest measured photostatistics ( $325 \pm 17$  PE/MeV). This variation is consistent with the run-to-run energy resolution difference observed in the BiPo  $\alpha$  energy resolution.

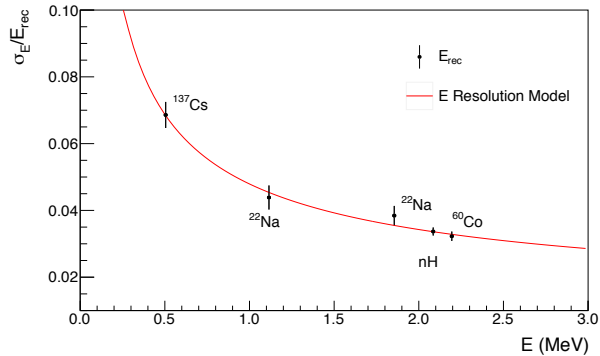


Figure 8.30. The energy resolution characterized with mean energies of each calibration fitted with the resolution function. The errors include both statistical uncertainty and uncertainty of the nonlinearity model.

In conclusion, the uncertainty of energy response includes the following systematic uncertainties:

- The  $1 - \sigma$  uncertainty of effective Birks' constants and effective Cherenkov efficiency, which are  $k_{B1} = 0.132 \pm 0.004$  mm/MeV,  $k_{B2} = 0.023 \pm 0.004$  mm/MeV,  $k_C = 37 \pm 2\%$ ,  $A = 100.26 \pm 0.46\%$ .
- The 0.46% uncertainty of absolute energy scale.
- The analysis ZLE threshold uncertainty of  $90 \pm 5$  keV.
- The uncertainty of the artificial smearing  $325 \pm 17$  PE/MeV.
- The uncertainty of the thickness of the optical separators of  $1.18 \pm 0.05$  mm.

Each of the uncertainties above are turned into a covariance matrix individually. As a result, the covariance matrices from energy scale uncertainty and thickness uncertainty of separators are shown in Figure [8.31](#).

For the IBD spectrum measurement, the finalized calibration to simulation comparisons are shown in Figure [8.32](#). The April gamma calibrations, the  $n$ -H capture

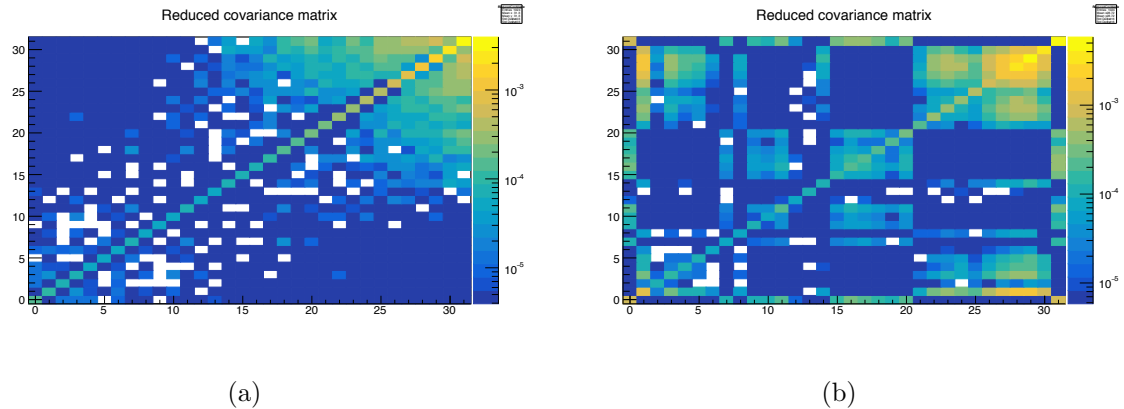


Figure 8.31. The reduced covariance matrices used for PROSPECT’s IBD spectrum analysis. (a) IBD covariance matrix for the uncertainty in the nonlinearity and energy scale model. (b) IBD covariance matrix for the uncertainty of panel thickness.

gamma, and the  $^{12}\text{B}$  beta energy are compared to the data with the uncertainties listed above. The errors of the  $E_{rec}/E_{mc}$  ratio in Figure 8.19 also contain those uncertainties.

The finalized detector response model is processed in the spectrum analysis in the form of a detector response matrix shown in the left plot of Figure 8.33. This matrix translates neutrino energy to the reconstructed IBD prompt energy. The default range of the input neutrino (IBD prompt) energy is from 1.8 to 10 MeV (from 0 to 10 MeV) with bin width of 0.05 MeV. After finalized energy model parameters are implemented in PG4, IBD events are simulated with equivalent neutrino energy uniformly distributed in each bin. The IBD event and neutron momentum distribution is simulated with respect to the HFIR core’s relative location to the PROSPECT AD. With two million IBD events simulated per bin, the energy response of the IBD events in each energy bin can provide sufficient statistical translation from neutrino energy to reconstructed IBD prompt energy. The modeled energy spectrum of a single-energy neutrino MC dataset is shown in the right plot of the Figure 8.33. The inconsistency of a naively smeared and Gaussian fitted prompt energy and the PROSPECT

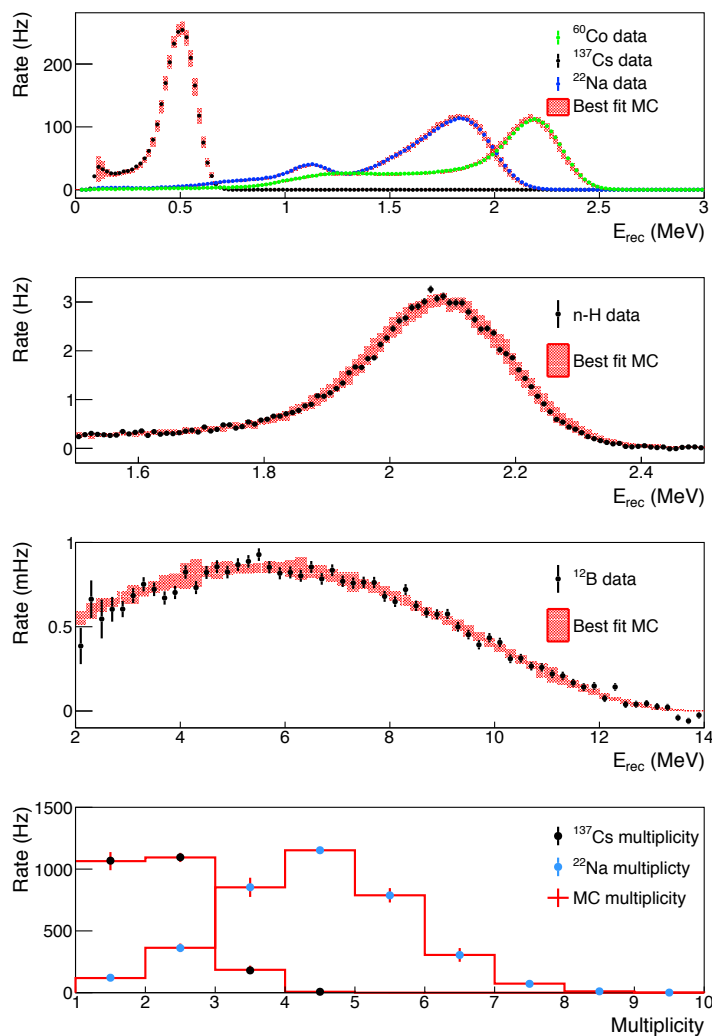


Figure 8.32. Calibration data to best fit MC comparison with energy scale uncertainties. (Top) The  $E_{rec}$  for detector-center  $\gamma$ -ray source deployments; (Center top) The  $E_{rec}$  for  $n$ -H captures from a detector-center  $^{252}\text{Cf}$  source deployment; (Center bottom) The  $E_{rec}$  for cosmogenically-produced  $^{12}\text{B}$ ; (Bottom) The event multiplicity for detector-center  $^{137}\text{Cs}$  and  $^{22}\text{Na}$  source deployments. Error bands indicate statistical (data) and systematic (PG4) uncertainties.

reconstruction is caused by

- Energy loss in dead volumes of the PROSPECT AD.
- The 90 keV analysis ZLE threshold excludes low energy hits from a portion of clusters, reducing their total energy and widening and lowering the total energy

distribution.

- The electron-positron annihilation gamma energy leakage, as well as the missing positron energy in dead segments, cause a significant amount of the prompt events with only one 511 keV energy deposition.
- The energy response nonlinearity.

Being able to predict the detector response including unavoidable energy loss and resolution smearing, this detector response matrix is able to provide trustworthy conversion between neutrino energy and reconstructed IBD energy spectrum.

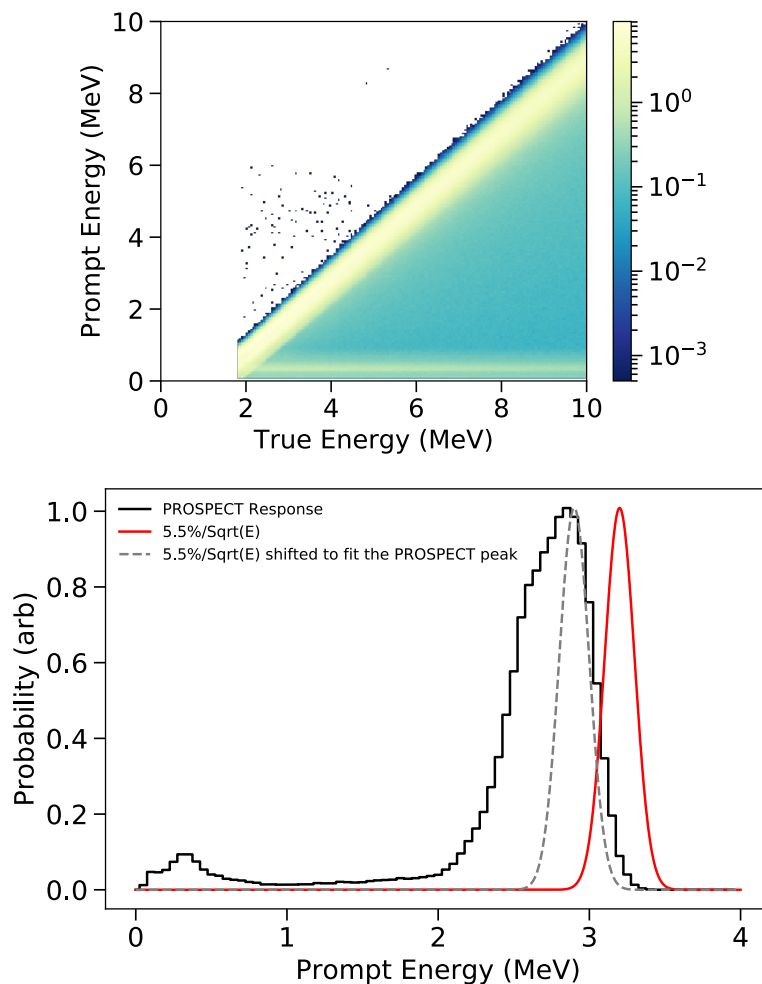


Figure 8.33. Top) The detector response matrix for the conversions from neutrino spectrum models to PROSPECT's expected IBD prompt energy spectrum. (Bottom) The IBD prompt energy spectrum generated from a 4.0 MeV antineutrino simulated through PG4. The red line represents a  $\sim 3.2$  MeV prompt energy with Gauss function smearing equivalent to 5.5% energy resolution. The gray dashed line is the smeared prompt energy shifted to match the PROSPECT reconstructed mean energy.

## CHAPTER 9

IBD PROMPT ENERGY SPECTRUM OF ANTINEUTRINOS FROM  $^{235}\text{U}$ 

With event selections based on multiple aspects of the prompt and delayed coincidence and cosmic ray exclusion, PROSPECT is able to detect reactor neutrinos with minimal overburden. The first reactor neutrino oscillation measurement from PROSPECT [93] was made using 33 exposure days reactor-on and 30 exposure days of reactor-off data. The first IBD prompt energy spectrum of antineutrinos from HFIR was measured after  $\sim 78$  days (40.3 reactor-on exposure days, 37.8 reactor-off exposure days) of total data acquisition [94]. In this thesis, the IBD prompt energy spectrum measurement is reported. Because of the limited detector dynamic range and the energy range of IBD prompt energy, the prompt energy spectrum between 0.8 MeV and 7.2 MeV is studied. The reactor correlated energy spectrum is obtained with reactor off backgrounds subtracted from reactor on IBD candidates. To do this, delicate background stability characterization and corrections were performed. To quantify the contribution of  $^{235}\text{U}$  to the 5-7 MeV excess of the reactor neutrino spectrum with respect to the Huber model [67], the PROSPECT measured IBD spectrum was compared to a variety of spectrum models.

### 9.1 IBD Event Selection

The reconstructed IBD event rate and energy spectrum was blinded until the IBD event selection values were frozen. PROSPECT's initial reactor neutrino oscillation measurement was based on IBD event selection developed with 3 days of reactor-on and reactor-off data. The IBD selection for the prompt energy spectrum measurement was further studied with the oscillation measurement data before unblinding additional data. Some IBD selection values were adjusted to optimize signal

stability, signal to background ratio (S:B), and total event statistics.

The IBD event selections are selections based on PSD, time coincidence between prompt and delayed clusters, topological spread of the IBD clusters, and detector volume cuts. Acceptance values of IBD selection and the physical purpose of each cut are shown in Table 9.1 and 9.2. The PSD values of prompt and delayed hits are used to identify the type of particle.

Table 9.1. All cuts of IBD event selections (page 1 of 2).

Event Class	Category	Accepted value	Purpose
Prompt	PSD	$< 2.5\sigma$ of lower PSD distribution	Purify positron and gamma selection
$n$ -Li	PSD	$< 3.6\sigma$ of $n$ -Li PSD distribution	select $n$ -Li hits based their PSD range
	energy	$< 3\sigma$ of $n$ -Li energy distribution	select $n$ -Li hits based energy range
Prompt-delay correlations	$\Delta t$	1-120 $\mu$ s	maximize the window for the delayed $n$ -Li hits
	$\Delta(x, y)$	same segment or adjacent segment (0 to 14.5 cm)	close prompt-delay vertex
	$\Delta z$	180 mm (same segment) 140 mm (adjacent segment)	close prompt-delay vertex

Table 9.2. All cuts of IBD event selections (page 2 of 2).

Event Class	Category	Accepted value	Purpose
Cosmic shower	muon veto	$>  200  \mu\text{s}$ from a muon event	reject accidental background correlated with muon shower
	fast neutron veto	$>  200  \mu\text{s}$ from a uncorrelated $n$ -Li hit	reject accidentals correlated with cosmic neutron
	heavy particle recoil veto	$>  200  \mu\text{s}$ from a uncorrelated from heavy particle	reject accidentals correlated with cosmic shower
Fiducial volume	$z$ range	$<44.4$ cm from segment center	veto accidentals with the scintillator at edges
	segment exclusion	prompt vertex inside the fiducial volume	veto accidentals with the scintillator at edges

In the study of optimizing IBD selection, an *effective count* was defined as

$$\text{count}_{\text{effective}} = \sum_{0.8\text{MeV}}^{7.2\text{MeV}} \frac{1}{\sigma_{\text{relative}}^2}, \quad (9.1)$$

where

$$\sigma_{\text{relative}} = \sqrt{\sigma_{\text{on}}^2 + \sigma_{\text{off}}^2 + 2(5\% * \sigma_{\text{off}}^2)}. \quad (9.2)$$

Both  $\sigma_{\text{on}}$  and  $\sigma_{\text{off}}$  consist of a statistical uncertainty and 5% systematic uncertainty of IBD candidates collected in the reactor-on and -off period, respectively. Additionally,

the reactor off normalization uncertainty of 5% of the total uncertainty was added under the consideration of the time dependence of the IBD rate. The IBD selection was optimized by searching for various acceptance values to maximize the effective count.

The PSD selection of prompt and delayed hits are based on the PSD distribution of all events collected in a one hour run. The PSD distribution of all hits in the PROSPECT detector, as well as an illustration of the IBD coincident hit selection are shown in Figure 9.1. By selecting events dynamically with PSD distributions, the time dependence of particle identification is minimized.

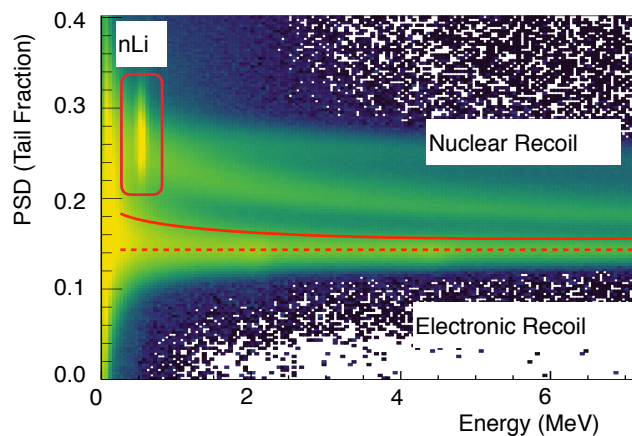


Figure 9.1. Illustration of the IBD PSD selection, where the solid line and dashed line are  $2.5\sigma$  threshold for positron- and gamma-like hits and the mean of their PSD distribution. The red circle represents the small range of PSD and energy for  $n$ -Li-capture-like hits.

The time coincidence of prompt and delayed clusters requires a 1 to 120  $\mu\text{s}$   $\Delta t$  window, that is

$$\Delta t \equiv T_{\text{delayed}} - T_{\text{prompt}} \quad (9.3)$$

Other time cuts are applied to minimize accidental IBD candidate (henceforth referred to as ‘accidental’) rates, cosmogenic showers, and fast neutrons of cosmic ray back-

grounds and reactor correlated non-IBD events. Topology cuts require close distance prompt and delayed hits to further reduce accidentals. In the PG4 simulation of the detector response to cosmic backgrounds, the out-most layer of segment was found to contain significantly more backgrounds than the inner segments. Thus, IBD prompt hits in the exterior segments are excluded. The interior segments of the PROSPECT AD are referred to as the *fiducial volume*. Once again, the finalized IBD selection values are listed in Table ???. The simulated IBD prompt energy spectrum is shown in Figure 9.3.

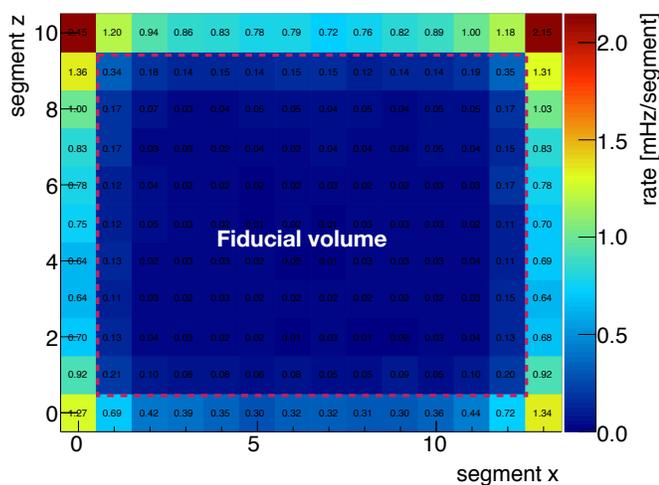


Figure 9.2. Illustration of the detector fiducial volume from the PG4 simulation of the cosmic ray background, where the accidental rate of each segment is shown. The higher accidental rate in the exterior segments lead to selection of IBD candidates within the fiducial volume.

## 9.2 Observation of Reactor Neutrinos on Earth's Surface

PROSPECT is able to detect reactor neutrinos with minimal overburden. With the first two-hour reactor-on dataset, PROSPECT is able to detect a  $> 5\sigma$  signal of reactor neutrinos from HFIR. In the first 24 hours of reactor-on data acquisition and the same duration of reactor-off data, the PROSPECT AD collected  $1254 \pm 30$  reactor on correlated IBD events and  $614 \pm 20$  reactor-off IBD-like candidates. PROSPECT's capability of detecting reactor neutrinos under high cosmic backgrounds is due to the

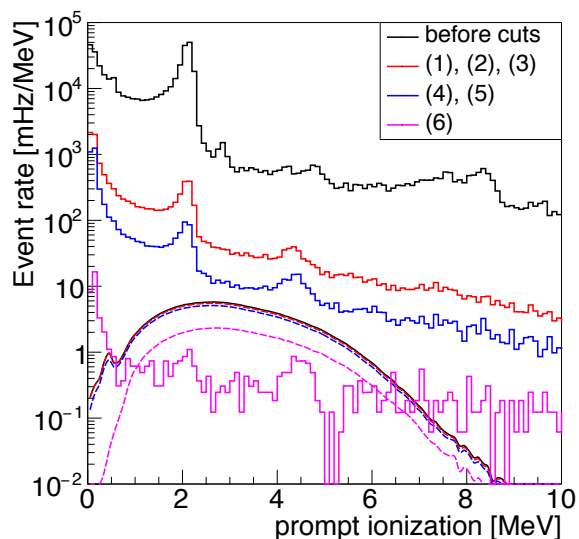


Figure 9.3. The amount of IBD candidates and cosmic backgrounds passing different levels of IBD selection cuts. (1, 2, 3) Cosmic background veto time windows, including muon veto, fast neutron, and single nuclear recoils. (4, 5) Topological cut of prompt and delay distance. (6) Fiducial volume.

precise timing and topological cuts enabled by optical segmentation and PSD.

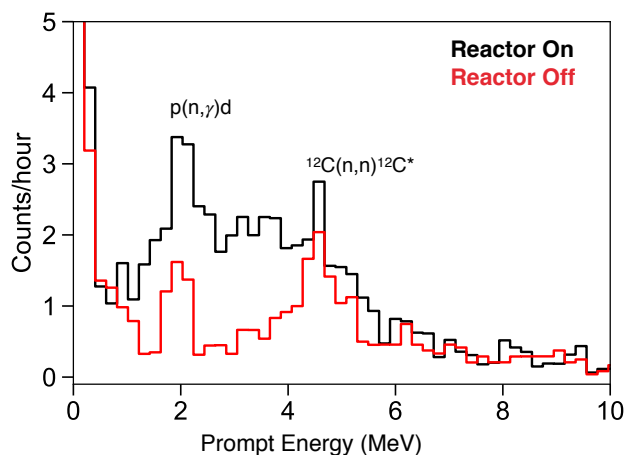


Figure 9.4. The reactor-on and -off IBD prompt energy spectra measured with 24 hours of reactor-on and -off data, separately. Two major background contributions in the spectra are the cosmic IBD-like events with  $n$ -H capture gamma and the gamma from  $n$ -carbon inelastic scattering.

### 9.3 Background Subtraction

Among the selected IBD candidates, the cosmogenic neutrons are the main source of background in PROSPECT's IBD measurement. The background mainly contains the inelastic recoil of fast neutrons, a 2.2 MeV  $n$ -H capture de-excitation gamma and the 4.4 MeV de-excitation gamma from  $n$  carbon inelastic scattering (nC\*). Measured the IBD prompt energy spectrum is a result of background subtraction,

$$S_{IBD} = (S_{on-corr} - \frac{T_{corr}}{T_{acc}} S_{on-acc}) - k \cdot \frac{T_{on}}{T_{off}} (S_{off-corr} - \frac{T_{corr}}{T_{acc}} S_{off-acc}), \quad (9.4)$$

where  $S_{on-corr}$  ( $S_{off-corr}$ ) is the reactor-on (-off) correlated prompt spectrum, when  $1 < \Delta t < 120 \text{ } \mu\text{s}$ . The accidental candidates are uncorrelated beta/gamma and  $n$ -Li capture hits defined as  $-12 < \Delta t < -2 \text{ ms}$  in PROSPECT data analysis. Prior to subtraction, the accidental spectrum was normalized based on the time window length with respect to the IBD coincident window. Additionally,  $k$  is a factor that varies with time that is applied to the reactor-on and reactor-off ratio to correct time dependent event rate differences.

The event rate of cosmic ray backgrounds is time dependent because of environmental atmospheric thickness variation (directly reflected by the variation of atmospheric pressure). By comparing fast neutron, single  $n$ -Li capture, and muon rates to the atmospheric pressure with respect of time, the correlation between atmospheric pressure and event rates was found. In analysis, these correlations are simplified with a linear function fitted to event rate vs. atmospheric pressure data points shown in Figure 9.5. A correction factor based on atmospheric pressure was applied to the normalization of reactor-on and -off prompt energy spectra in order to subtract background correctly. After adjustments based on atmospheric pressure, the IBD correlated candidate rates during the data acquisition period are stable, as shown in Figure 9.6.

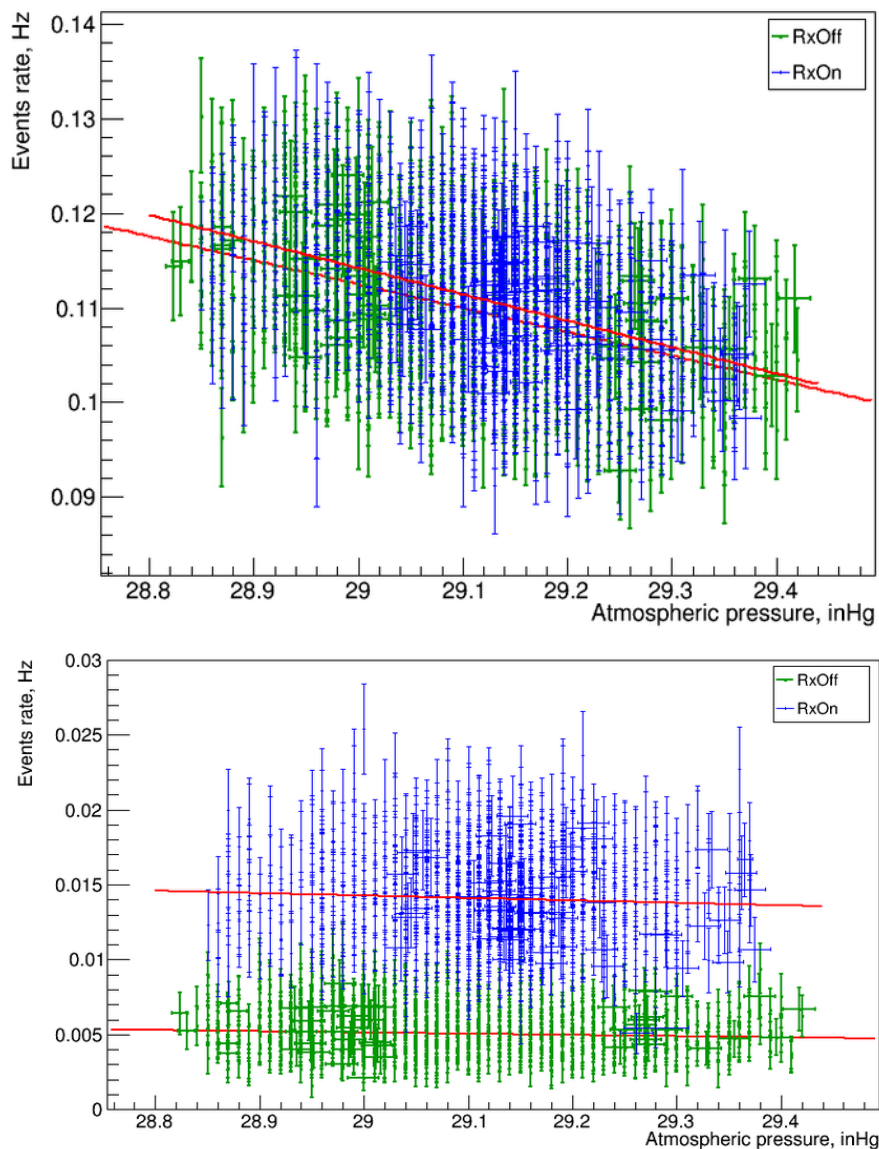


Figure 9.5. (Top) The correlation between fast neutron + single  $n$ -Li events and atmospheric pressure. (Bottom) The correlation between IBD event rate and atmospheric pressure. Because reactor correlated event rate is higher, the reactor-on and -off data points are fitted separately with linear functions.

The reactor-on and -off data dead time caused by the shower veto requirements varies from 14% to 11% of the total exposure time, due to reactor correlated time-varying gamma ray backgrounds that entered the nuclear recoil band. Finally, a correction factor of  $0.991 \pm 0.004$  was multiplied to the background IBD prompt spectrum normalization by comparing the average reactor-on and -off atmospheric

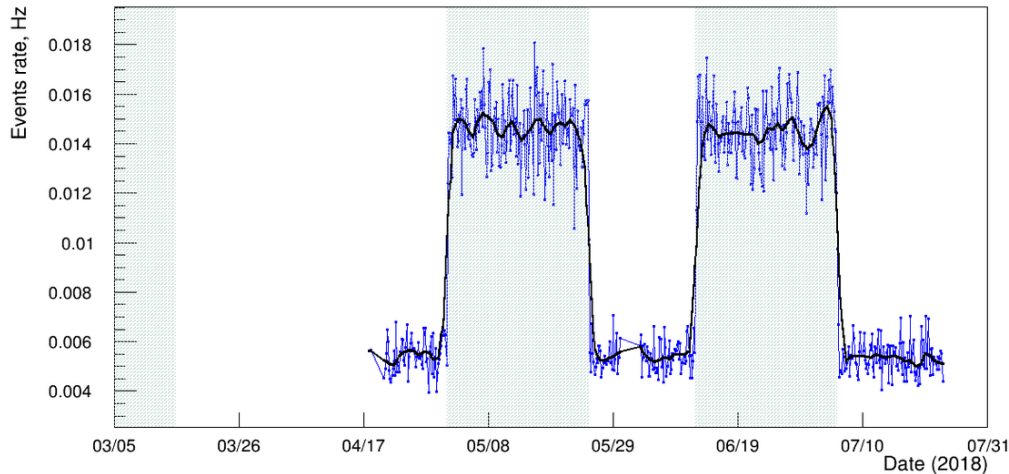


Figure 9.6. The rate IBD correlated candidates with adjusted with local atmospheric pressure. One data point is the event rate in every four hours.

pressures [95] and dead time corrected exposure time.

The energy reconstruction stability of the IBD measurement was evaluated by comparing two reactor-off IBD prompt spectra equally divided, which is independent from possible power variation of the reactor. The comparison between IBD prompt energy spectra from the two periods is shown in Figure 9.7. This two-period comparison validates the correction of atmospheric pressure, as well as the energy reconstruction stability, with  $\chi^2/\text{NDF} = 35.6/56$ .

#### 9.4 IBD Prompt Energy Spectrum

PROSPECT's first HFIR  $^{235}\text{U}$  reactor neutrino spectrum measurement included 40.3 exposure days of reactor-on data and 37.8 exposure days of reactor-off data. In the energy range from 0.8 MeV to 7.2 MeV, total amount of reactor-on (-off) IBD candidates is  $70811 \pm 267$  (stat.) ( $20036 \pm 145$  (stat.)) After subtraction of accidental events, there were  $50277 \pm 267$  (stat.) reactor-on correlated IBD candidates and  $18600 \pm 145$  (stat.) from reactor-off cycles. The total number of reactor correlated IBD events is  $31678 \pm 304$  (stat.), with correlated S:B = 1.7:1. The measured

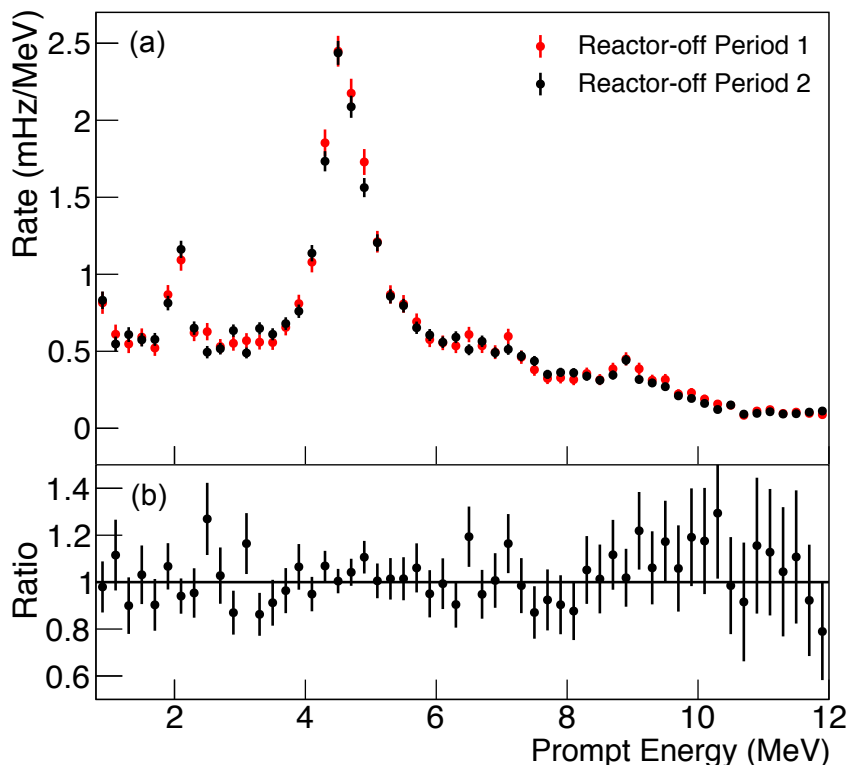


Figure 9.7. The comparison between reactor-off energy spectra of two time periods. (a) Energy spectra of reactor-off IBD candidate events with statistical errors. (b) Ratio between two periods.

prompt energy spectrum is shown in Figure 9.8. With 78 days of exposure, the IBD prompt energy spectrum of HFIR measured by PROSPECT became a direct  $^{235}\text{U}$  antineutrino spectrum measurement with the highest-ever precision, compared with  $\sim 5000$  IBD events measured in ILL [50].

## 9.5 Comparison with Spectrum Models

The goal of the PROSPECT spectrum measurement is to test the  $^{235}\text{U}$ 's contribution to previous LEU experiments' spectrum data-model disagreement, which is described in Chapter 2. To achieve this goal, the IBD prompt energy spectrum of HFIR is subject to comparisons with spectrum models. This study requires spectrum

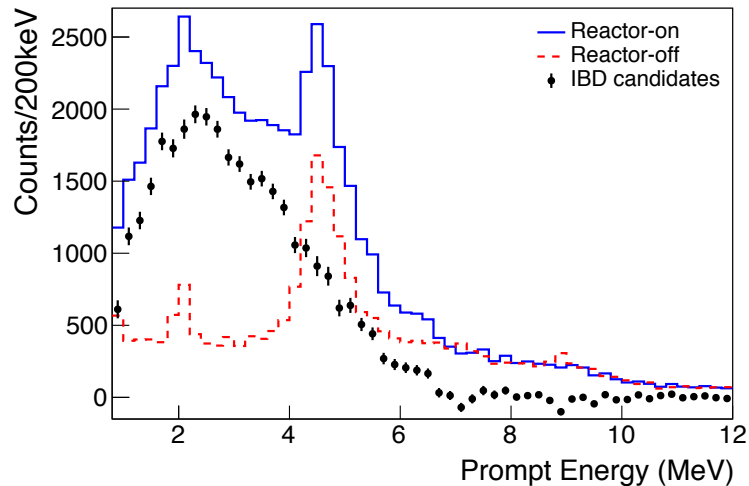


Figure 9.8. First PROSPECT IBD prompt energy spectrum from HFIR, where error bars indicates statistical error only.

model generation, uncertainty processing, and hypothesis testing.

**9.5.1 Spectrum Models.** Spectrum models were generated by multiplying a theoretical prediction of the neutrino spectrum with the IBD cross-section and the detector response matrix described in Section 8.10. The multiplication with PROSPECT’s detector response matrix maps antineutrino energy to PROSPECT reconstructed energy. In this study, the Huber model of the  $^{235}\text{U}$   $\bar{\nu}_e$  spectrum [67] was compared to the PROSPECT measured spectrum under the assumption that no distortion of spectrum is caused by possible sterile neutrino oscillation. In addition, two HFIR specific reactor correlated IBD sources were modeled as minor corrections to the models. The aluminum structure of the HFIR core generates  $\bar{\nu}_e$  through  $\beta$  decay of  $^{28}\text{Al}$ , whose half-life is 2.24 minutes and  $Q$ -value = 2.86 MeV. The short reactor cycle also introduces non-equilibrium fission isotopes that take days to achieve equilibrium of reaction. Neutrinos from  $^{28}\text{Al}$  and non-equilibrium isotopes contributes to the IBD prompt spectrum mainly in the  $< 4$  MeV energy region, with  $\sim 0.8\%$  and  $\sim 0.5\%$  contribution factors, respectively. The IBD prompt spectrum models with/without  $^{28}\text{Al}$  and non-equilibrium contribution are shown in Figure 9.9. The contribution from

spent nuclear fuel is negligible.

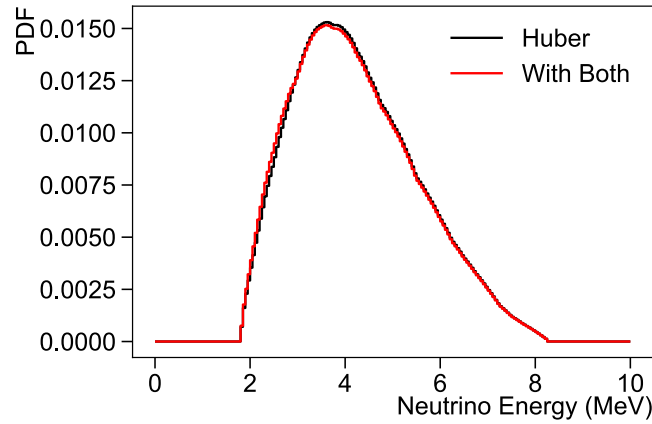


Figure 9.9. Prompt spectrum model generated from Huber's prediction of  $^{235}\text{U}$  spectrum with the PG4 generated detector response matrix. The spectrum model was adjusted with the contributions from  $^{28}\text{Al}$  decay and non-equilibrium isotopes in the HFIR core.

In order to search for the contribution of  $^{235}\text{U}$  to the spectral shape discrepancy observed in LEU neutrino experiments, the spectrum model was adjusted with a Gaussian function whose magnitude was allowed to float.

**9.5.2 IBD Prompt Spectrum Data to Model Comparison.** Spectral shapes of the IBD data and model were compared through the evaluation of  $\chi^2$ ,

$$\chi^2 = \Delta^T \mathbf{V}^{-1} \Delta,$$

where

$$\Delta_i \equiv N_i^{obs} - N_i^{pred} \times (1 + \eta), \quad (9.5)$$

where  $\Delta_i$  is the difference between the experimental measurement and prediction,  $\eta$  is a normalization nuisance parameter and  $\mathbf{V}$  is a full covariance matrix, processing statistical and systematic uncertainties. This full covariance matrix was summed from covariance matrices of uncertainties of various aspects of analysis, such as the energy model uncertainty described in Section [8.10](#). A single covariance matrix was produced

by comparing IBD spectrum models to toy spectra with specific variables allowed to vary within a predetermined uncertainty range. The systematic uncertainties studied and included in the covariance matrix are listed in Table 9.3. The full covariance matrix for data for the model comparison is shown in Figure 9.10.

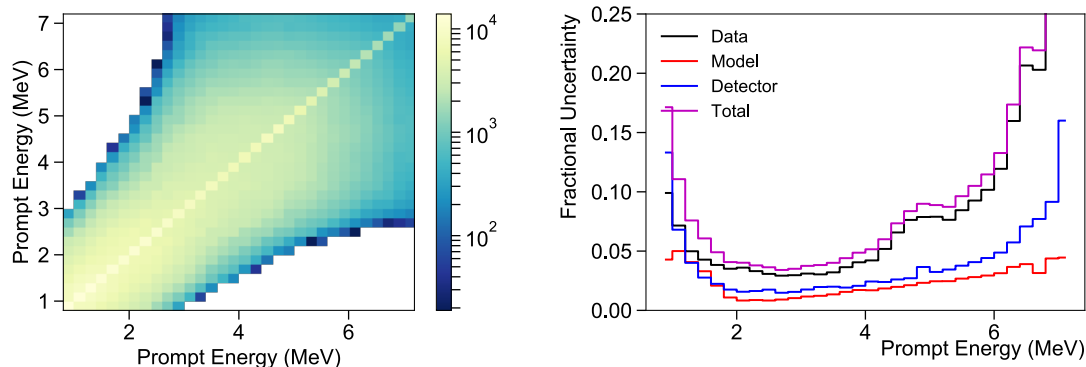


Figure 9.10. (Left) Full covariance matrix used in PROSPECT spectrum and model comparison. (Right) The diagonal terms of the different covariance matrices. Currently, the uncertainty of PROSPECT’s spectrum measurement is statistically dominated.

The spectral shape contribution to the total  $\chi^2$  in different energy range is defined as

$$\tilde{\chi}_i = \frac{N_i^{obs} - N_i^{pred}}{|N_i^{obs} - N_i^{pred}|} \sqrt{\chi_{original}^2 - \chi_{i,new}^2} \quad (9.6)$$

The energy distribution of the local  $\chi_i^2$  is used to characterize the deviation in each energy bin. The PROSPECT measured IBD prompt spectrum is shown in Figure 9.11, along with local  $\chi^2$  contributions and data-model ratios.

**9.5.3 Results.** In the comparison between the PROSPECT measured spectrum and the adjusted Huber spectrum model,  $\chi^2/\text{NDF} = 51.4/31$ , with a one-sided  $p = 0.01$ . Most significant local discrepancies were found in the range from 2.8 MeV to 3.5 MeV, and  $> 6.5$  MeV energy, with  $2 - 3\sigma$  significance.

An *ad hoc* spectrum model was made based on the Huber spectrum to allow regional spectral shape, in 5-7 MeV  $\bar{\nu}_e$  energy, to change with a Gaussian. The best-fit

Table 9.3. List of systematic uncertainties.

Systematic uncertainty	$\sigma$	Description
Background normalization	0.5%	uncertainty of the time dependent event rate
Background $n$ -H peak height	4%	the variation of $n$ -H peak height
Energy reconstruction factors	-	described in detail Section 8.10
Energy leakage	8 keV	the data to MC difference of in energy shift from $^{22}\text{Na}$ calibration at different positions in detector
$z$ fiducial volume	25 mm	position reconstruction variation
$^{28}\text{Al}$ contribution	100%	uncertainty of contribution factor to the spectrum
Non-equilibrium isotope contribution	100%	uncertainty of contribution factor to the spectrum

*ad hoc* spectrum model is shown in Figure 9.11(b), suggesting a distortion magnitude  $n = 0.69 \pm 0.53$  observed by PROSPECT, as a ratio to Daya Bay measured magnitude of excess 1. This result is compatible with hypothesis of equal isotopic contribution

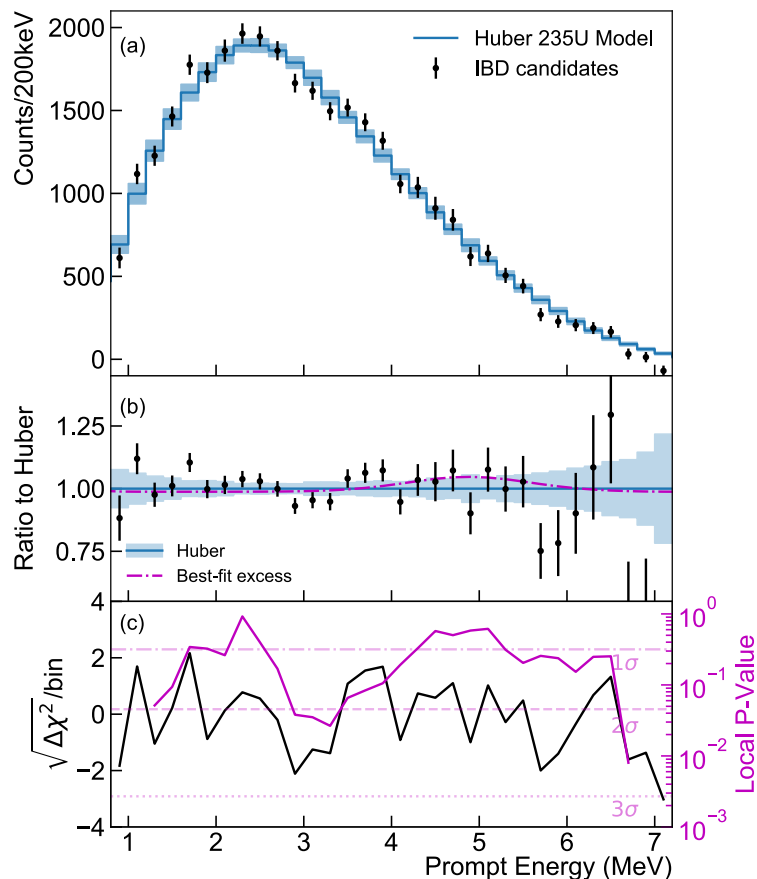


Figure 9.11. (a) PROSPECT measured spectrum compared to adjusted Huber spectral model [94], with error bars including both statistical and systematic uncertainties. (b) The IBD prompt spectrum ratio to the adjusted Huber model, a best-fit *ad hoc* distortion to the model at the 4-6 MeV region. (c) The  $\chi^2$  contribution from each energy bin and the local  $p$ -values in 1 MeV wide regions.

( $n = 1$ ) and the Huber model ( $n = 0$ ), with current uncertainties. The PROSPECT measured IBD spectrum disfavors (with  $2.1\sigma$ ) the hypothesis that the regional excess is caused solely from  $^{235}\text{U}$  ( $n = 1.78$ ).

## CHAPTER 10

### CONCLUSION

The PROSPECT experiment was built to directly measure the  $^{235}\text{U}$  generated antineutrino energy spectrum. The experiment also relies on measuring relative spectral difference at various baselines to probe the short baseline oscillations involving a sterile neutrino. Its short baseline measurement at HFIR contains challenges of high reactor correlated and cosmic ray backgrounds. The PROSPECT AD was therefore designed as an optically segmented LS target for accurate reconstruction of particle tracks and vertex positions. High precision fabrication and 3D printing were applied to build the optical grid subsystem, in order to minimize the dead volume of the liquid scintillator detector. The interlocking between the PLA rods and separators allows exclusive features for the calibration source insertion and event position calibration. After approximately one year of component fabrication and detector construction, the PROSPECT AD was commissioned in February 2018.

As a vital step for the  $^{235}\text{U}$  spectrum measurement, energy scale calibration - setting the relationship between neutrino energy and reconstructed IBD energy - presented unique challenge because of the segmented nature of the PROSPECT AD. Energy and hit loss in the detector, as well as the Birks' quenching and Cherenkov effects in the scintillator light yield were studied exhaustively with radioactive calibration sources and ambient particle interactions. The dependence between cluster energy and segment multiplicity of a particle requires simulation of complicated nonlinear effects and detector structure to characterize the full detector response. The  $\frac{dE}{dx}$  calculated by Geant4 enables simplification of the nonlinear effect simulation. By fitting multiple calibration sources' data with MC simulation simultaneously, the best-fit energy response model was constrained with sub-1% energy scale uncertainty. Signif-

icant computing resources were used in this parameter searching process. Subsequent variations of event reconstruction dependent on time and position were quantified and removed.

PROSPECT measured the IBD prompt energy spectrum from HFIR with  $\sim 78$  exposure days and collected  $31678 \pm 304$  reactor correlated neutrino events on the Earth's surface, with S:B = 1.7:1. The Huber spectrum model with corrections specific for HFIR was compared to the PROSPECT measured spectrum. With current statistics, the PROSPECT measured spectrum was found to be compatible with both Huber and the "equal isotope" hypothesis with relatively high  $\chi^2/\text{NDF}$ , and disfavored the "all  $^{235}\text{U}$ " hypothesis at  $2.1\sigma$ .

## 10.1 Personal Contribution

My personal contributions to PROSPECT's reactor neutrino spectrum include:

- During the early detector R&D with prototypes, I participated the prototype construction, tested different configurations of the optical grid components to ensure their material compatibility and superior optical property, and developed detector calibration analysis programs in preparations of full detector calibration.
- I co-led the efforts of the optical grid fabrication, construction and QC/QA measurements.
- As a core member for the PROSPECT AD construction, I developed the procedures for the optical grade construction.
- During detector installation and commissioning, I participated the detector filling work, and was responsible for characterizing detector performance with

PROSPECT's initial wet commissioning and calibration data.

- I led the collaboration effort of detector energy scale calibration. This work involves equally significant effort of adjusting the PG4 simulation of detector response and reconstruction of calibration events with various interactions.
- I conducted studies of quantifying systematic uncertainties of the PROSPECT AD's energy response.
- I was also deeply involved in identifying the IBD event selection cuts.

## 10.2 Possible Improvement of This Work

The energy scale study for the PROSPECT spectrum measurement can be further improved by including the AmBe calibrations and BiPo energies into the data-MC comparison for parameter searching. This work requires better modeling of the AmBe calibration source and the beta energy from Bi in the PG4 simulation. The simulation of effective Cherenkov light can be adjusted with more realistic modeling of light transmission and indices of refraction. The density of  ${}^6\text{LiLS}$ , a key factor of particle stopping power, was simulated according to measurements with a prototype detector. A re-measurement of target density with realized PROSPECT detector is likely warranted.

Regarding to PROSPECT's reactor neutrino spectrum measurement, the AD has been collecting more reactor-on and -off data to further improve the precision of the spectrum measurement. Joint spectrum analysis between PROSPECT and other LEU experiments will be significantly helpful in searching for the isotopic contributions of the reactor neutrino spectrum shape discrepancy.

## BIBLIOGRAPHY

- [1] F. P. An *et al.*, “Improved Measurement of the Reactor Antineutrino Flux and Spectrum at Daya Bay,” *Chin. Phys.*, vol. C41, no. 1, p. 013002, 2017.
- [2] F. P. An *et al.*, “Evolution of the Reactor Antineutrino Flux and Spectrum at Daya Bay,” *Phys. Rev. Lett.*, vol. 118, p. 251801, Jun 2017.
- [3] M. G. Aartsen *et al.*, “Multimessenger observations of a flaring blazar coincident with high-energy neutrino IceCube-170922A,” *Science*, vol. 361, no. 6398, p. eaat1378, 2018.
- [4] J. Chadwick, “The intensity distribution in the magnetic spectrum of beta particles from radium (B + C),” *Verh. Phys. Gesell.*, vol. 16, pp. 383–391, 1914.
- [5] C. D. Ellis and W. A. Wooster, “The Average Energy of Disintegration of Radium E,” *Proceedings of the Royal Society of London Series A*, vol. 117, pp. 109–123, Dec. 1927.
- [6] E. Fermi, “Versuch einer theorie der  $\beta$ -strahlen. i,” *Zeitschrift für Physik*, vol. 88, pp. 161–177, Mar 1934.
- [7] C. Bemporad, G. Gratta, and P. Vogel, “Reactor-based neutrino oscillation experiments,” *Rev. Mod. Phys.*, vol. 74, pp. 297–328, Mar 2002.
- [8] C. L. Cowan, Jr., F. Reines, F. B. Harrison, H. W. Kruse, and A. D. McGuire, “Detection of the Free Neutrino: A Confirmation,” *Science*, vol. 124, pp. 103–104, July 1956.
- [9] B. Pontecorvo, “Electron and Muon Neutrinos,” *Sov. Phys. JETP*, vol. 10, pp. 1236–1240, 1960. [Zh. Eksp. Teor. Fiz.37,1751(1959)].
- [10] M. Schwartz, “Feasibility of using high-energy neutrinos to study the weak interactions,” *Phys. Rev. Lett.*, vol. 4, pp. 306–307, Mar 1960.
- [11] G. Danby, J.-M. Gaillard, K. Goulianos, L. M. Lederman, N. Mistry, M. Schwartz, and J. Steinberger, “Observation of high-energy neutrino reactions and the existence of two kinds of neutrinos,” *Phys. Rev. Lett.*, vol. 9, pp. 36–44, Jul 1962.
- [12] T. D. Lee and C. N. Yang, “Question of Parity Conservation in Weak Interactions,” *Phys. Rev.*, vol. 104, pp. 254–258, Oct 1956.
- [13] C. S. Wu, E. Ambler, R. W. Hayward, D. D. Hoppes, and R. P. Hudson, “Experimental test of parity conservation in beta decay,” *Phys. Rev.*, vol. 105, pp. 1413–1415, Feb 1957.
- [14] R. Davis, D. S. Harmer, and K. C. Hoffman, “Search for neutrinos from the sun,” *Phys. Rev. Lett.*, vol. 20, pp. 1205–1209, May 1968.
- [15] W. Hampel *et al.*, “Gallex solar neutrino observations: results for gallex iv,” *Physics Letters B*, vol. 447, no. 1, pp. 127 – 133, 1999.
- [16] M. Altmann *et al.*, “Complete results for five years of gno solar neutrino observations,” *Physics Letters B*, vol. 616, no. 3, pp. 174 – 190, 2005.

- [17] J. Abdurashitov *et al.*, “Results from sage (the russian-american gallium solar neutrino experiment),” *Physics Letters B*, vol. 328, no. 1, pp. 234 – 248, 1994.
- [18] Y. Fukuda *et al.*, “Solar Neutrino Data Covering Solar Cycle 22,” *Phys. Rev. Lett.*, vol. 77, pp. 1683–1686, Aug 1996.
- [19] D. Casper *et al.*, “Measurement of atmospheric neutrino composition with the IMB-3 detector,” *Phys. Rev. Lett.*, vol. 66, pp. 2561–2564, May 1991.
- [20] M. Nakahata *et al.*, “Atmospheric Neutrino Background and Pion Nuclear Effect for Kamioka Nucleon Decay Experiment,” *J. Phys. Soc. Jap.*, vol. 55, p. 3786, 1986.
- [21] Y. Fukuda *et al.*, “Evidence for Oscillation of Atmospheric Neutrinos,” *Phys. Rev. Lett.*, vol. 81, pp. 1562–1567, Aug 1998.
- [22] Q. R. Ahmad *et al.*, “Measurement of the Rate of  $\nu_e + d \rightarrow p + p + e^-$  Interactions Produced by  $^8B$  Solar Neutrinos at the Sudbury Neutrino Observatory,” *Phys. Rev. Lett.*, vol. 87, p. 071301, Jul 2001.
- [23] T. Yanagida, “Horizontal gauge symmetry and masses of neutrinos,” *Conf. Proc.*, vol. C7902131, pp. 95–99, 1979.
- [24] P. Ramond, M. Gell-Mann and R. Slansky, *Supergravity*. North-Holland, Amsterdam: D. Freedman and P. Van Nieuwenhuizen (eds.), 1979.
- [25] B. Pontecorvo, “Mesonium and anti-mesonium,” *Sov. Phys. JETP*, vol. 6, p. 429, 1957. [*Zh. Eksp. Teor. Fiz.*33,549(1957)].
- [26] B. Pontecorvo, “Inverse beta processes and nonconservation of lepton charge,” *Sov. Phys. JETP*, vol. 7, pp. 172–173, 1958. [*Zh. Eksp. Teor. Fiz.*34,247(1957)].
- [27] Z. Maki, M. Nakagawa, and S. Sakata, “Remarks on the unified model of elementary particles,” *Prog. Theor. Phys.*, vol. 28, pp. 870–880, 1962. [,34(1962)].
- [28] V. Gribov and B. Pontecorvo, “Neutrino astronomy and lepton charge,” *Physics Letters B*, vol. 28, no. 7, pp. 493 – 496, 1969.
- [29] B. Aharmim *et al.*, “Combined analysis of all three phases of solar neutrino data from the Sudbury Neutrino Observatory,” *Phys. Rev. C*, vol. 88, p. 025501, Aug 2013.
- [30] K. Eguchi *et al.*, “First Results from KamLAND: Evidence for Reactor Antineutrino Disappearance,” *Phys. Rev. Lett.*, vol. 90, p. 021802, Jan 2003.
- [31] M. Ambrosio *et al.*, “Atmospheric neutrino oscillations from upward throughgoing muon multiple scattering in MACRO,” *Physics Letters B*, vol. 566, no. 1, pp. 35 – 44, 2003.
- [32] W. W. M. Allison *et al.*, “Neutrino oscillation effects in Soudan 2 upward-stopping muons,” *Phys. Rev. D*, vol. 72, p. 052005, Sep 2005.
- [33] M. H. Ahn *et al.*, “Measurement of neutrino oscillation by the K2K experiment,” *Phys. Rev. D*, vol. 74, p. 072003, Oct 2006.
- [34] P. Adamson *et al.*, “Measurement of the neutrino mass splitting and flavor mixing by minos,” *Phys. Rev. Lett.*, vol. 106, p. 181801, May 2011.

- [35] K. Abe and othres, “Measurement of Neutrino Oscillation Parameters from Muon Neutrino Disappearance with an Off-Axis Beam,” *Phys. Rev. Lett.*, vol. 111, p. 211803, Nov 2013.
- [36] P. Adamson *et al.*, “First measurement of muon-neutrino disappearance in NOvA,” *Phys. Rev. D*, vol. 93, p. 051104, Mar 2016.
- [37] S. Adrian-Martinez *et al.*, “Measurement of Atmospheric Neutrino Oscillations with the ANTARES Neutrino Telescope,” *Phys. Lett.*, vol. B714, pp. 224–230, 2012.
- [38] M. G. Aartsen *et al.*, “Determining neutrino oscillation parameters from atmospheric muon neutrino disappearance with three years of IceCube DeepCore data,” *Phys. Rev. D*, vol. 91, p. 072004, Apr 2015.
- [39] F. P. An *et al.*, “Measurement of electron antineutrino oscillation based on 1230 days of operation of the Daya Bay experiment,” *Phys. Rev. D*, vol. 95, p. 072006, Apr 2017.
- [40] S.-B. Kim, “Measurement of neutrino mixing angle  $\Theta_{13}$  and mass difference  $\Delta m_{ee}^2$  from reactor antineutrino disappearance in the RENO experiment,” *Nucl. Phys.*, vol. B908, pp. 94–115, 2016.
- [41] Y. Abe *et al.*, “Improved measurements of the neutrino mixing angle  $\theta_{13}$  with the Double Chooz detector,” *JHEP*, vol. 10, p. 086, 2014. [Erratum: JHEP02,074(2015)].
- [42] M. Tanabashi *et al.*, “Review of Particle Physics,” *Phys. Rev. D*, vol. 98, p. 030001, Aug 2018.
- [43] X. Qian and J.-C. Peng, “Physics with reactor neutrinos,” *Reports on Progress in Physics*, vol. 82, p. 036201, feb 2019.
- [44] G. R. Jocher *et al.*, “Theoretical antineutrino detection, direction and ranging at long distances,” *Phys. Rept.*, vol. 527, pp. 131–204, 2013.
- [45] M. R. Bhat, “Evaluated Nuclear Structure Data File (ENSDF),” in *Nuclear Data for Science and Technology* (S. M. Qaim, ed.), (Berlin, Heidelberg), pp. 817–821, Springer Berlin Heidelberg, 1992.
- [46] D. Brown *et al.*, “ENDF/B-VIII.0: The 8th Major Release of the Nuclear Reaction Data Library with CIELO-project Cross Sections, New Standards and Thermal Scattering Data,” *Nuclear Data Sheets*, vol. 148, pp. 1 – 142, 2018. Special Issue on Nuclear Reaction Data.
- [47] K. SHIBATA *et al.*, “JENDL-4.0: A New Library for Nuclear Science and Engineering,” *Journal of Nuclear Science and Technology*, vol. 48, no. 1, pp. 1–30, 2011.
- [48] P. Vogel, G. K. Schenter, F. M. Mann, and R. E. Schenter, “Reactor Antineutrino Spectra and Their Application to Anti-neutrino Induced Reactions. 2.,” *Phys. Rev.*, vol. C24, pp. 1543–1553, 1981.
- [49] F. Von Feilitzsch, A. A. Hahn, and K. Schreckenbach, “Experimental Beta Spectra From Pu-239 And U-235 Thermal Neutron Fission Products And Their Correlated Anti-Neutrinos Spectra,” *Phys. Lett.*, vol. 118B, pp. 162–166, 1982.

- [50] K. Schreckenbach, G. Colvin, W. Gelletly, and F. Von Feilitzsch, “Experimental Beta Spectra From Pu-239 And U-235 Thermal Neutron Fission Products And Their Correlated Anti-Neutrinos Spectra,” *Phys. Lett.*, vol. 160B, pp. 325–330, 1985.
- [51] A. A. Hahn, K. Schreckenbach, G. Colvin, B. Krusche, W. Gelletly, and F. Von Feilitzsch, “Anti-neutrino Spectra From  $^{241}\text{Pu}$  and  $^{239}\text{Pu}$  Thermal Neutron Fission Products,” *Phys. Lett.*, vol. B218, pp. 365–368, 1989.
- [52] F. Reines, H. W. Sobel, and E. Pasierb, “Evidence for Neutrino Instability,” *Phys. Rev. Lett.*, vol. 45, p. 1307, 1980.
- [53] H. Kwon *et al.*, “Search for Neutrino Oscillations at a Fission Reactor,” *Phys. Rev.*, vol. D24, pp. 1097–1111, 1981.
- [54] G. Zacek *et al.*, “Neutrino-oscillation experiments at the gösigen nuclear power reactor,” *Phys. Rev. D*, vol. 34, pp. 2621–2636, Nov 1986.
- [55] A. I. Afonin *et al.*, “ $\bar{\nu}_e$  Spectra at Two Distances From the Reactor of the Rovno Nuclear Power Plant: Search for Oscillations,” *JETP Lett.*, vol. 45, pp. 247–251, 1987. [Pisma Zh. Eksp. Teor. Fiz.45,201(1987)].
- [56] G. S. Vidyakin *et al.*, “Limitations on the characteristics of neutrino oscillations,” *JETP Lett.*, vol. 59, pp. 390–393, 1994. [Pisma Zh. Eksp. Teor. Fiz.59,364(1994)].
- [57] Y. Declais *et al.*, “Search for neutrino oscillations at 15-meters, 40-meters, and 95-meters from a nuclear power reactor at Bugey,” *Nucl. Phys.*, vol. B434, pp. 503–534, 1995.
- [58] Z. D. Greenwood *et al.*, “Results of a two position reactor neutrino oscillation experiment,” *Phys. Rev.*, vol. D53, pp. 6054–6064, 1996.
- [59] M. Apollonio *et al.*, “Initial results from the CHOOZ long baseline reactor neutrino oscillation experiment,” *Phys. Lett.*, vol. B420, pp. 397–404, 1998.
- [60] M. Apollonio *et al.*, “Limits on neutrino oscillations from the CHOOZ experiment,” *Phys. Lett.*, vol. B466, pp. 415–430, 1999.
- [61] M. Apollonio *et al.*, “Search for neutrino oscillations on a long baseline at the CHOOZ nuclear power station,” *Eur. Phys. J.*, vol. C27, pp. 331–374, 2003.
- [62] F. Boehm *et al.*, “Final results from the Palo Verde neutrino oscillation experiment,” *Phys. Rev.*, vol. D64, p. 112001, 2001.
- [63] F. Boehm *et al.*, “Search for neutrino oscillations at the Palo Verde nuclear reactors,” *Phys. Rev. Lett.*, vol. 84, pp. 3764–3767, 2000.
- [64] F. Boehm *et al.*, “Results from the Palo Verde neutrino oscillation experiment,” *Phys. Rev.*, vol. D62, p. 072002, 2000.
- [65] T. Araki *et al.*, “Measurement of neutrino oscillation with KamLAND: Evidence of spectral distortion,” *Phys. Rev. Lett.*, vol. 94, p. 081801, 2005.
- [66] T. A. Mueller *et al.*, “Improved Predictions of Reactor Antineutrino Spectra,” *Phys. Rev.*, vol. C83, p. 054615, 2011.

- [67] P. Huber, “On the determination of anti-neutrino spectra from nuclear reactors,” *Phys. Rev.*, vol. C84, p. 024617, 2011. [Erratum: *Phys. Rev.*C85,029901(2012)].
- [68] F. P. An *et al.*, “Measurement of the Reactor Antineutrino Flux and Spectrum at Daya Bay,” *Phys. Rev. Lett.*, vol. 116, no. 6, p. 061801, 2016. [Erratum: *Phys. Rev. Lett.*118,no.9,099902(2017)].
- [69] G. Mention, M. Fechner, T. Lasserre, T. A. Mueller, D. Lhuillier, M. Cribier, and A. Letourneau, “The Reactor Antineutrino Anomaly,” *Phys. Rev.*, vol. D83, p. 073006, 2011.
- [70] K. N. Abazajian *et al.*, “Light Sterile Neutrinos: A White Paper,” 2012.
- [71] A. C. Hayes, J. L. Friar, G. T. Garvey, G. Jungman, and G. Jonkmans, “Systematic Uncertainties in the Analysis of the Reactor Neutrino Anomaly,” *Phys. Rev. Lett.*, vol. 112, p. 202501, 2014.
- [72] D. A. Dwyer and T. J. Langford, “Spectral Structure of Electron Antineutrinos from Nuclear Reactors,” *Phys. Rev. Lett.*, vol. 114, no. 1, p. 012502, 2015.
- [73] C. Giunti, Y. F. Li, B. R. Littlejohn, and P. T. Surukuchi, “Diagnosing the Reactor Antineutrino Anomaly with Global Antineutrino Flux Data,” *Phys. Rev.*, vol. D99, no. 7, p. 073005, 2019.
- [74] G. Bak *et al.*, “Fuel-composition dependent reactor antineutrino yield at RENO,” *Phys. Rev. Lett.*, vol. 122, p. 232501, 2019.
- [75] J. Ashenfelter *et al.*, “PROSPECT Physics Program,” *J. Phys. G*, vol. 43, p. 113001, 2016.
- [76] J. Ashenfelter *et al.*, “The PROSPECT Reactor Antineutrino Experiment,” *Nuclear Instruments and Methods in Physics Research Section A: Accelerators, Spectrometers, Detectors and Associated Equipment*, vol. 922, pp. 287 – 309, 2019.
- [77] J. Swartout, A. Boch, T. Cole, R. Cheverton, G. Adamson, and C. Winters, “The Oak Ridge High Flux Isotope Reactor.,” Tech. Rep. 4042265, Oak Ridge National Laboratory, 10 1964.
- [78] J. Ashenfelter *et al.*, “Background Radiation Measurements at High Power Research Reactors,” *Nucl. Instrum. Meth.*, vol. A806, pp. 401–419, 2016.
- [79] J. Ashenfelter *et al.*, “Lithium-loaded Liquid Scintillator Production for the PROSPECT experiment,” *JINST*, vol. 14, no. 03, p. P03026, 2019.
- [80] J. Ashenfelter *et al.*, “A Low Mass Optical Grid for the PROSPECT Reactor Antineutrino Detector,” *JINST*, vol. 14, no. 04, p. P04014, 2019.
- [81] J. Ashenfelter *et al.*, “Performance of a segmented 6 Li-loaded liquid scintillator detector for the PROSPECT experiment,” *Journal of Instrumentation*, vol. 13, no. 06, p. P06023, 2018.
- [82] J. Ashenfelter *et al.*, “Light Collection and Pulse-Shape Discrimination in Elongated Scintillator Cells for the PROSPECT Reactor Antineutrino Experiment,” *JINST*, vol. 10, no. 11, p. P11004, 2015.

- [83] M. F. Weber, C. A. Stover, L. R. Gilbert, T. J. Nevitt, and A. J. Ouder Kirk, “Giant Birefringent Optics in Multilayer Polymer Mirrors,” *Science*, vol. 287, no. 5462, pp. 2451–2456, 2000.
- [84] J. Ashenfelter *et al.*, “The Radioactive Source Calibration System of the PROSPECT Reactor Antineutrino Detector,” 2019.
- [85] N. I. of Standard and Technology, “E-star.”
- [86] J. B. Birks, “Scintillations from Organic Crystals: Specific Fluorescence and Relative Response to Different Radiations,” *Proceedings of the Physical Society A*, vol. 64, pp. 874–877, Oct. 1951.
- [87] J. BIRKS in *The Theory and Practice of Scintillation Counting* (J. BIRKS, ed.), International Series of Monographs in Electronics and Instrumentation, pp. 1 – 14, Pergamon, 1964.
- [88] P. A. Cherenkov, “Visible luminescence of pure liquids under the influence of  $\gamma$ -radiation,” *Dokl. Akad. Nauk SSSR*, vol. 2, no. 8, pp. 451–454, 1934. [Usp. Fiz. Nauk93,no.2,385(1967)].
- [89] S. Agostinelli *et al.*, “GEANT4: A Simulation toolkit,” *Nucl. Instrum. Meth.*, vol. A506, pp. 250–303, 2003.
- [90] C. Hagmann, D. Lange, and D. Wright, “Cosmic-ray shower generator (CRY) for Monte Carlo transport codes,” in *2007 IEEE Nuclear Science Symposium Conference Record*, vol. 2, pp. 1143–1146, Oct 2007.
- [91] F. James, “MINUIT Function Minimization and Error Analysis: Reference Manual Version 94.1,” 1994.
- [92] “B12 beta decay evaluated data.” <http://www.tunl.duke.edu/nuclldata/GroundStatedecays/12B.shtml>.
- [93] J. Ashenfelter *et al.*, “First search for short-baseline neutrino oscillations at HFIR with PROSPECT,” *Phys. Rev. Lett.*, vol. 121, no. 25, p. 251802, 2018.
- [94] J. Ashenfelter *et al.*, “Measurement of the Antineutrino Spectrum from  $^{235}\text{U}$  Fission at HFIR with PROSPECT,” *Phys. Rev. Lett.*, vol. 122, no. 25, p. 251801, 2019.
- [95] “Oak Ridge Reservation Meteorology.” <https://metweb.ornl.gov>. Accessed: 2018-11-02.